Polymer/Fullerene Photovoltaic Devices - Nanoscale Control of the Interface by Thermally-controlled Interdiffusion

Martin Drees

Dissertation submitted to the Faculty of the Virginia Polytechnic Institute and State University in partial fulfillment of the requirements for the degree of

Doctor of Philosophy
in
Physics

James R. Heflin, Chair
Richey M. Davis
Guy J. Indebetouw
Massimiliano Di Ventra
Richard H. Zallen

May 12, 2003
Blacksburg, Virginia

Keywords : Organic Photovoltaics, Conjugated Polymers, Interdiffusion, Gradient Bulk-heterojunction

Virginia Polytechnic Institute and State University

Polymer/Fullerene Photovoltaic Devices - Nanoscale Control of the Interface by Thermally-controlled Interdiffusion

by Martin Drees

Abstract

In this thesis, the interface between the electron donor polymer and the electron acceptor fullerene in organic photovoltaic devices is studied. Starting from a bilayer system of donor and acceptor materials, the proximity of polymer and fullerene throughout the bulk of the devices is improved by inducing an interdiffusion of the two materials by heating the devices in the vicinity of the glass transition temperature of the polymer. In this manner, a concentration gradient of polymer and fullerene throughout the bulk is created. The proximity of a fullerene within 10 nm of any photoexcitation in the polymer ensures that the efficient charge separation occurs. Measurements of the absorption, photoluminescence, and photocurrent spectra as well as I-V characteristics are used to study the interdiffusion and its influence on the efficiency of the photovoltaic devices. In addition, the film morphology is studied on a microscopic level with transmission electron microscopy and with Auger spectroscopy combined with ion beam milling to create a depth profile of the polymer concentration in the film.

Initial studies to induce an interdiffusion were done on poly(2-methoxy-5-(2'-ethylhexyloxy)-1,4-phenylenevinylene) (MEH-PPV) as the electron donor polymer and the buckminsterfullerene C_{60} as the electron acceptor. Interdiffused devices show an order of magnitude photoluminescence quenching with concomitant increase in the photocurrents by an order of magnitude. Variation of the polymer layer thickness shows that the photocurrents increase with decreasing thickness down to 70 nm due to charge transport limitation. The choice of layer thickness in organic photovoltaic devices is

critical for optimization of the efficiency. The interdiffusion process is also monitored *in situ* and a permanent increase in photocurrents is observed during the heat treatment. Transmission electron microscopy (TEM) studies on cross sections of the film reveal that C_{60} interdiffuses into the MEH-PPV bulk in the form of >10 nm clusters. This clustering of C_{60} is a result of its tendency to crystallize and the low miscibility of C_{60} in MEH-PPV, leading to strong phase separation.

To improve the interdiffusion process, the donor polymer is replaced by poly(3-octylthiophene-2,5-diyl) (P3OT), which has a better miscibility with C_{60}. Again, the photocurrents of the interdiffused devices are improved significantly. A monochromatic power conversion efficiency of 1.5 % is obtained for illumination of 3.8 mW/cm^2 at 470 nm. The polymer concentration in unheated and interdiffused films is studied with Auger spectroscopy in combination with ion beam milling. The concentration profile shows a distinct interface between P3OT and C_{60} in unheated films and a slow rise of the P3OT concentration throughout a large cross-section of the interdiffused film. TEM studies on P3OT/C_{60} films show that C_{60} still has some tendency to form clusters.

The results of this thesis demonstrate that thermally-controlled interdiffusion is a viable approach for fabrication of efficient photovoltaic devices through nanoscale control of composition and morphology. These results are also used to draw conclusions about the influence of film morphology on the photovoltaic device efficiency and to identify important issues related to materials choice for the interdiffusion process. Prospective variations in materials choice are suggested to achieve better film morphologies.

To my dear wife

Her love and support is my inspiration

Acknowledgements

I would like to thank my advisor, Dr. Randy Heflin, for his help and advice during the last three years. His generous support allowed me to spend most of my time on research and also to travel to interesting conferences. His advice was most valuable to understand the obtained results and to determine the next steps for the research presented in this thesis.

I am indebted to Dr. Rick Davis who took quite some time to help me understand more about polymers and molecular interdiffusion. The discussions with him always brought up interesting ideas for new studies and possible interpretations of the observed data.

A special thank you goes to Dr. Wilhelm "Willi" Graupner, who was the first person to introduce me to the field of organic optoelectronics. His enthusiasm motivated me to learn more about this interesting class of materials and to actually do my Ph.D. research in this field.

I would like to thank Daniela Marciu Topasna and Nicole Short from Luna Innovations for all their help and support. It was a great experience to be able to work in close collaboration with an industrial partner on this project.

Steve McCartney has to be mentioned here. He always managed to clear up some time in his busy schedule to do TEM studies on my samples. Also thank you to Frank Cromer for the help with the Auger spectroscopy studies, to Dr. Herve Marand for DSC studies and to Dr. Guy Indebetouw for letting me use his laser facilities for the PL studies.

Joe Santoro and Henning Back are great friends who suffered long days and nights with me to get through the homework and exams during the first years. Thank you to Pat Neyman for some interesting discussions and for setting up the wet lab in room 6. Also Raoul Schröder, Artur Erlacher, Thomas Piok and Charles Brands have helped me gain valuable insight about organic optoelectronics.

The staff in the Physics Department at VT has been the backbone of my research - especially Melvin Shaver, John Miller , and Scott Allen from the machine shop, Fred Mahone from the electronics shop, Roger Link, Travis Heath, Judy Faw, and Janet Sanders. Chris Thomas has watched over me (as she does for all graduate students) to make sure that all administrative paper work is always up to date and to make all of us feel welcome and at home in Blacksburg.

I would like to thank my parents for their help throughout my life, especially the generous financial support that allowed me to study abroad at VT.

Of course, I would like to thank my loving wife Sarah. Her love and support helped me tremendously. I could always count on her cheering me up during the frustrating times that are inevitable during the long process of getting your Ph.D.

Table of Contents

List of Figures

List of Tables

Chapter 1

Motivation and Outline

The worldwide demand for energy has grown dramatically over the last century with an increase in the industrialization of the world. The need for energy is likely to grow even more in the 21st century with the improvements in living standards across the planet. This high demand of energy brings into question the energy sources currently used and the depletion of natural resources.

1.1 Fossil Fuels

Oil, coal, and natural gas are usually referred to as fossil fuels. The percentage of energy production that is from fossil fuels was more than 70 % in the US in 2000 (see Figure 1). The combustion of fossil fuels is used to produce electric power and heat. The

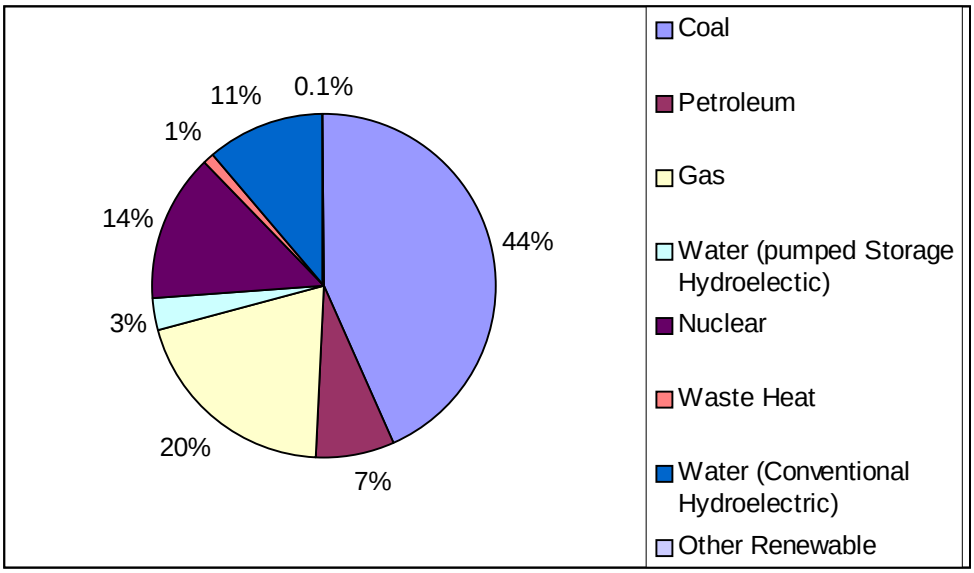

Figure 1 Existing capacity at U.S. electric utilities by energy source (2000). The chart shows the percentage of each energy source in the total capacity. The other renewable sources summarize geothermal, nonwood waste, solar, wind, wood and woodwaste. The percent missing to add up to 100 % is due to rounding (source: http://www.eia.doe.gov).

byproducts of this combustion process are carbon dioxide (CO_2) and sulfur compounds like SO_2. While the former is related to the greenhouse effect [1] leading to global warming and the rise in sea level, the latter is a cause of acid rain harming the environment.

In addition to the catastrophic environmental consequences of using fossil fuels, the earth's resources of oil, coal, and natural gas are limited and will deplete sooner or later. Estimates suggest that within 20 years oil and natural gas production rates will start to decrease [2,3]. With these prospects, new sources of energy must be implemented that do not rely on depleting resources.

1.2 Renewable Energy

Renewable energy sources use natural resources without depleting them and with no harmful side effects for the environment. Examples include power plants that use wind energy; energy from water due to waves, tidal motion or potential energy (rivers); and

solar energy. The energy provided by the sun can be used in solar collector systems to heat water or by direct conversion into electric energy in photovoltaic devices.

Current renewable energy systems cannot produce energy at the low cost that conventional fossil fuel power plants can. For large-scale implementation of renewable energy power plants, it is therefore necessary to develop systems that can compete on an economic level with fossil fuel facilities, either by decreasing cost, increasing efficiency, or a combination of both.

1.3 Plastic Solar Cells

Photovoltaics are attractive renewable energy power sources. The sun supplies a peak intensity of about 1 kW/m^2 on the surface of the earth. Of course, this intensity is reduced when the sun is not at zenith due to location or time of day. The optical energy supplied by the sun can be converted into electric energy in a solar cell. Due to the rather high cost of Si solar cell systems today, they are mainly used in remote locations where there is no power line from a conventional power plant available. To make solar cell systems more competitive with fossil fuel power plants, a significant reduction in cost must be achieved.

A promising approach towards low cost photovoltaic devices is fabrication of solar cells based on organic materials [4,5,6,7,8,9]. In one class of these devices, Si or GaAs are replaced by semiconducting polymer materials in combination with fullerene materials as the active layer. These materials are usually soluble in common organic solvents. This solubility makes device production relatively easy. Thin films can be spin cast [10] or doctor bladed [11] from solution. Even screen printing and ink jet printing have been demonstrated [12]. Since thin organic films are flexible, they can also be applied to flexible plastic substrates making the whole device flexible and allowing for cheap roll-to-roll production methods.

Another unique characteristic of polymeric materials is that the optical and electrical properties can be changed by altering the molecular structure of the monomers.

It is therefore possible to tune the optical and electrical properties of the polymer in order to optimize device performance.

A challenge in organic photovoltaic devices is to achieve efficient charge separation of electrons and holes created by the absorption of photons. Charge separation in polymer/fullerene systems is achieved by ultrafast transfer of photoexcited electrons from the polymer to the fullerene. This ultrafast charge transfer from a conducting polymer onto buckminsterfullerene C_{60} was first reported by Sariciftci *et al.* on a blend of poly(2-methoxy-5-(2'-ethylhexyloxy)-1,4-phenylenevinylene), hereafter referred to as MEH-PPV, and C_{60} [13]. Charge transfer from the polymer to the fullerene leads to a spatial separation of electrons and holes that is needed for efficient photovoltaic devices. An upper limit for the electron transfer time was found to be 300 fs in this system [14] versus a photoluminescence lifetime of 550 ps in the pristine polymer. Several studies determined the charge transfer range to be within 5 to 10 nm [15,16,17]. Therefore the C_{60} molecule has to be within ~10 nm of the location of the photoexcitation for the charge transfer to occur. The actual mechanism that leads to charge transfer from polymer to fullerene is an issue that is still debated and will be discussed in more detail in Section 2.1.2. Since the electron transfer time is 3 orders of magnitude faster than the competing process of photoluminescence, the probability of charge transfer is close to unity if the C_{60} is within transfer range.

Early studies showed the importance of close proximity of polymer and fullerene for the efficiency of photovoltaic devices. Devices produced in a bilayer structure with a single interface between electron donor and electron acceptor [18] had low efficiencies because the volume of the active layer, where efficient charge separation occurred, was limited to a small fraction at the interface.

To overcome this problem, Yu *et al.* prepared devices from a solution containing a blend of MEH-PPV and the methanofullerene (phenyl-[6,6]-C_{61})-butyric acid methyl ester (PCBM) [6]. The derivatization of C_{60} leads to better solubility of the fullerene in organic solvents and to better miscibility of polymer and fullerene. With this device structure, the efficiency was improved by nearly two orders of magnitude. In a similar approach with the active layer cast from a blend solution of polymer and fullerene, the total power conversion efficiency under simulated sunlight conditions was improved to

2.5 % [4]. This is to be compared to 10-15 % power conversion efficiencies in commercial silicon solar cells.

To further enhance the efficiency of devices, a slightly more complicated structure is suggested where the interface between electron donor and acceptor is diffuse, but at the electrodes only the donor material has contact to the anode and only the acceptor material has contact to the cathode. This structure should enhance the transport of electrons and holes through the acceptor and donor material respectively in a preferred direction to the extracting electrodes. In addition, this structure is believed to enhance rectification of the photovoltaic devices by preventing direct pathways for the charge carriers from the cathode to the anode through either of the materials. Better rectification will improve the fill factor (for an explanation of fill factor please refer to Chapter 2) and with that the efficiency of the solar cells.

Several different approaches have been implemented to achieve this kind of structure in the active layer. In one, the temperature dependence of the solubility of the conducting polymer was used [10,19]. Poly[2-methoxy-5-(3',7'-dimethyloctyloxy)-1,4-phenylenevinylene], MDMO-PPV, exhibits good solubility in xylenes at 90 ^{o}C but is only slighlty soluble at room temperature. Using this, the devices were fabricated by spin casting MDMO-PPV from a hot solution and afterwards spin casting PCBM as the fullerene acceptor from a room temperature xylene solution. Spin casting of the PCBM layer led to a partial dissolution of the MDMO-PPV layer, allowing the PCBM to diffuse in the polymer bulk. Devices produced with this method exhibited full quenching of the photoluminescence, which shows that PCBM diffused into the polymer bulk. In addition, the power conversion efficiency improved by a factor 4-5 compared to homogeneous blends of the same materials (0.5 % power conversion efficiency under 780 W/m^2 simulated solar spectrum).

A completely different approach was based on a lamination technique [5]. Here, both electron donor and acceptor materials were polymeric. They were spin cast onto different substrates containing the anode and cathode and then laminated under vacuum at elevated temperatures (200^{o}C). The lamination at high temperatures led to an intermixture of the two polymers, creating a diffuse interface but still having only one polymer in contact with either electrode. Devices produced in this fashion exhibited high

external quantum efficiencies (up to 28 % at peak) that were larger than devices produced from a blend of the two polymers.

Another approach is the so-called “bulk diffusion bilayer” [11]. Here, a layer of MDMO-PPV was doctor bladed onto the substrate first and then a second layer of PCBM was doctor bladed from a solution with the same solvent. During the application of the PCBM layer, the polymer swelled or even partially dissolved and allowed the PCBM to diffuse into the polymer bulk. In devices produced in this way, the phase separation of donor and acceptor material was reduced. The reduction in phase separation also reduced the number of pinholes in the film, which led to fewer shorts in the devices. Solar cells manufactured with the bulk diffusion layer had at least comparable efficiencies to devices produced from a blend solution of MDMO-PPV and PCBM.

In this work, a new approach to achieve this close proximity of polymer and fullerene components in a gradient structure is introduced [20,21,22]. Devices are first fabricated in a bilayer structure and then interdiffusion of the fullerene into the polymer bulk is induced by heating the device at temperatures in the vicinity of the glass transition temperature of the polymer. This way, the morphology of the active layer exhibits good proximity of polymer and fullerene throughout the bulk with a concentration gradient of the two components from one electrode to the other. Since electrons and holes are transported separately in the fullerene and polymer phase, respectively, the concentration gradient of the materials should support the charge transport of either charge in the preferred direction. The approach does not require both components to be soluble. However, as shown in this thesis, the miscibility of the two materials is critical. Devices with external quantum efficiencies of up to 28 % and monochromatic power conversion efficiencies of up to 1.5 % were fabricated. These conversion efficiencies are lower than the best reported (~10 %), but in those studies different polymer and fullerene materials were used. Therefore with a different choice of materials the interdiffusion approach has a great potential for further improvements.

1.4 Outline

Chapter 2 gives an introduction to excitation processes and charge carriers in polymer and fullerene materials. This knowledge is essential to understand the charge creation and separation processes that occur in organic photovoltaic devices. Afterwards, a basic description of photovoltaic devices and their characteristics is given. Finally, a few considerations concerning heat and mass transfer related to the interdiffuion heating are discussed.

In Chapter 3, the experimental setups and methods are described. In addition, some information about the polymer and fullerene materials in the active layer is given as well as information about the electrode materials of the devices.

Some preliminary studies related to the heating process are presented in Chapter 4. Here, the photoluminescence behavior of a pristine polymer layer was studied during the heating process.

In Chapters 5 and 6, the main work of this research is described. Two different polymers were used to study the interdiffusion of polymer and fullerene layers starting from a bilayer of the two materials. The photoluminescence and the photocurrents as well as the current-voltage characteristics of photovoltaic cells were investigated. In Chapter 5, the polymer and fullerene exhibited low miscibility. Nonetheless, the photoluminescence was quenched by an order of magnitude after interdiffusion heating. The photocurrents showed concomitant increase by an order of magnitude. This demonstrates that the proximity of polymer donor and fullerene acceptor was improved throughout the bulk of the active layer. Variation of the polymer layer thickness showed that the device efficiency increased with decreasing polymer layer thickness within the thickness range tested due to limitations in the charge transport. In addition, the interdiffusion process was monitored *in situ* by observing improved photocurrents during and after the heat-treatment. Morphology studies with transmission electron microscopy on cross-sections of the film revealed that C_{60} forms >10 nm clusters that diffuse into the polymer bulk. These large C_{60} clusters put a constraint on the interdiffusion and therefore limit the possible improvements in device efficiency.

To improve miscibility of polymer and C_{60}, a different polymer was used in Chapter 6. The polymer used was microscrystalline, thus exhibiting both a glass transition temperature and a melting temperature. Photoluminescence quenching of 2 orders of magnitude showed that the better miscibility led to diffusion of small quantities of C_{60} into the polymer bulk even in the unheated bilayer devices. Upon heat-treatment, the photocurrents improved by an order of magnitude independent of whether the interdiffusion heating was done below or above the melting temperature. The I-V characteristics showed improved open circuit voltage and fill factor. Larger improvements were achieved for heating below the melting temperature. The morphology of films was analyzed with Auger spectroscopy in combination with ion beam milling. This technique measures the polymer concentration in the surface layer and, in combination with the milling, a depth profile of the film is acquired. While the unheated bilayer films had a distinct interface between polymer and fullerene, the interdiffused films (below melting temperature) had a concentration gradient of the polymer content throughout most of the film's cross-section. Heating above the melting temperature led to a blend of polymer and C_{60} without a concentration gradient, which shows that in this case the resulting film morphology was interdiffused beyond the intended concentration gradient structure. In addition, transmission electron microscopy showed that C_{60} again forms some clusters that move into the film

Chapter 7 gives the conclusions drawn from this work. Also, future projects are suggested using the thermally-controlled interdiffusion process introduced in this thesis.

Chapter 2

Background on Polymer Photovoltaics

Polymers were originally studied primarily because of their attractive mechanical and structural properties and easy processability. The discovery of conducting polymers in the mid 1970's has led to intense research of a whole new class of materials, showing that the electrical properties of polymers can range from insulating to semiconducting to conducting (conductivity >100,000 S/cm has been shown [23]). These new semiconducting and conducting materials combine the electrical and optical properties of inorganic semiconductors with the mechanical flexibility of polymers. While the electrical and optical properties can be quite similar to inorganics, the charge carriers and charge transport mechanisms in semiconducting polymers are essentially different from their inorganic counterparts.

In this chapter, the charge carriers and excitation processes that are important for understanding organic photovoltaic devices are described. A much broader introduction

to the field of organic electronic materials can be found, for example, in references 24 or 25. After that, an introduction to photovoltaic devices is given. Here, the aim is to give the reader a basic understanding of the most important characteristics of solar cells with a focus on organic devices. At the end, a few topics related to the heat-induced interdiffusion process used in this thesis are introduced.

2.1 Charge Transport in Organic Materials

Semiconducting polymers can usually be described as quasi-one-dimensional semiconductors. Semiconducting and conducting polymers are conjugated polymers, which refers to the alternating single and double bonds between the carbon atoms on the polymer backbone. The double bonds result from the fact that, while carbon has four valence electrons, the carbon atoms in conjugated molecules bind to only three (or sometimes two) other atoms. The remaining electrons form π-electron bonds that are delocalized over the entire molecule. While the polymer chains can be very long (microns), the conjugation length along the chain can be interrupted (e.g. by foreign atoms, bending of the polymer chain, or crosslinks) and is typically less than 100 nm. The molecular levels are grouped in bands, and in the limit of very long conjugation length, the band structure picture associated with inorganic semiconductors can be applied to organic semiconductors. The band edge of the valence band is referred to as the "Highest Occupied Molecular Orbital" (HOMO) and the edge of the conduction band is called the "Lowest Unoccupied Molecular Orbital" (LUMO).

2.1.1 Photoexcitation in Polymers

The energy gap between the HOMO and LUMO level in conjugated polymers is typically within the range of visible photons. Upon absorption of an incoming photon, an electron is promoted into the LUMO level, leaving behind a hole in the HOMO level.

The two main excited species resulting out of this photon absorption will be described in the following.

Singlet Excitons

After photon absorption, it is likely that the created electron hole pair forms a singlet exciton. This means that the electron and hole remain on the same polymer chain and are bound to each other by their electrostatic attraction. The energy levels of the singlet exciton are located within the HOMO-LUMO gap. The excitons can migrate within the film to lower energy sites [26]. This process is referred to as exciton energy migration. The typical lifetime of singlet excitons is in the hundreds of picoseconds [27,28] after which they can recombine radiatively or nonradiatively. The diffusion length is typically of the order of 10 nm [16,17].

The binding energy E_b of singlet excitons has been a subject of great debate over the last decade. Values for E_b ranging from $E_b < k_bT = 25\ meV$ [29,30], which means that at room temperature the electron and hole are not bound, all the way to $E_b \sim 1\ eV$ [31]. Evidence seems to indicate that a third school, namely $E_b \sim 0.3 - 0.4\ eV$ [32,33] gives a correct picture of most conjugated polymers, including the ones used in this thesis. In band energy diagrams in this thesis, the slightly lower energy levels of the excitons will be neglected and instead the HOMO-LUMO gap will be presented.

Polarons

Upon adding a charge to a polymer chain, the chain will deform to lower the energy of the carrier. This charge and deformation together constitute a polaron, hereafter denoted as P^+ or P^- depending on the sign of the charge. The energy levels of a polaron are within the HOMO-LUMO gap. Polarons can drift along the conjugated chain. Once

they reach the end of a conjugated segment, a hopping process to another conjugated chain can occur. Thus, in an applied electric field, a combination of drifting and hopping of polarons leads to charge transport through the film.

It should be noted here that for creation of a P^+/P^- polaron pair upon photon absorption, the electron and hole must be separated sufficiently in space, so that there is no Coulomb attraction binding them together. This can be achieved by removing the electron or hole within femtoseconds after photon absorption from the chain or by trapping one of the charges at an impurity or defect. The former will be discussed in more detail in Section 2.1.2.

2.1.2 Donor-Acceptor Interface

In most conjugated polymers, the predominant excited species is the singlet exciton. As was discussed in Section 2.1.1, at room temperature the electron and hole are bound to each other and there are no free charge carriers. An essential process for polymeric solar cells after photoexcitation is charge separation. Since the electron and hole are bound together, a mechanism must be found to efficiently separate electron and hole and to prevent recombination of the two. A possibility to achieve this charge separation is by introducing an electron acceptor that dissociates the exciton by transferring the electron from the polymer (therefore being the electron donor) to the electron acceptor material. As a result, the polymer is left with a P^+ polaron that can drift through the film to the anode while the electron is in the acceptor material and can be transported to the cathode. The main condition for the exciton dissociation to occur is that the electron affinity of the acceptor is larger than the ionization potential of the donor.

A well-known acceptor material is the buckminsterfullerene C_{60}. Since the discovery of ultrafast charge transfer from conjugated polymers to C_{60} [13], its properties as an electron acceptor have been subject to intense research. The charge transfer typically occurs within the femtosecond time regime. An upper time limit was found to be 300 fs [14] which is three orders of magnitude faster than any electron-hole

recombination process within the polymer. As already mentioned in Chapter 1, the charge transfer range is about 5-10 nm, which makes close proximity of C_{60} to the photoexcitation on the polymer essential. While the charge transfer range is similar in different models, the mechanism leading to the electron transfer from the polymer to the fullerene is a subject of controversy. Halls *et al.* suggest that the singlet excitons diffuse from the location of photoexcitation to the polymer-fullerene interface and are dissociated at the interface [16]. They studied the photovoltaic response in heterojunction devices prepared from poly(phenylenevinylene) (PPV) and C_{60}. In addition to experiments, they modeled the photocurrent spectra under the assumption that all absorbed photons create singlet excitons and all singlet excitons within the diffusion range of the interface are dissociated and contribute to the photocurrent. From the quantitative agreement of the modeled current spectra and the experimental spectra they deduce a diffusion range of 6-8 nm and conclude that the agreement is strong evidence for the diffusion model. This diffusion model is disputed by Vacar *et al.* [15]. From transient photoinduced absorption experiments on MEH-PPV/C_{60} bilayer films, they found that the ultrafast charge transfer occurs on a picosecond time scale. Using this time scale and a diffusion range of ~10 nm, the necessary diffusion constants and mobilities in the polymer would have to be much higher (at least 2 orders of magnitude) than they are known to be. Instead, they suggest that the wave functions of the primary excitations on the polymer must be spatially extended over ~10 nm to explain the rapid charge transfer. Further analysis of their data leads to a charge transfer range of approximately 8 nm in the MEH-PPV/C_{60} system.

Even though the actual mechanism of charge transfer is unresolved, the charge transfer range is determined to be the same in both models. Since the transfer mechanism is not essential for this work, no further effort was made to resolve this issue. Instead, the transfer range, which is of great importance for this work, was assumed to be that found in both models. Therefore, if the C_{60} is within ~10 nm of the photoexcitation, the probability for charge transfer is close to unity because it is 3 orders of magnitude faster than competing recombination processes. Back-transfer of the electron onto the polymer does not occur, which makes the charge separated state metastable.

There are two general ways to create a donor-acceptor interface in organic devices. One is to bring two films in contact at the surface, which creates a heterojunction. In this case, only a fraction of the bulk of the materials (within ~10 nm of the interface) builds a donor-acceptor interface. The other is to blend the two materials to form one mixed layer. In this case, the whole bulk of the device has a donor-acceptor interface. These devices are called bulk-heterojunction devices. There are various methods to create a bulk-heterojunction including blending of the materials in a solution from which the film is cast, interdiffusion of the two materials into each other, or coevaporation of both materials.

2.1.3 Exciton Dissociation at Oxygen Traps

Another possibility for a singlet exciton to dissociate is at an oxygen trap in the polymer chain. These traps can be introduced when the polymer is exposed simultaneously to oxygen and light, a process called photo-oxidation. In PPV, the oxygen reacts with a vinylene group forming a carbonyl group. This carbonyl group has a strong electron affinity which makes it favorable for the electron of an exciton to transfer onto the carbonyl group thereby dissociating the exciton [34,35]. The hole is now free to move along the polymer as a free charge carrier while the electron is trapped at the site of the carbonyl group.

This charge separation process is similar to the dissociation of an exciton at a donor-acceptor interface. The main difference is that the electron remains on the polymer chain at the location of the trap. While the hole can be transported to the collecting anode, the electron is not free to move and will eventually recombine with a hole in the valence band of the polymer. Thus, photo-oxidation can be interpreted as p-doping the polymer by increasing the number of free holes and enhancing the photoconductivity.

In general, photo-oxidation is not sought to be used as a charge separation mechanism since it can decrease the transport properties of electrons and holes in the device by building up space charges. To prevent oxidation, devices should be produced

and handled in an oxygen-free environment or they should be encapsulated immediately after production.

2.1.4 Traps and Recombination

There are several processes after photoexcitation, that can prevent the electrons and holes created by photon absorption to be collected at the extracting electrodes of the solar cell. Some of these processes can occur right at the photoexcitation site before the electron and hole are sufficiently separated, while others can occur during charge transport through the film or at the interface of the organic film and the metal electrodes. In the following, the important loss mechanisms due to recombination and charge trapping will be described.

Photoluminescence

The singlet exciton created by photon absorption typically has a lifetime in the hundreds of picoseconds. In MEH-PPV, the lifetime is found to be about 550 ps [13] after which electron and hole recombine radiatively yielding photoluminescence. Since the electronic excitations of the chain are coupled to vibrations of the lattice, the photoluminescence spectrum has a vibronic structure, which is observed much better at low temperatures but is still observed at room temperature. Typically the phonons involved have an energy of ~0.2 eV.

The photoluminescence is quenched when excitons are dissociated. Mechanisms for exciton dissociation are described in Sections 2.1.2 and 2.1.3. Thus, the photoluminescence intensity of an organic photovoltaic device can be used to measure the charge separation efficiency and therefore the quality of the donor-acceptor interface. In cases of high photoluminescence, most of the excitons are created far away from a donor-acceptor interface so that they have no chance of being dissociated. In bulk-

heterojunction devices, the photoluminescence should be completely quenched since donor and acceptor have an exciton-dissociating interface throughout the bulk of the device. Photoluminescence quenching is used in this thesis as a valuable indicator of the formation of a bulk-heterojunction due to interdiffusion of donor and acceptor materials.

Traps

Traps in an organic film are spatially localized states that are energetically favorable for the charge carrier. They are usually divided into two groups – shallow and deep traps.

Shallow traps are states where the charge carrier is trapped for a certain time, after which it can be thermally released and can continue drift or diffusion. Therefore, the effective total flight time τ_{eff} through a distance L is the sum of the flight time τ_0 through a trap-free material and the average reside time τ_{tr} in a trap multiplied by the number of traps N in the path

$$\tau_{eff} = \tau_0 + N\tau_{tr} \qquad 2.1$$

This increase in effective flight time with trap density has a direct influence on the mobility of the charge carriers

$$\mu_{eff} = \frac{L}{\tau_{eff} E} = \frac{L}{(\tau_0 + N\tau_{tr})E} \qquad 2.2$$

Equation 2.2 shows that the mobility of the charge carriers decreases with increasing trap density. Since the mobility is inversely proportional to the resistance, the resistance for the charge carriers increases with higher trap densities.

Deep traps are states where, during a reasonable experimental time, charge carriers, once trapped, are not released any more. This does not only reduce the number of free charge carriers that can reach the electrodes, but it also leads to the buildup of space charges. These space charges can create an electric field that significantly hinders the transport of free charge carriers.

Traps can be introduced to the polymer by foreign atoms, impurities, or defects in the chain. A common example is oxidation of the polymer.

2.2 Photovoltaic Characterization of Organic Solar Cells

In the following, the main properties to characterize the photovoltaic behavior of organic solar cells are described. This section by no means gives a full description of all details. It is more intended to give the reader a basic understanding of organic photovoltaic devices. In some cases, inorganic and organic solar cells are compared to point out the difference between these two classes of devices. A good reference to learn more about organic photovoltaic devices is [36]. Even though it deals with inorganic thin film solar cells, [37] helps to interpret the I-V characteristics of photovoltaic devices and draw conclusions about the detrimental mechanisms.

2.2.1 Equivalent Circuit Diagram

The equivalent circuit diagram (ECD) is used to describe the electric behavior of complex devices in terms of basic ideal components such as current or voltage sources, resistors, diodes, and capacitors. Figure 2 shows the ECD typically used for inorganic solar cells. Since the loss mechanisms are basically the same for organic and inorganic solar cells, the ECD can be applied to organic devices, even though the specific physical processes are significantly different. The components shown can be described as follows:

- The current source G generates a current I_G. This current results from dissociation of excitons into electrons and holes after photon absorption. I_G does not take into account any recombination but only depends on the charge carrier creation efficiency.
- The shunt resistor R_{Sh} represents the recombination of electrons and holes near the exciton dissociation site before significant charge transport through the bulk has

occurred. The case of recombination at the extracting electrodes will be discussed below.

- The series resistor R_S takes into account the mobility of charge carriers in the bulk of the solar cell. The mobility will be influenced by defects and barriers as well as space charges in the device. R_S will also increase with thickness of the device since the distance that the charges have to travel to the collecting electrodes increases.
- The diode *D* describes the asymmetric conductivity in the solar cell. In inorganic devices, this is due to the pn-junction and its blocking behavior in one current direction. In organic cells, it can be due to a blocking contact at the semiconductor/electrode interface or a built-in field resulting from a donor-acceptor interface.

- The resistor R_L results when the solar cell is contacted to an external load. Alternatively, a source-measure unit can be connected to measure the I-V characteristics of the solar cell.

For an ideal solar cell, R_{Sh} would be infinitely large and R_S would be zero. Typical values for inorganic cells are R_{Sh} larger than 1000 Ohms and a few Ohms for R_S. These values can be significantly different in organic devices since the mobility is usually lower (increasing R_S) and charge recombination can be an issue (lowering R_{Sh}).

- 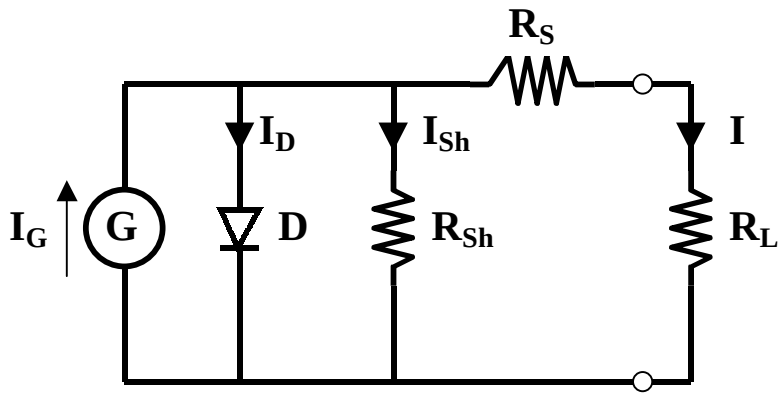

Figure 2 Equivalent circuit diagram for a typical solar cell.

Often, it is useful in organic solar cells to extend the ECD to take into account additional loss mechanisms. Figure 3 shows the extended ECD for an organic solar cell. The additional components are:

- A diode D_2 that takes into account a possible blocking contact at the electrode. This blocking contact can, for example, influence the extraction of holes at the ITO interface.
- A second shunt resistor R_{Sh2} that directly connects the electrodes. This shunt resistor accounts for possible recombination of charges at the extracting electrodes. In addition, this shunt resistor can result from direct conducting pathways between the electrodes, for example due to shorts in the film. When R_S is much smaller than either of the two shunt resistors, a splitting of the shunt resistance into R_{Sh} and R_{Sh2} is not necessary and both loss mechanisms can be represented by R_{Sh}.
- A capacitor C that accounts for charging and discharging effects in the device. Since the device area is usually much larger than the device thickness, the capacitance can become an important part of the device ($C=\varepsilon A/d$).

This ECD can be used to interpret I-V curves measured for a photovoltaic device. The observed shape can be related to certain components of the ECD, and from that conclusions can be drawn about the physical properties of the solar cell. From this, problems can be detected and possible changes and improvements on the devices can be deduced.

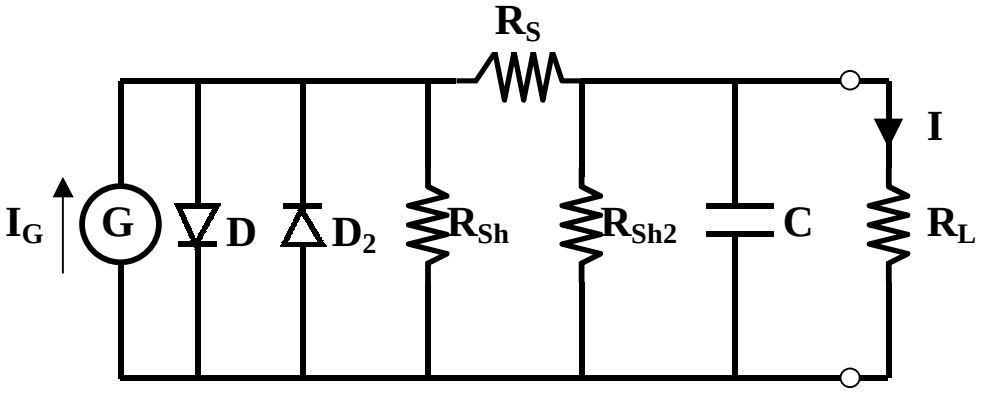

Figure 3 Extended equivalent circuit diagram for a solar cell.

2.2.2 Short Circuit Current , Open Circuit Voltage and Fill Factor

The typical current–voltage characteristic of a solar cell is shown in Figure 4. A few important points on the curve, that are used to determine the efficiency of solar cells, and to compare different cells are labeled in the graph:

- The intersection of the curve with the y-axis (current) is referred to as the short circuit current I_{SC}. I_{SC} is the maximum current the solar cell can put out under a given illumination power without an external voltage source connected. It is measured by connecting both electrodes to an ammeter.
- The intersection with the x-axis (voltage) is called the open circuit voltage (V_{OC}). V_{OC} is the maximum voltage a solar cell can put out. It is measured by connecting the illuminated solar cell to a voltmeter.
- I_{MP} and V_{MP} are the current and voltage at the point of maximum power output of the solar cell. I_{MP} and V_{MP} can be determined by calculating the power output P of the solar cell ($P=I*V$) at each point between I_{SC} and V_{OC} and finding the maximum of P.

Out of these quantities, the fill factor FF can be calculated. FF is defined as

$$FF = \frac{P_{\max}}{I_{SC} \cdot V_{OC}} = \frac{I_{MP} \cdot V_{MP}}{I_{SC} \cdot V_{OC}} \qquad 2.3$$

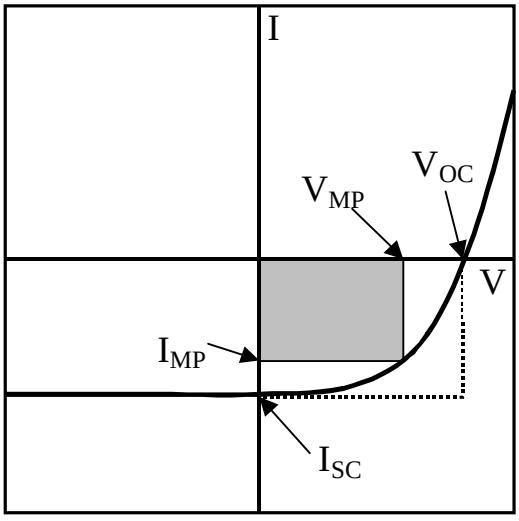

Figure 4 Current versus voltage characteristic of a solar cell under illumination.

The fill factor is the ratio of the rectangles given by the maximum power point and I_{SC} and V_{OC} (see Figure 4). The fill factor therefore gives a measure of the quality of the I-V characteristic of the solar cell. Its theoretical limits are between 0.25 (ohmic non-rectifying behavior of the solar cell) and 1. In practice, *FF* can even drop below 0.25 when a blocking contact is formed at one of the electrodes (compare extended ECD in Section 2.2.1).

In general, the overall efficiency of a solar cell is larger for larger *FF*. In the ideal limit of *FF* approaching 1 the solar cell puts out a constant maximum current at any voltage between 0 and V_{OC}.

2.2.3 Photoresponsivity, External Quantum Efficiency and Power Conversion Efficiency

An important property of a solar cell is the wavelength spectrum for which it absorbs light and produces a photocurrent. This spectrum helps determine whether a solar cell is capable of converting the available light illuminating it into electric energy. One possibility is to measure the photoresponsivity of the solar cell. The photoresponsivity is defined as the photocurrent extracted from the solar cell divided by the incident power of the light at a certain wavelength

$$PR(\lambda) = \frac{I_{SC}(\lambda)}{P_{source}(\lambda)} \qquad 2.4$$

The photoresponsivity spectrum $PR(\lambda)$ of a solar cell can be determined by scanning through the wavelength range available from the light source. Since the *PR* is normalized to the incident power of the light source, the *PR* spectrum is independent of the light source used and therefore the obtained data can be compared to other solar cells measured on different setups.

A different quantity often used to characterize the spectral behavior of solar cells is the external quantum efficiency *EQE*. The external quantum efficiency is defined as

the number of charges N_e extracted at the electrodes divided by the number of photons N_{ph} of a certain wavelength incident on the solar cell

$$EQE(\lambda) = \frac{N_e}{N_{ph}(\lambda)} \qquad 2.5$$

EQE can be calculated from the *PR*. Since

$$PR(\lambda) = \frac{I_{SC}(\lambda)}{P(\lambda)} = \frac{eN_e/\Delta t}{h\nu N_{ph}/\Delta t} = \frac{N_e}{N_{ph}}\frac{e}{hc/\lambda} \qquad 2.6$$

therefore

$$EQE(\lambda) = \frac{hc}{e}\cdot\frac{PR(\lambda)}{\lambda} \qquad 2.7$$

While the *EQE* just considers the conversion efficiency from incident photons to extracted electrons, the *PR* also takes into account the energy of the incident photons. Since the number of photons per given power decreases with shorter wavelengths, the *PR* will be lower than the *EQE* for shorter wavelengths. This effect is demonstrated in Figure 5 for an MEH-PPV single layer device.

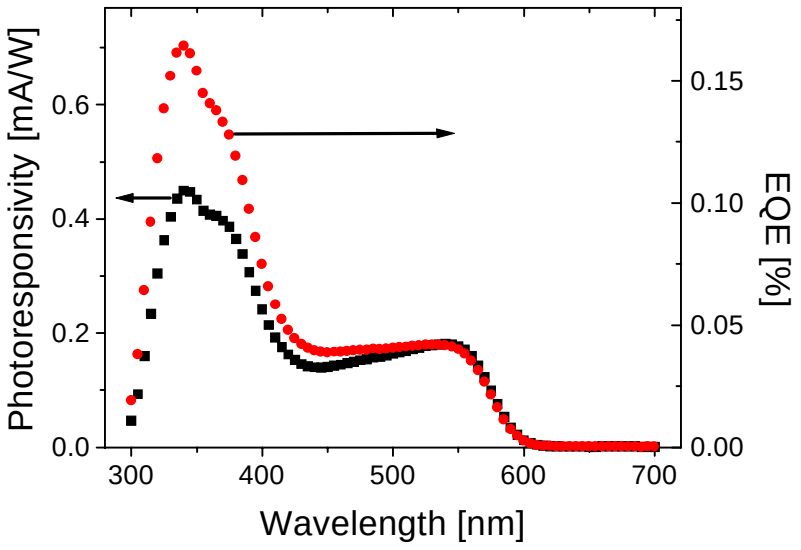

Figure 5 Comparison between the photoresponsivity (squares) and external quantum efficiency for an MEH-PPV single layer device.

The overall efficiency of a solar cell is called the power conversion efficiency. It is defined as the ratio of the electric power output of the cell at the maximum power point to the incident optical power. It can also be expressed in terms of I_{SC}, V_{OC} and FF

$$\eta = \frac{P_{electric}}{P_{light}} = \frac{FF \cdot V_{OC} \cdot I_{SC}}{P_{light}} \qquad 2.8$$

The power conversion efficiency can be calculated for monochromatic light illumination or for polychromatic illumination. Typically, the power conversion efficiency should be calculated for sunlight illumination. For this purpose, a light source that simulates solar illumination is needed, a so-called solar simulator. It consists of a white light source and a set of filters that simulate the solar irradiance. Due to the high cost of these systems, it was not available for studies in this thesis.

The band gap of a solar cell influences the maximum theoretical power conversion efficiency. The energy of the band gap determines the minimum energy of the absorbed photons. The lower the energy of the band gap, the more photons from the solar spectrum can be absorbed. On the other hand, electrons excited by photons with energies larger than the gap will initially be in states higher than the LUMO, but will lower their energy by emitting phonons (and therefore heating the device) until they reach the LUMO level. This process is called thermalization. In solar cells with lower band gap, the losses due to thermalization of the excited charges increase. Figure 6 shows how the power conversion efficiency depends on the band gap of a semiconductor for an ideal p-n junction device. Assigning reasonable values for the mobility and lifetime of charge carriers, the efficiency of a solar cell can be calculated as a function of band gap energy for the solar spectrum. The graph shows that there is a maximum in efficiency between 1.4 and 1.6 eV band gap energy. To achieve maximum efficiency of a solar cell, it is therefore important to utilize materials with an appropriate band gap. One of the attractions of organic solar cells is the ability to tune the band gap by derivatization.

It should be noted that if the power conversion efficiency is calculated for monochromatic illumination, these values can be significantly higher than the efficiency for solar illumination since losses due to limited absorption and thermalization are neglected.

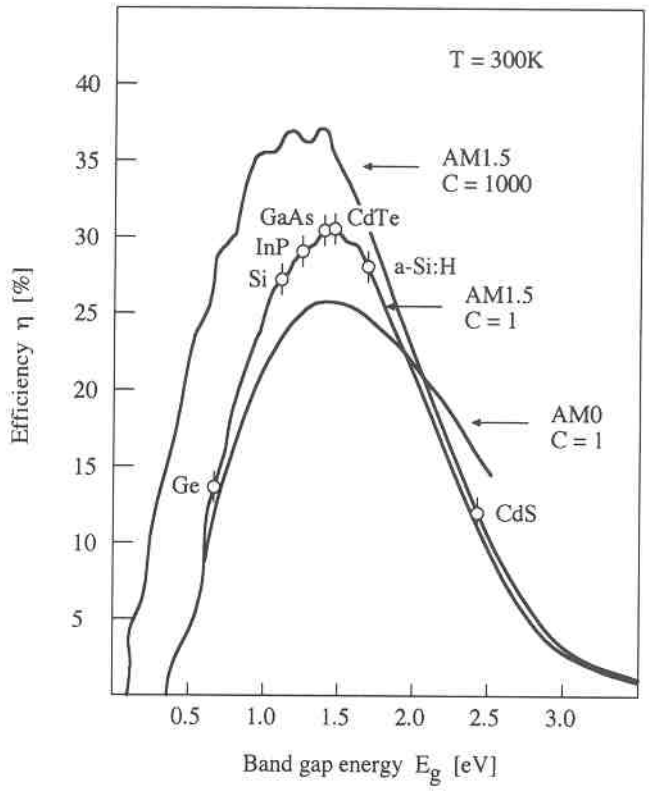

Figure 6 Ideal solar cell efficiency as a function of the band gap energy for the spectral distribution AM0 and AM1.5 with a power density of 1 sun, and for AM1.5 with 1000 sun (=844 kW/m^2). Reprinted with permission from *Semiconductors for Solar Cells*, by H.J. Möller, 1993, Artech House Publishers, Norwood, MA, USA. **www.artechhouse.com**

2.2.4 I-V Characteristics of a 'real' solar cell

The shape of I-V curves can reveal various undesirable mechanisms present in the solar cell. Often, different mechanisms can lead to similar shapes in the 4th quadrant of the I-V graph. It is therefore important that the cell is measured in reverse bias and also in forward bias at voltages $V>V_{OC}$. In the following, various examples of detrimental mechanisms are given, including a sketch of an I-V curve characteristic for each detrimental mechanism.

Low Shunt Resistance R_{Sh}

Figure 7 shows the effect of R_{Sh} on the I-V curve. The value of R_{Sh} can be found from the inverse slope in the 4th quadrant. The curve with the largest slope (solid) therefore has the smallest R_{Sh} and the smallest slope (dotted line) has the highest R_{Sh}. As is shown in Figure 7, a lower R_{Sh} reduces the open circuit voltage V_{OC} and the fill factor FF of the device. In addition, the slope in the 3rd quadrant increases with lower R_{Sh}. The short circuit current I_{SC} is not influenced by the change in R_{Sh} because R_{Sh} is still much larger than R_S and therefore the current through R_{Sh} can be neglected. In the limit of very small R_{Sh}, the V_{OC} will approach 0 and the FF will go to 0.25 (its theoretical limit).

High Series Resistance R_S

The influence of a high series resistance R_S on the I-V characteristic is shown in Figure 8. The I_{SC} and the FF are reduced with increasing R_S. Also, the slope in the 1st quadrant is reduced for higher R_S values. The V_{OC} remains unchanged for higher R_S since at V_{OC} the current flow is zero through R_S. The slope in the 3rd quadrant is still dominated by the R_{Sh} and therefore does not change with increasing R_S (assuming R_{Sh} is constant).

Low Short Circuit Currents I_{SC}

In addition to low R_{Sh} and high R_S, the current I_G generated by illumination of the solar cell can influence the I-V characteristic. Figure 9 shows how low I_G values can reduce V_{OC} and FF. Since I_G is influenced by the illumination intensity, V_{OC} and FF also depend on the light intensity shining on the solar cell. It is therefore very important to quote light intensities when publishing data about the efficiency of solar cells. Also, measurements under standard conditions (solar simulator) should be performed if available.

In practice there is often a combination of the mechanisms described above. It is not always easy to distinguish between the different detrimental mechanisms, especially for devices with rather low efficiencies.

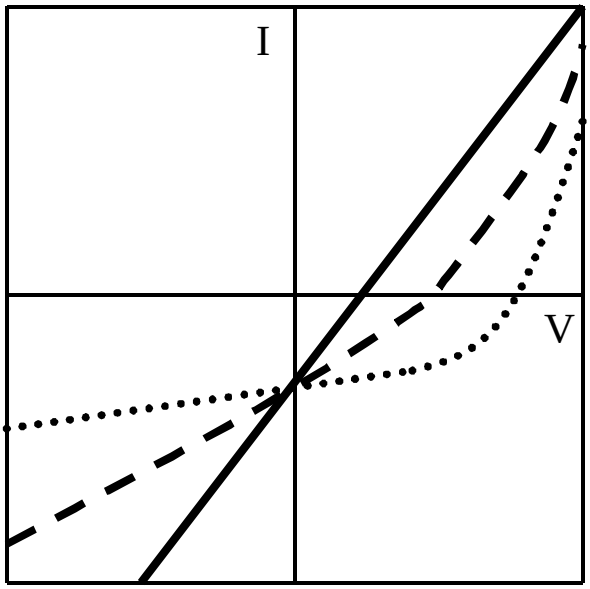

Figure 7 Effect of the shunt resistor on the I-V characteristic. The graph shows I-V curves for high (dotted), medium (dashed), and low (solid) values of R_{Sh}.

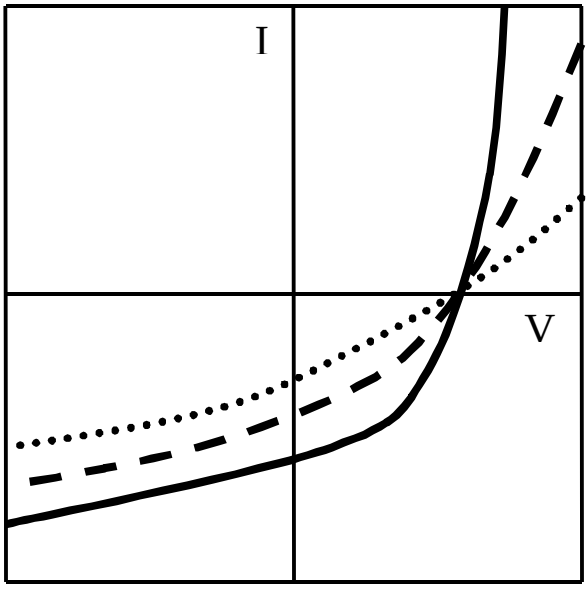

Figure 8 Effect of the series resistor on the I-V characteristic. The graph shows I-V curves for a low (solid), medium (dashed), and high (dotted) value of R_S.

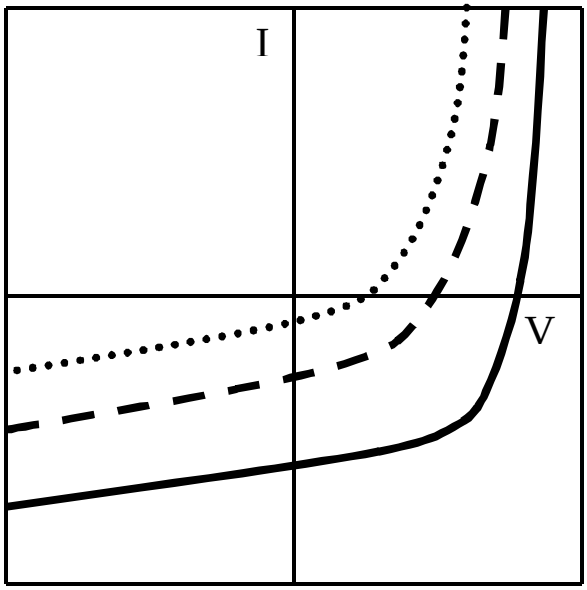

Figure 9 Effect of low short circuit currents on the I-V characteristic. The graph shows I-V curves for high (solid), medium (dashed), and low (dotted) values of I_{SC}.

2.2.5 Origin of the Open Circuit Voltage V_{OC}

The origin of the open circuit voltage in organic solar cells has been a subject of great debate and intensive studies. It is generally accepted that V_{OC} is related to the built-in potential of the photovoltaic device. The built-in potential is a parameter that influences charge dissociation, charge transport, and charge collection. The nature of the built-in field depends on the morphology of the active layer and is therefore different for various device structures.

In devices with the active layer consisting only of a pristine polymer, the built-in potential is created by the difference in workfunction *W* between the negative (low *W*) and the positive (high *W*) electrode. The upper limit for V_{OC} is given by the HOMO-LUMO gap of the polymer. Even in cases where the difference in *W* of the electrodes is larger than the HOMO-LUMO gap, no further increase in V_{OC} would be observed.

In bulk-heterojunction devices made out of donor polymers and acceptor fullerenes, recent studies [11,38] have shown a different origin of the V_{OC}. These studies suggest that the Fermi level of the negative electrode is "pinned" to the reduction potential of the fullerene. Fermi level pinning describes a situation where the workfunction of the metal electrode is pinned to the workfunction of the semiconductor. This occurs independent of whether the metal workfunction is higher or lower than the semiconductor Fermi level. This results in a V_{OC} that is directly related to the energy difference between the HOMO level of the donor and the LUMO level of the acceptor material. Varying the difference in workfunction between positive and negative electrode in these devices has only minor effects on the $V_{OC.}$ Therefore, in bulk-heterojunction devices the V_{OC} can be tuned by molecular engineering.

It should be noted here that the V_{OC} can be significantly reduced due to shorts between the positive and negative electrode and other recombination processes near the electrodes (represented by R_{Sh2} in Figure 3). Therefore, the V_{OC} can be used in addition to the shape of the I-V characteristic to evaluate the quality of the photovoltaic device.

2.2.6 Optical Filter Effect in Organic Films

The absorption in organic semiconducting materials is strongly wavelength dependent. This means that light that is subject to weak absorption can propagate through the whole film and is absorbed throughout the bulk of the material. On the other hand, light that is subject to strong absorption will be absorbed entirely in the surface layer, therefore not penetrating the bulk. The film in this case acts as an optical filter. This behavior can have severe consequences for the performance of organic photovoltaic devices. Since the photoexcitation has to occur in close vicinity of a donor acceptor interface (as described in Section 2.1.2), the filter effect creates conditions for the device structure and morphology. Early photovoltaic devices, which were built in a bilayer structure where there is a single interface between donor and acceptor materials, [18]

showed low efficiencies because a large fraction of the light was absorbed in areas far away from the donor acceptor interface.

Figure 10 uses the example of MEH-PPV to demonstrate this behavior. It shows the fraction of the transmitted light intensity as a function of film thickness for two different wavelengths, one that is strongly absorbed (490 nm) and another one (575 nm) that is close to the absorption onset at 600 nm. For a typical film thickness of 100 nm, less than 20 % of the strongly absorbed light will reach the donor acceptor interface where efficient charge separation can occur.

The filter effect can be easily observed in photoresponsivity data. While strong photoresponsivity is observed in regions of weak absorption or at the absorption onset, the photoresponsivity decreases in regions of strong absorption. Therefore this data can be used as a tool to characterize the extent of a bulk-heterojunction in photovoltaic devices.

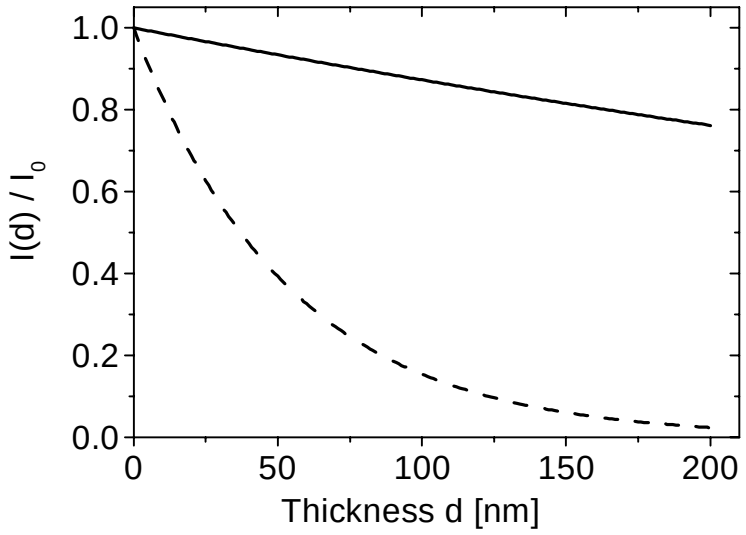

Figure 10 Fraction of the transmitted intensity through an MEH-PPV film. The solid line shows light of wavelength 575 nm, the dashed line shows light of 490 nm.

2.3 Heat Treatment

A good donor-acceptor interface is needed in organic photovoltaic devices for efficient charge transfer (see Section 2.1.2). In this work, the donor acceptor interface is studied by inducing an interdiffusion of donor and acceptor materials by heating devices in the vicinity of the glass transition temperature of the polymer donor material. In the following, topics related to this interdiffusion heat treatment such as heat and mass transfer as well as temperature gradients are discussed.

2.3.1 Heat Transfer

Heat can be transferred from a hot bath to a cold bath by conduction, convection or radiation. Since heat transfer due to radiation can be neglected in the hot stage setup used for interdiffusion heating, only conduction and convection will be described.

Conduction

Heat conduction is the energy transport through a medium initiated by a thermal gradient. On the atomic level, it is caused by the random movement of atoms. The kinetic energy of atoms in hotter regions is higher than in cooler areas. The energy can be transferred from hotter to cooler atoms, which leads to a heat current H along the temperature gradient. The heat current is defined as the heat rate that flows through a volume of cross-sectional area A and thickness L. It depends directly on the cross-section and the temperature gradient ΔT and inversely on the thickness

$$H = \frac{dQ}{dt} = kA\frac{\Delta T}{L} \qquad 2.9$$

where k is the thermal conductivity. The thermal conductivity is a material-specific constant that can also be temperature dependent.

Convection

Convection is a form of heat transfer that is a combination of two mechanisms. While there is still heat transfer due to random motion of atoms as described for conduction, there is also heat transport due to the macroscopic motion of the bulk. Since the bulk must be able to move, it follows that convection is only possible in fluids and gases.

A special case of heat transfer by convection is the case of an interface between a solid surface and a moving fluid or gas at different temperatures. Near the surface, the velocity of the moving phase will vary from zero at the interface to the common bulk velocity further away. Therefore, near the interface where the velocity is small, the heat transfer due to random atomic motion will dominate, whereas further away the heat transfer due to bulk motion will dominate. In this case, the heat current out of the surface of the solid phase into the moving phase is proportional to the temperature difference between the two phases and the surface area as described in equation 2.10.

$$H = \frac{dQ}{dt} = h \cdot A \cdot \Delta T \qquad 2.10$$

The constant of proportionality h is called the convection heat transfer coefficient. It depends on the thermodynamic properties of the moving phase, the nature of the motion (free or forced convection) and the surface geometry.

Thermal Contact Resistance

In a system where heat transfer occurs through an interface of two solid materials, a thermal contact resistance can occur. This resistance leads to a temperature drop across the interface. The origin of this contact resistance is the surface roughness of either surface of the two materials in contact, which leads to gaps at the interface. The contact resistance can be reduced by reducing the surface roughness or increasing the joint pressure. Since it is difficult to model the contact resistance, it is favorable to determine experimentally whether it is possible to neglect the effect of the interface.

Heat Transfer through a Single Wall

A glass slide that is placed on a hot stage and is in contact with a gas on the other side experiences a temperature drop. This situation can be modeled as a heat transfer through a single wall. Figure 11 shows the geometry of the setup. Assuming that the thermal contact resistance at the interface of the hot plate and glass is negligible, the heat current into the glass slide is

$$H_{in} = k_{glass} \cdot A \frac{T_{hp} - T_{surface}}{L} \qquad 2.11$$

where T_{hp} is the temperature of the hot plate and $T_{surface}$ is the temperature of the glass at the air interface. The heat current out of the glass slide is

$$H_{out} = h \cdot A(T_{surface} - T_{gas}) \qquad 2.12$$

From energy conservation it follows that in the steady state H_{in} has to be equal to H_{out} which leads to

$$k_{glass} \cdot A \frac{T_{hp} - T_{surface}}{L} = h \cdot A(T_{surface} - T_{gas}) \qquad 2.13$$

Solving for $T_{surface}$ gives

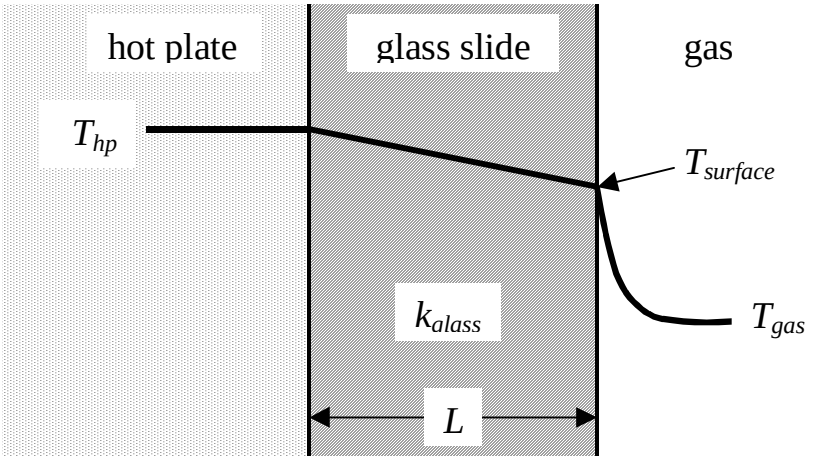

Figure 11 Temperature drop in a glass slide on a hot plate.

$$T_{surface} = \frac{k_{glass} T_{hp} + h \cdot L \cdot T_{gas}}{k_{glass} + h \cdot L} \qquad 2.14$$

This equation allows one to determine the actual temperature that a film on the glass slide experiences during thermal treatment. Any temperature gradient between the hot plate and the film can be accounted for.

2.3.2 Mass Transfer by Interdiffusion

The following section is based on the description of diffusion mass transfer from reference 39. Mass transfer in a mixture of materials is the phenomenon of particles of one species moving within the mixture as a result of a concentration gradient. In our photovoltaic devices, the two materials are the donor and the acceptor material. Starting from a bilayer system, mass transfer of one component into the other is induced by heating the devices, resulting in a mixture of the materials with a concentration gradient. The device can be treated as a stationary medium (i.e. the bulk of the device is not moving itself), so the mass transport is governed by interdiffusion.

The rate equation for mass diffusion in a binary mixture of species A and B is described by Fick's law

$$\vec{J}_A = -CD_{AB}\nabla f_A \qquad 2.15$$

where J_A is the molar flux of species A, C is the total molar concentration ($C=C_A+C_B$), D_{AB} is the binary diffusion coefficient and f_A is the mole fraction of species A ($f_A=C_A/C$). In addition, the conservation of species requires for a certain volume that

$$\dot{M}_{A,in} - \dot{M}_{A,out} + \dot{M}_{A,generated} = \dot{M}_{A,stored} \qquad 2.16$$

Here $M_{A,in}$ is the inflow rate of species A into the volume, $M_{A,out}$ is the outflow rate, $M_{A,generated}$ is the rate at which species A is generated (or annihilated) in a chemical reaction, and $M_{A,stored}$ is the rate at which species A is stored in the volume.
For the situation of the donor/acceptor bilayer system, the following assumptions simplify equations 2.15 and 2.16

- there are no chemical reactions increasing or reducing the number of fullerenes (species A) diffusing into the polymer bulk, therefore $M_{A,generated}$ is zero
- the diffusion occurs only in one spatial direction, reducing the problem to one dimension.

Using the simplification of one-dimensional transport, it is clear that for species A diffusing through a distance dx the relation between the molar flow rates at the beginning and end of dx is

$$J_{A,x+dx} = J_{A,x} + \frac{\partial J_{A,x}}{\partial x}dx \qquad 2.17$$

Also the rate at which A is stored can be replaced by

$$\dot{M}_{A,stored} = \frac{\partial C_A}{\partial t}dx \qquad 2.18$$

Plugging 2.17 and 2.18 into 2.16 gives

$$-\frac{\partial J_A}{\partial x} = \frac{\partial C_A}{\partial t} \qquad 2.19$$

Using Fick's law this becomes

$$\frac{\partial}{\partial x}(CD_{AB}\frac{\partial f_A}{\partial x}) = \frac{\partial C_A}{\partial t} \qquad 2.20$$

Equation 2.20 can be used to model the concentration of the fullerene in the polymer bulk as a function of position and time. To further simplify the problem, it is assumed that the C and D_{AB} are constant and that the position of the interface between polymer and fullerene is fixed in space (i.e. the polymer does not diffuse into the fullerene layer). In addition the fullerene layer is treated as an infinite reservoir of fullerene molecules.

With this, equation 2.20 reduces to

$$D_{AB}\frac{\partial^2 C_A}{\partial x^2} = \frac{\partial C_A}{\partial t} \qquad 2.21$$

With the initial condition that the concentration of A in the bulk of B is zero

$$C_A(x,0) = 0 \qquad 2.22$$

and the boundary conditions

$$C_A(\infty,t) = 0 \quad \text{and} \quad C_A(0,t) = C_{A,\max} \qquad 2.23$$

the general solution is

$$C_A(x,t) = C_{A,\max}[1 - erf(\frac{x}{2(D_{AB}t)^{1/2}})] \qquad 2.24$$

The actual diffusion of the fullerene molecules into the polymer bulk is more complicated than described in this model. Studies in Chapter 5 will show that diffusion of single fullerene molecules does not occur. Instead clusters of the fullerene in various sizes move into the polymer bulk, making a precise modeling of the diffusion behavior impossible.

The description of this simple diffusion model was introduced here to promote a general understanding and because a different choice of fullerene material for future studies might lead to the kind of diffusion that is described here. More comments about this can be found in Chapter 7.

Chapter 3

Experimental Methods and Materials

In this chapter, experimental methods and setups that were used for the work in this thesis are described. Also, the materials used in the photovoltaic devices are introduced. Properties such as the absorption and photoluminescence spectrum and HOMO-LUMO levels will be discussed. And the methods used for film thickness determination are specified.

3.1 Experimental Setups

3.1.1 Transmission-Reflection Measurements

Transmission and reflection data for the devices were obtained with a Filmetrics F20-UV thinfilm spectrometer system that can be used in transmission or reflection mode respectively. A Deuterium-Halogen light source DH2000 from Ocean Optics Inc. was used for illumination. From these spectra, the optical density (OD) can be calculated from

$$OD = -\log\frac{T}{1-R} \tag{3.1}$$

It is important to correct the transmission spectrum for reflection losses of the incoming light since polymer-fullerene films can have reflectivity of more than 25% at some wavelengths. The relationship between OD and the absorption coefficient α can be deduced from

$$I = I_0 e^{-\alpha d} \tag{3.2}$$

Since the transmission is

$$T = \frac{I}{I_0} \tag{3.3}$$

it follows that

$$OD = \alpha d \cdot \log(e) \tag{3.4}$$

Equation 3.4 shows that the optical density of a film is directly proportional to its thickness. Thus, the OD spectra can be used to determine the thickness of a film. This method of thickness determination was used throughout this work unless otherwise specified.

3.1.2 Photocurrent and I-V Curve Measurements

A schematic of the setup to measure photocurrents is shown in Figure 12. A 300 W Xenon arc lamp from Oriel Instruments is used as an illumination source. The light then passes through a CVI AB 301 automated filter wheel, which is equipped with appropriate filters and an aluminum disc to block the light beam. A CVI CM110 monochromator with 2400 grooves/mm, blazed at 400 nm is used to select a wavelength between 300 and 700 nm, which is then focused on the device by an UV lens. The resulting currents in the device are recorded by a Keithley 485 Autoranging Picoammeter.

To correct the photocurrent spectra for the intensity spectrum of the Xe lamp, a calibration measurement is needed. This is done by using a calibrated Si-photodiode from Oriel Instruments to determine the power $P_{source}(\lambda)$ of the light at each selected wavelength, using the known photoresponsivity spectrum of the photodiode (see Figure 13). With this and the photocurrent $I_{SC}(\lambda)$ the photoresponsivity can be calculated using equation 2.4. Figure 14 shows the power spectrum of the Xe lamp and for comparison the solar spectrum AM 1.5. Below 600 nm, the shape of the two spectra are similar; but above 600 nm, the Xe-lamp power is lower than the solar spectrum.

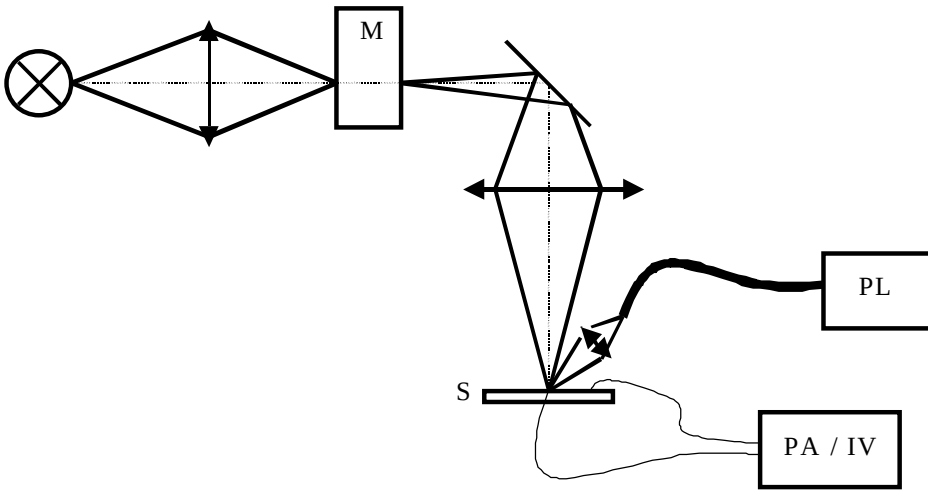

Figure 12 Photocurrent and I-V curve measurement setup

Regular recalibration every other week is necessary to account for slight changes in the power output of the light source with time due to wear of the cathode in the Xe lamp.

The same illumination setup is used to measure I-V curves of the devices. The picoammeter is replaced by a Keithley 236 Source Measure Unit. I-V curves were measured in the dark and under illumination at selected wavelengths.

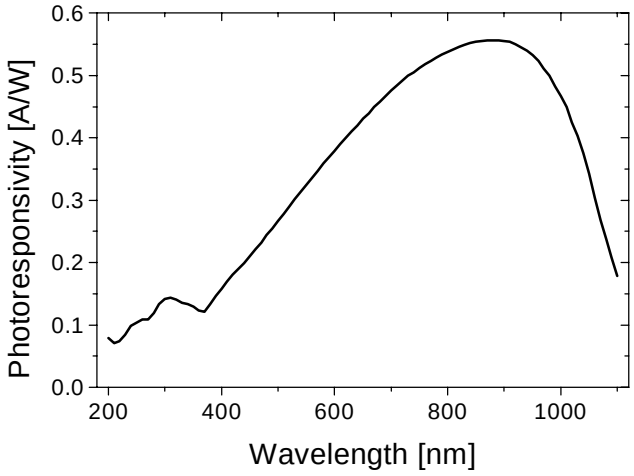

Figure 13 Photoresponsivity of the calibrated Si-photodiode.

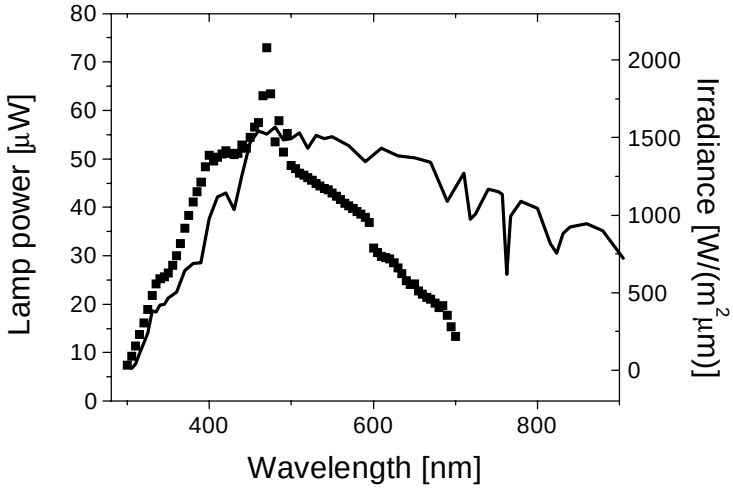

Figure 14 Power spectrum of the Xe-lamp. Squares show the power spectrum of the Xe-lamp setup as determined with a calibrated Si-photodiode. Also shown is the AM1.5 solar spectrum (solid line) (source : http://www.pv.unsw.edu.au/am1.5.html , Key Centre for Photovoltaic Engineering UNSW). The Xe-lamp shows similarities with the solar spectrum below 600 nm but is lower above 600 nm.

3.1.3 Photoluminescence Measurements

Photoluminescence was measured with an Ocean Optics S2000 fiber optics spectrometer. The sample was illuminated from the top with light from the Xe-lamp/monochromator setup described in the previous paragraph. The luminescence signal was picked up with a fiber that had a collecting lens mounted onto it, under an angle of 45^{o} with respect to the incident light.

3.1.4 Hot Stage for Heat Treatment

A hot plate was used to heat the samples and induce a diffusion of donor and acceptor materials from separate layers. In early experiments, a hot plate controlled by a CN9000A temperature controller by Omega Engineering Inc. was used. Later, a new hot stage was designed that was controlled by a CNi1622-C24 temperature controller by Omega Engineering Inc. enabling computer control and constant heat rates for the heating process. A hole in the stage made illumination of devices possible for *in situ* measurements during heating. During all heating processes, the hot plate was either in a N_2 glove box or in a plexiglass box filled with Argon.

Since the temperature controller can only control the temperature of the hot plate, it is necessary to determine the temperature difference between the hot plate and the surface of the glass slide. This can be done using equation 2.14. The following assumptions are made

- steady state
- thermal contact resistance is negligible
- free convection – since there is no forced air flow across the hot plate – therefore the convection heat transfer coefficient is h=25 $Wm^{-2}K^{-1}$
- thermal conductivity of float glass is k_{glass}=1 $Wm^{-1}K^{-1}$
- surrounding gas is at 20 ^{o}C

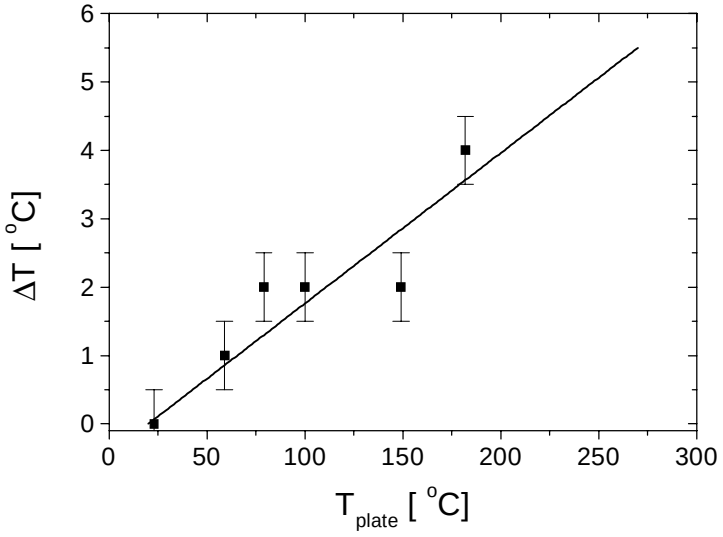

Figure 15 Temperature difference between glass slide surface and hot plate surface as a function of hot plate temperature (solid line). Also shown are experimental data (squares).

With this, the temperature difference between hot plate and glass surface can be calculated. Since the ITO layer and the polymer/fullerene film on the glass slide are both very thin (both are ~ 200 nm thick) compared to the glass slide thickness of 0.9 mm, the temperature gradient through these layers is negligible. Figure 15 shows the calculated temperature difference between hot plate and the polymer/fullerene film versus the hot plate temperature as well as actual measurements conducted on the hot stage at a few temperatures. The graph shows that the data is in good agreement.

3.1.5 Transmission Electron Microscopy

To study the film morphology of the organic devices Transmission Electron Microscopy (TEM) was used. In TEM, a focussed high-energy electron beam is transmitted through a thin sample. During transmission, some of the electrons interact with the sample, resulting in an electron "shadow" picture. This picture can be viewed on a fluorescent screen or recorded on film. Even though polymers and fullerenes are both

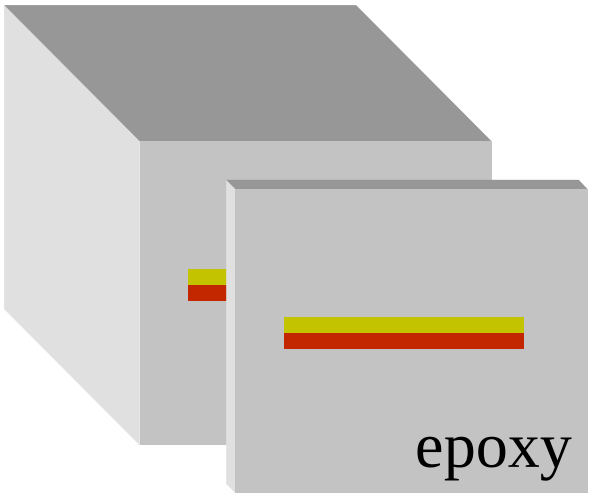

Figure 16 Polymer/fullerene bilayer imbedded in epoxy for TEM studies.

mainly carbon-based, a good contrast between the two materials was observed. The cross-sectional concentration distribution of polymer and fullerene throughout the film was of special interest. To study this distribution, films were imbedded in epoxy (EPOFIX purchased from Electron Microscopy Science) and afterwards slices of ~50 nm thickness were microtomed with a Reichert-Jung Ultracut E microtome showing the cross-section of the film. Figure 16 shows an illustration of the imbedded film and slices cut from it. Slices were placed on Cu TEM grids and studied in a Philips 420T TEM system at 100 kV. Images of the film morphology were recorded on film.

3.1.6 Auger Spectroscopy with Ion Beam Milling

Auger spectroscopy is a nice method to study the atomic composition of materials. In this method, a high-energy electron beam is focussed on a sample. The high-energy electrons free electrons from the atomic shells of the atom. To refill these energy states, there are two possible processes (Figure 17):

- An electron from a higher state falls down to the lower state emitting a x-ray photon of energy $h\nu = E_{low} - E_{high}$.

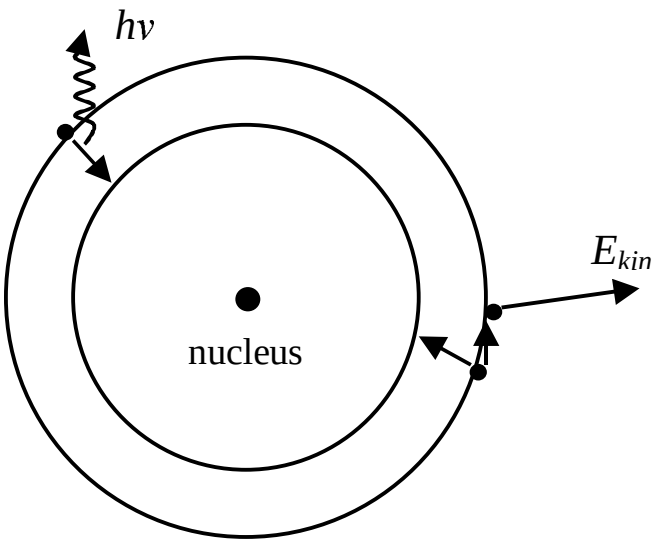

Figure 17 Two possible processes to refill an empty state in a lower energy shell.

- An electron falls down from a higher state to the lower state and instead of emitting a photon, the energy is transferred to another electron, the so called Auger electron. The Auger electron now has the energy to escape from the atom and travel with a characteristic kinetic energy given by

$$E_{kin} = E_{transferred} - E_{high} = (E_{low} - E_{high}) - E_{high} = E_{low} - 2E_{high} \qquad 3.5$$

In Auger spectroscopy, the kinetic energy of the secondary electrons is measured. Since the kinetic energy is unique for each element, the types of atoms present in the tested area are revealed. From the number of Auger electrons counted, the concentration of the specific element in the tested area can be calculated.

The Scanning Auger Spectroscopy system (model 610 Perkin-Elmer) is used to study the surface layer of the sample. The penetration depth of the electron beam is typically 5 nm. To get a depth profile of the atomic composition, Argon ion beam milling is used. After each Auger scan of the surface, the surface layer is removed and a new Auger scan is started. In the scans presented in this thesis, 2.5 nm of the film were removed during each etching step. Unfortunately, the etching process does not remove a flat layer so that some noise in the depth profile is introduced due to surface roughness.

Since the fullerene is entirely carbon based and the main constituent of polymers is also carbon, the polymer needs to have another characteristic element so that one can

distinguish between the two components during the Auger spectroscopy depth profile. Since the system used in this study can not detect hydrogen, the polymer must contain another element. During our studies, we discovered that the sensitivity of the system towards oxygen in MEH-PPV was not sufficient enough to get results beyond the noise level, but sulfur in P3OT was easily detected. For chemical structures of MEH-PPV and P3OT, see section 3.2.

3.2 Device Structure

The general device structure of organic photovoltaic devices studied in this work is shown in Figure 18. The substrate material in this case is glass. On the glass is the actual photovoltaic device consisting of the active layer being sandwiched in between the positive (anode) and negative (cathode) electrodes. Illumination of the device in this case would be through the glass substrate and the anode. The cathode should be reflecting so that light that is not absorbed by the active layer is reflected back into the device and can be absorbed when it passes through the active layer the second time. This choice of device structure is very common for organic solar cells but is not the only one possible.

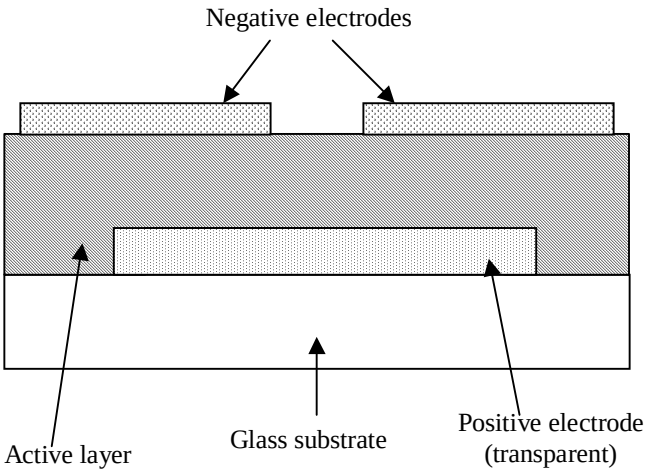

Figure 18 General device structure of an organic photovoltaic device. The active layer is sandwiched between the positive and negative electrode and is illuminated through the substrate onto an overlapping region of the two electrodes.

The workfunction of available transparent materials typically limits the choice of making the cathode the transparent electrode. A way around this problem is to evaporate thin metal layers that are semitransparent. In this case, illumination through the negative top electrode is possible. Another way of varying the structure is to put the non-transparent cathode down on the substrate and deposit the transparent anode on top of the active layer. This approach is usually not chosen because the deposition of the commonly used indium tin oxide as the anode is not as easy as the evaporation of metals as top electrodes.

There are different possibilities for the composition of the active layer. Figure 19 shows several morphologies that can be used. The simplest approach is to have a layer made out of a single material. Usually, devices using this approach show low efficiencies because there is only little charge separation in the absence of a donor-acceptor interface. The next approach shown is a bilayer system of a donor and acceptor material forming a heterojunction. In these devices, charge separation is limited to a region at the interface. Depending on the thickness of the two layers, the interface region can be only a small fraction of the total bulk of the active layer. Therefore, these devices also show rather low efficiencies. The other two morphologies shown are a blend of donor and acceptor material and a bilayer with a diffuse interface. Both device morphologies have a donor-acceptor interface throughout the bulk therefore forming a so-called bulk-heterojunction. These devices show improved efficiencies over single and bilayer devices.

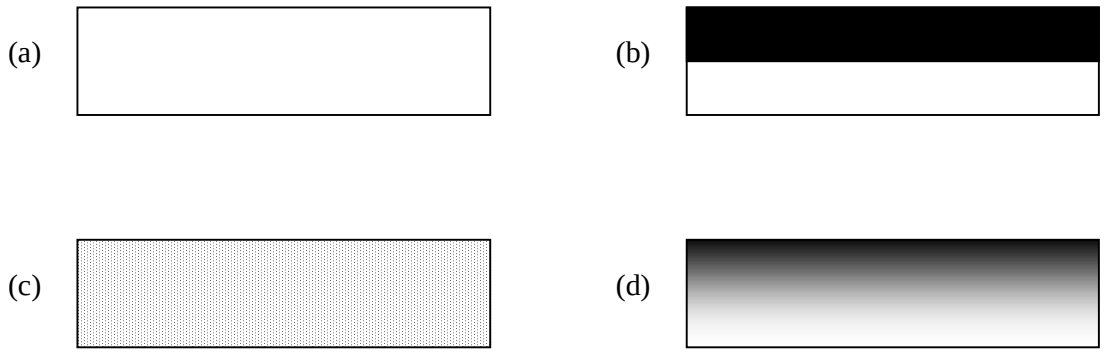

Figure 19 Various structures of the active layer. The active layer can be made out of (a) a single material, (b) a bilayer with a distinct interface, (c) a blend of donor and acceptor materials or (d) a bilayer system with a diffuse interface and a concentration gradient of donor and acceptor materials through the bulk.

3.3 Donor Materials

Typically, semiconducting polymers are used in organic photovoltaic devices as the donor material. They have good hole-conducting properties but don't conduct electrons very well. The absorption is usually in the visible part of the spectrum. The polymer materials used in this thesis will be introduced in the following.

3.3.1 MEH-PPV

The semiconducting polymer poly(2-methoxy-5-(2'-ethylhexyloxy)-1,4-phenylenevinylene), hereafter referred to as MEH-PPV, has been intensely studied over the last decade for application in organic light emitting devices [40,41,42] as well as organic photovoltaic devices [43,44,45]. It is a soluble derivative of the insoluble polymer poly(phenylene vinylene) (PPV). The MEH-PPV used in our study is a copolymer purchased from H.W. Sands Corp. with a molecular weight of ~85,000. The chemical structure of MEH-PPV is shown in Figure 20. It is readily soluble in most organic solvents. For this thesis, solutions were prepared in chlorobenzene unless otherwise stated. Typically, a solution concentration of 1 % wt/vol (1 % wt/vol is 1 g of solute per 100 ml of solvent) was prepared, and the MEH-PPV film thickness was varied by varying the spin speed during spin coating. The average film thicknesses obtained for

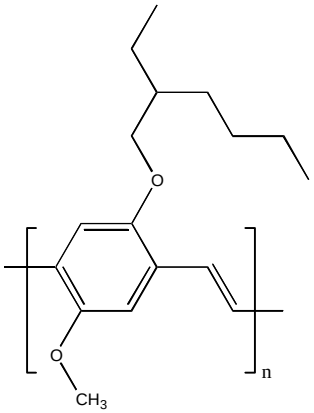

Figure 20 Chemical structure of MEH-PPV. The picture shows one repeat unit of the polymer.

Table 1 Average film thickness of MEH-PPV single layers spin-coated at various spin speeds. The chlorobenzene solution concentration in all cases was 1 % wt/vol.

spin speed [rpm]	2000	3000	4000
film thickness [nm]	110	90	70

these conditions using 8 drops of solution are shown in Table 1. The film thickness of each device produced for this thesis was confirmed by absorption measurements during the device production.

Figure 21 shows the optical density and the photoluminescence of a 90 nm single MEH-PPV layer on a glass substrate. The absorption spectrum shows an onset at 590 nm. The absorption peak is at 490 nm. The dramatic increase in absorption below 300 nm is due to the strong absorption of the glass substrate that cuts off any transmission below 300 nm. The photoluminescence (PL) is red-shifted compared to the absorption and shows a vibronic structure with peaks at 592 nm and 633 nm. The energy levels in MEH-PPV are 2.9 eV for the LUMO and 5.3 eV for the HOMO level resulting in an energy gap of 2.4 eV [46].

A Filmtek thin film measurement unit was used to get an initial thickness calibration for MEH-PPV. The Filmtek measures the transmittance and reflectance of a film and then models the refractive index and the extinction coefficient (*n* and *k*, respectively). The output data includes *n* and *k*, which should be thickness independent, and the film thickness. The data in Figure 22 show the OD of two MEH-PPV films. The OD clearly shows the difference in film thickness, one film being 117 nm thick and the other being 83 nm. Figure 23 shows the corresponding *n* and *k* data obtained with the Filmtek. The fact that *n* and *k* match for the two different films shows the reliability of the measurements. Knowing the OD and the thickness *d* of the MEH-PPV film, the absorption coefficient $\alpha(\lambda)$ of MEH-PPV was calculated using equation 3.4. $\alpha(\lambda)$ was found to be 18×10^4 cm^{-1} at 490 nm. This $\alpha(\lambda)$ was then used to calculate the thickness of other films from their OD spectrum.

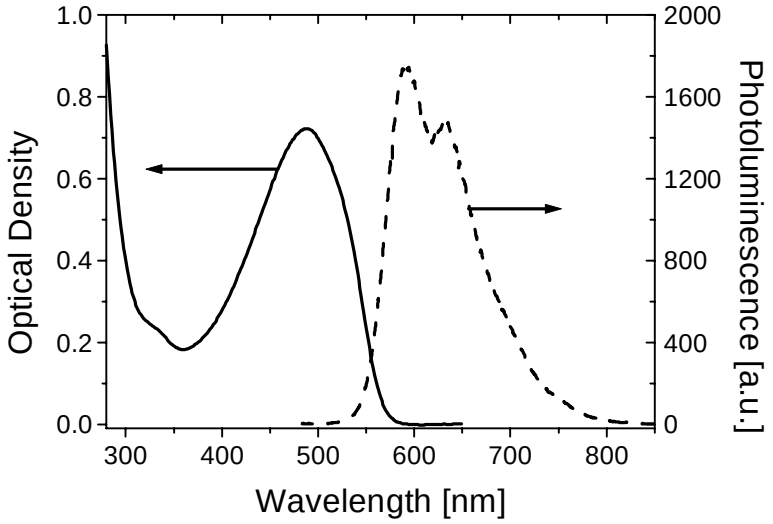

Figure 21 Optical density (solid) and photoluminescence spectrum (dashed) for a pristine MEH-PPV polymer layer. The absorption onset is at 590 nm and peaks at 490 nm. The photoluminescence is red-shifted and shows a vibronic structure with peaks at 592 nm and 633 nm. The films used to obtain the data shown had a film thickness of 90 nm.

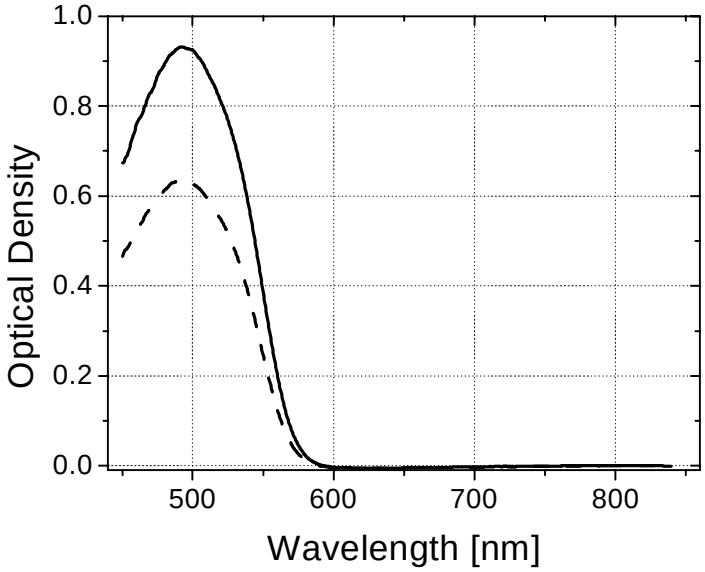

Figure 22 Optical density for two MEH-PPV films on glass substrates measured with the Filmtek. One film has a thickness of 117 nm (solid) and the other 83 nm (dashed).

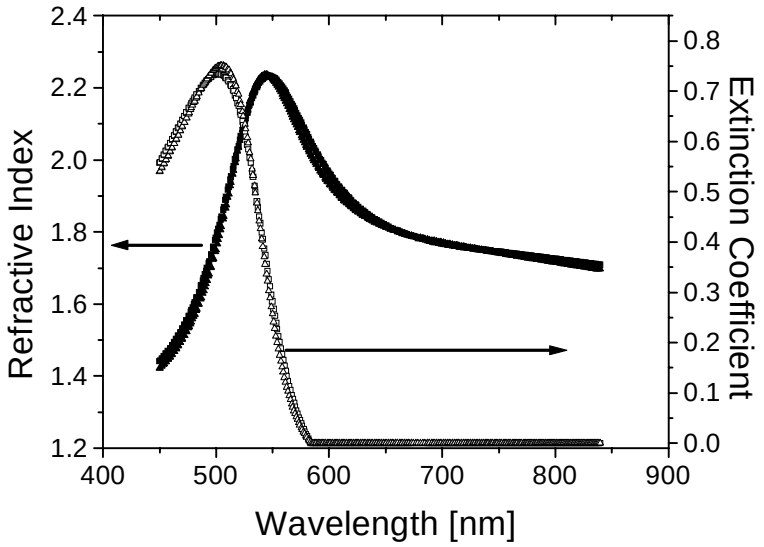

Figure 23 Refractive index and extinction coefficient for two MEH-PPV films on glass substrates. Solid symbols show the refractive index and open symbols show the extinction coefficient. Squares show data belonging to the 117 nm film and triangles belong to 83 nm film. The n and k data for both films are the same showing the good reproducibility of the used model.

To check the thickness calibration, a Dektak surface profilometer was used. An MEH-PPV film was prepared on a glass substrate and a thin line of the polymer film was scratched off, creating a small well. The profilometer scanned a region across this well determining the difference in height to the bottom of the well (glass substrate). Figure 24 shows the results of a surface scan. The film thicknesses found with the profilometer were about 10 nm thinner than was expected from absorption measurements (for both a 95 nm and a 116 nm film). This slight difference is most likely due to small deformation of the film at the tip contact area because of the softness of the polymer. Altogether, the thickness measurements of the Filmtek and Dektak system are in good agreement.

A material parameter important for the interdiffusion experiments is the glass transition temperature T_g of MEH-PPV. The value for T_g supplied by the manufacturer is 230 ^{o}C. This was confirmed by DSC measurements.

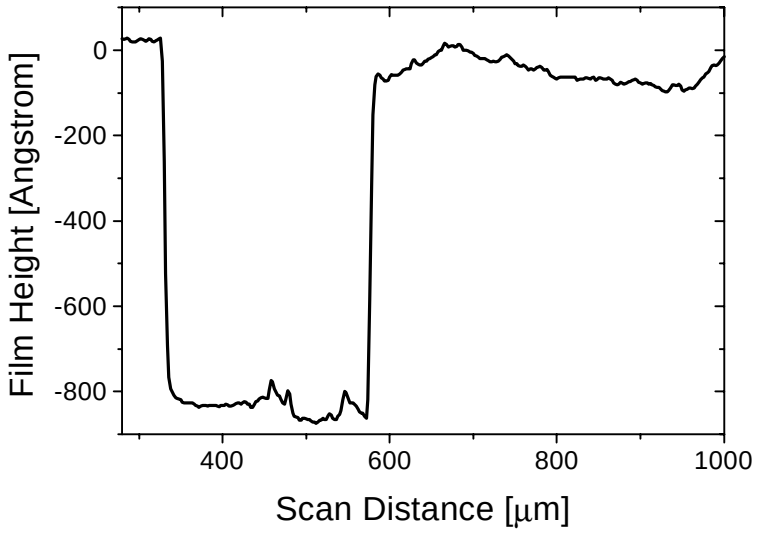

Figure 24 Surface scan of an MEH-PPV film on a glass substrate. Part of the film was removed to get the height difference between the top of the film and the glass substrate. The graph shows part of the scan across the well area. The step width of the profilometer was 2 μm with a total scanned length of 2 mm. The thickness of the film from absorption data was 95 nm.

3.3.2 P3OT

Poly(3-octylthiophene-2,5-diyl), hereafter referred to as P3OT is another semiconducting polymer that has been intensely studied in photovoltaic device applications [47,48,49]. The chemical structure of P3OT is shown in Figure 25. P3OT was purchased from Sigma-Aldrich Co. (lot number 02918BA) with a molecular weight of ~142,000 in a regioregular structure (>98.5% head-to-tail regiospecific conformation). In this form, P3OT is micro-crystalline (whereas regiorandom P3OT is amorphous) [50,51] therefore exhibiting a melting point T_m as well as a T_g. T_m was determined to be 187 ^{o}C by DSC. T_g could not be determined but is expected to be below 100 ^{o}C [52]. Films were prepared by spin-coating P3OT from a 1.5 % wt/vol chloroform solution. Typical film thickness is 95 nm at a spin speed of 3000 rpm applying 6 drops.

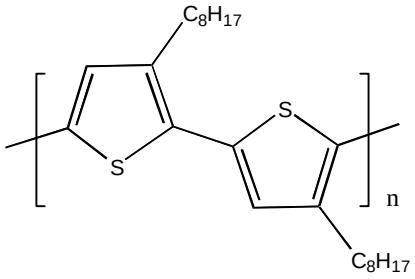

Figure 25 Chemical structure of P3OT. The picture shows one repeat unit of the polymer.

The OD and PL spectra are shown in Figure 26. The OD spectrum shows the absorption onset at 670 nm and the peak absorption at 512 nm. The PL is red-shifted compared to the absorption with a vibronic structure and shows a peak at 670 nm and a shoulder at 705 nm. Again, the sharp increase of absorption below 300 nm is due to strong absorption of the glass substrate.

The HOMO and LUMO level in P3OT are 4.9 and 2.8 eV respectively resulting in a HOMO-LUMO gap of 2.1 eV [53]. Because the HOMO-LUMO gap of P3OT is smaller than for MEH-PPV, P3OT can absorb photons with lower energy than MEH-PPV can absorb, as shown in the OD spectra.

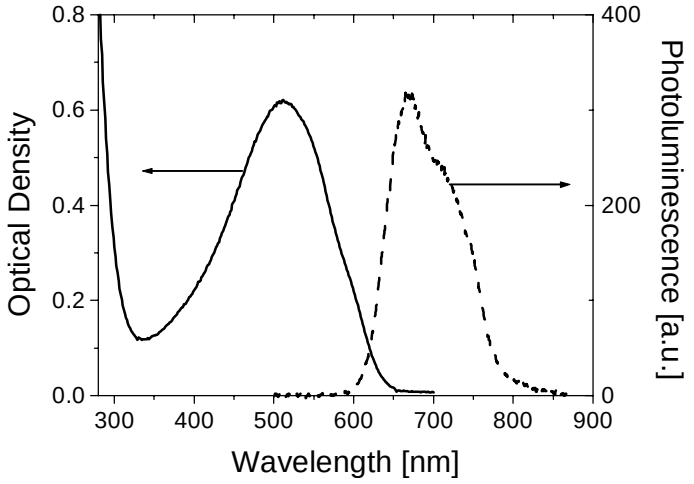

Figure 26 Optical density (solid) and photoluminescence spectrum (dashed) for a pristine P3OT polymer layer. The absorption has an onset at 670 nm and peaks at 512 nm. The photoluminescence is red-shifted and shows a vibronic structure with a peak at 670 nm and a shoulder at 705 nm. The films used to obtain the data shown had a film thickness of 100 nm.

The thickness of P3OT layers was determined from OD data and the absorption coefficient using equation 3.4. The same Dektak surface profilometer as described in section 3.3.1 was used to determine $\alpha(\lambda)$ of P3OT. The P3OT films were prepared on glass slides and part of the film was removed with an Acetone-soaked cotton tip applicator to get a clean edge of the film. The $\alpha(\lambda)$ was determined to be 14×10^4 cm^{-1} at 512 nm.

3.4 Acceptor Materials

The buckminsterfullerene C_{60} was used as an electron accepting material in this work. Its electron accepting properties due to ultrafast charge transfer have been intensely studied (see Section 2.1.2). The chemical structure of C_{60} is shown in Figure 27. C_{60} powder was purchased from MER Corporation (Tucson, Arizona) and used without additional purification. Due to its low solubility, C_{60} can not be spin-coated. Instead, C_{60} was sublimed in a vacuum evaporator from Ladd Research at pressures below 3×10^{-6} Torr. The C_{60} sublimation source is shown in Figure 28. C_{60} powder was filled into a quartz glass tube, which was inserted in a brass container to achieve homogeneous heating of the whole quartz tube. The brass container was kept in a thin ceramic coat that was used to prevent shorting of the tungsten heating filament with the metal container.

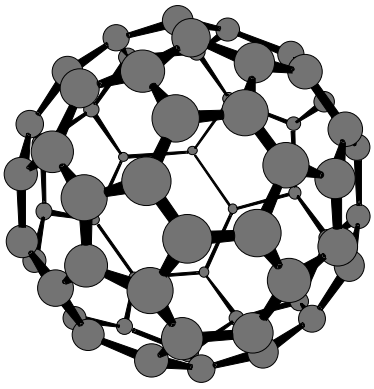

Figure 27 Chemical structure of the Buckminsterfullerene (C_{60}).

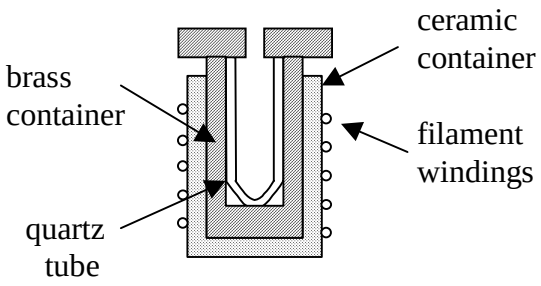

Figure 28 Schematic of the C_{60} sublimation source.

The brass container has a small 2 mm diameter opening for the C_{60} to escape. This way, a good directionality of the subliming C_{60} is achieved, reducing use of material. The substrate was kept 7.5 cm above the C_{60} source. The disadvantage of this technique is that the C_{60} film has a variation of thickness from the center to the edge of the slide.

To determine the absorption coefficient of C_{60}, which is needed for thickness calibration of the films, a very thick C_{60} film was prepared on a glass slide using a much longer sublimation time than that used for fabrication of PV devices. The reflection measurements showed several interference fringes as can be seen in Figure 29. From the maxima and minima, the optical path length (thickness * refractive index) was calculated from

$$2dn = \frac{\lambda_1 \lambda_2}{\lambda_1 - \lambda_2} \qquad 3.6$$

where λ_1 and λ_2 are the positions of 2 consecutive maxima or minima. With this equation and the refractive index n, the thickness of the film can be determined. The refractive index for C_{60} in this wavelength range is $n=2$ [54]. The thickness of the film shown here was determined to be 1.08 micrometer. This provides an absorption coefficient of 6×10^4 cm^{-1} at λ=435 nm. The thicknesses of other C_{60} films can be calculate from the *OD* spectrum using this absorption coefficient and equation 3.4.

The HOMO level in C_{60} is 6.1 eV and the LUMO level is 3.7 eV resulting in a HOMO-LUMO gap energy of 2.4 eV [55].

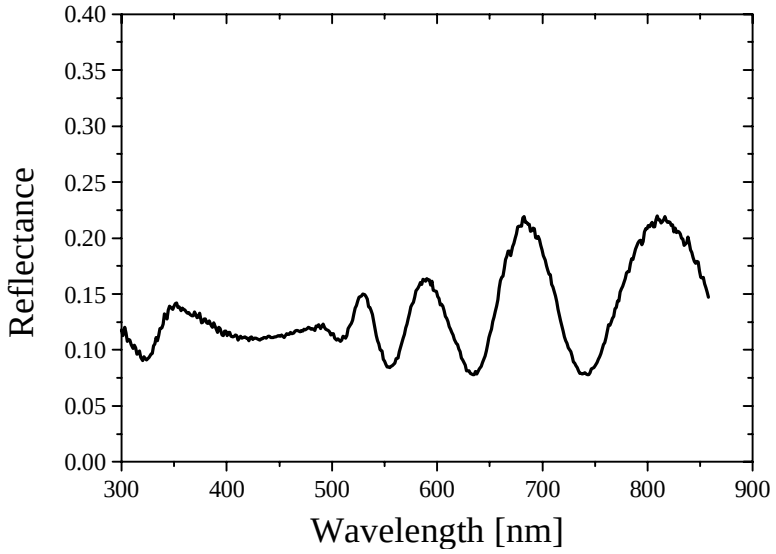

Figure 29 Reflectance spectrum of a thick C_{60} film. Several interference fringes are observed due to multiple beam interference.

3.5 Electrode Materials

The charges created by photon absorption are collected at the electrodes of a photovoltaic device. One electrode has to be transparent so that photons can enter the device and be absorbed in the active layer. The other electrode should preferably be a good reflector. In that case, photons that were not absorbed will be reflected back into the active layer and have another chance to be absorbed. Usually, the electrode materials are chosen to have different workfunctions. The difference in workfunction creates a built-in field that helps collect charges. For this to work, the anode should have a higher workfunction than the cathode so that the band bending gives electrons and holes a preferred travel direction. This band bending is illustrated in Figure 30.

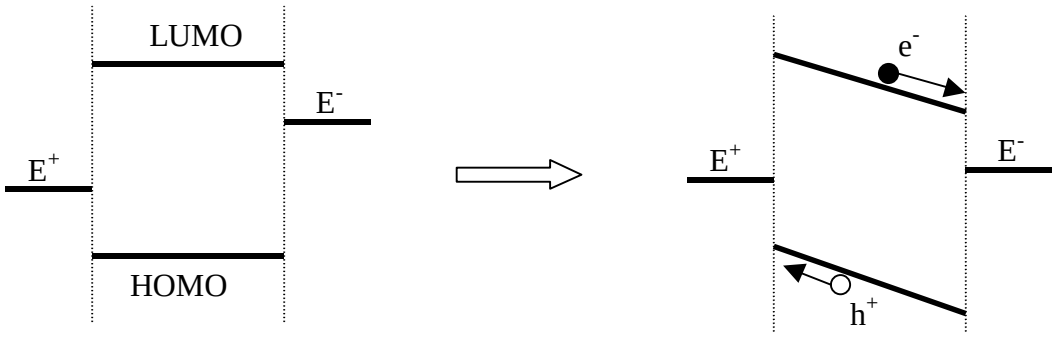

Figure 30 Energy level diagram for a single material active layer. On the left, the diagram shows the workfunctions of the positive E^+ and negative E^- electrode and the HOMO-LUMO level of the active layer before the materials are in contact. On the right, the layers are in contact with each other and band bending occurs creating a preferential travel direction for electrons and holes.

3.5.1 Positive Electrode

The positive electrode is made out of a two-layer system. The first layer is indium tin oxide (ITO) on a glass substrate. On top of that, a layer of the conducting polymer complex poly(3,4-ethylenedioxythiophene) : poly(styrenesulfonate) (hereafter referred to as PEDOT) is spin coated.

The ITO-coated glass substrate is purchased from Delta Technologies with a sheet resistance of R_S = 8-12 Ω at 150-200 nm ITO layer thickness. R_S is defined as the bulk resistivity of the material divided by the thickness of the layer. The total resistance of a thin film can be found by multiplying R_S with the length of the film and dividing by its width. The glass substrate has an antireflection coating on the back. To prepare the slides, the ITO is etched off the sides of the slide to prevent shorting between the Al top electrode and the ITO when making electrical contacts to the Al. This etching is done by covering a 1 cm wide strip of the ITO in the center of the slide with electrical tape to protect the ITO in this region from the etching acid. Also, the antireflection coating on the back of the substrate is covered with electrical tape. The slide is then submerged in a 1:1 (hydrochloric acid (HCl at 37 %) : deionized water) solution for 45 minutes to remove ITO from the uncovered parts of the slide. After the etching process the slides are cleaned in a base solution made of 370 g water, 41 g hydrogen peroxide, and 69 g

ammonium hydroxide by sonicating for 30 minutes. Afterwards the slides are rinsed with deionized water and dried with prepurified nitrogen gas.

Reported values for the workfunction of ITO vary between 4.4 – 4.8 eV [56,57]. In this thesis, the workfunction was assumed to be 4.7 eV.

PEDOT was purchased from Bayer Corp. in an aqueous solution. The solution was filtered before use with a 0.4 micron nylon syringe filter. Films were prepared by spin coating PEDOT on top of the ITO. The film thickness was typically 50 nm. After the PEDOT film has dried, it is not easily removed so that spin-coating an additional layer will not wash off the PEDOT.

The PEDOT layer has a dual function in the devices. First, it smoothens the ITO surface, which helps to prevent shorts between the positive and the negative electrode, especially if the active layer is very thin. In addition, the PEDOT has a higher workfunction (5.2 eV [58]) than ITO, which gives a better alignment of the workfunction with the HOMO level of the active layer for the polymers used in this thesis.

3.5.2 Negative Electrode

For the negative electrode, aluminum was evaporated under vacuum. Al evaporations were done in a vacuum evaporator from Ladd Research at pressures below $4x10^{-6}$ Torr. Al granules were placed in tungsten filaments (ME17-3x.025W from R.D. Mathis Company) and evaporated at currents of 35 A. The Al film thickness was controlled with a TM-100 thickness monitor from Maxtek Inc. to be 200 nm. Typical deposition rates were between 1 and 2 nm per second. The work function of Al is 4.3 eV [59], which is lower than the ITO/PEDOT workfunction. Often, even lower workfunction materials like Ca (2.9 eV [60]) are used for the negative electrode. Since these metals have the tendency to be unstable in air, they have to be encapsulated or a protective layer has to be evaporated on top of them. The studies in this thesis are limited to Al electrodes.

Chapter 4

Preliminary Heating Studies

Initial heating tests were carried out to determine the ability to obtain high-quality, reproducible PPV films and to establish the stability of the pure PPV films through the heating cycle. These tests were performed with PPV films converted from precursor PPV, which was spin coated from the sulfonium precursor. It was later decided to use the soluble PPV derivative MEH-PPV. The main reason for this decision was that MEH-PPV does not need the 12 hour thermal conversion needed for PPV. Also, there were issues with the film quality of spin-cast PPV films due to the hydrophobic properties of ITO, leading to inhomogeneous film coverage on the substrate. The photoluminescence of a PPV film spin-cast at 2000 rpm from an aqueous 30 mMol PPV precursor solution on ITO was measured under Argon-environment at varying temperatures. The experiments were meant to determine the reproducibility of the

photoluminescence measurements and to determine the PPV behavior with varying temperature. It is important to understand the effect of temperature of a pure PPV film before examining the interdiffusion process at elevated temperature of films containing PPV and C_{60}. In particular, we wanted to determine the dependence of the luminescence on temperature and whether the PPV survived the temperature excursion, as evidenced by no loss of photoluminescence at the end of the heating cycle.

4.1 Temperature Dependence of the Photoluminescence

To establish the temperature dependence of the photoluminescence, a PPV film on an ITO-covered glass slide was heated on a hot plate in an Argon-filled box. The excitation beam was at 400 nm (2.9 mW/cm^2). Figure 31 shows the PL spectra at room temperature and various temperatures up to 200 ^{o}C. The PL clearly decreases and shifts to shorter wavelengths with increasing temperature.

To further investigate the temperature dependence, the peak positions and peak intensities of the first and second peaks were determined from the data shown in Figure 31. The temperature dependence of the peak intensity is shown in Figure 32. The graph shows that the peak intensity decreases in a fairly linear fashion with increasing temperature. The peak position also shifts in a linear manner towards shorter wavelengths with increasing temperature as can be seen from Figure 33.

This temperature dependence of the PL has to be taken into account if the interdiffusion of an acceptor material is monitored *in situ* during the heating process. Since the PL is also quenched by improving the interface between donor and acceptor material, the collected data has to be corrected for the temperature dependence of the pristine polymer.

In all cases shown in this chapter, the PL spectrum fully recovered to its original intensity. An example of this recovery is shown in Figure 34. The film was heated up to 180 ^{o}C. The PL was measured before, during, and after heating. The graph only shows the spectra before and after the heating cycle. The fact that they are identical shows that there is no degradation of the polymer due to oxidation or thermal decomposition. If the

PPV film oxidized during the heating, the PL would be quenched permanently. Since the oxygen acts as a dissociation site for excitons (see Section 2.1.3), the radiative recombination of excitons would be reduced resulting in a lower PL. This result also shows that the used Argon box provides an oxygen-free environment that can be used safely for heating experiments.

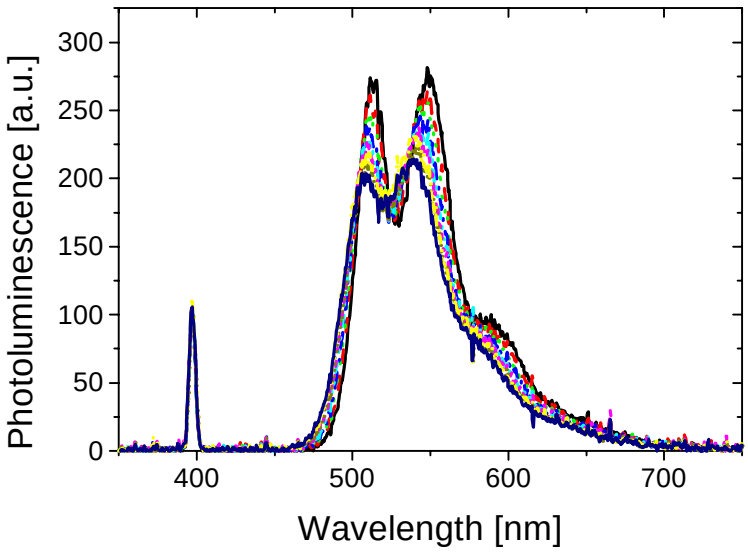

Figure 31 Photoluminescence of a PPV film at various temperatures. The PL was measured at room temperature (black), 60 °C (red), 80 °C (green), 100 °C (blue), 120 °C (cyan), 140 °C (magenta), 160 °C (yellow), 180 °C (dark yellow) and 200 °C (navy). The graph shows that the PL decreases in intensity and blue-shifts monotonically with increasing T while the scattered intensity from the excitation beam is constant.

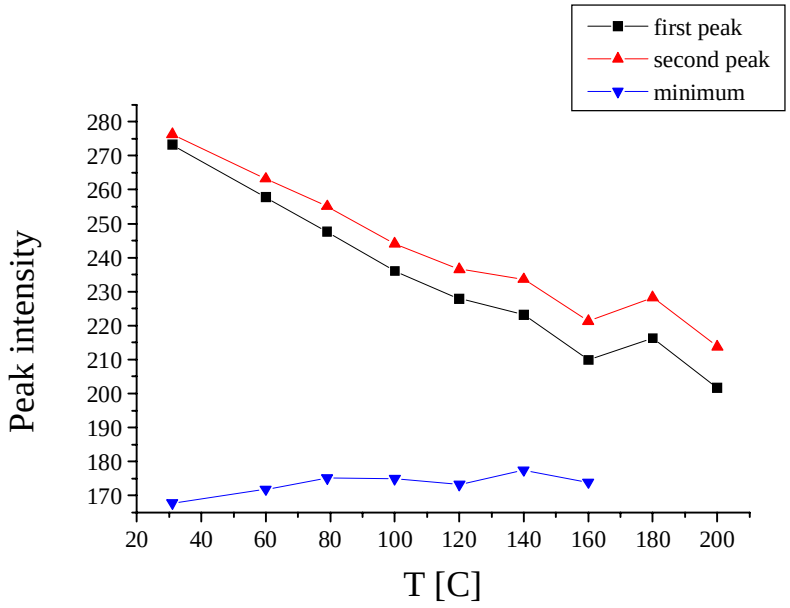

Figure 32 Peak intensity of PPV photoluminescence versus temperature. The first (squares) and second (triangles) peaks decrease in a linear fashion with increasing temperature.

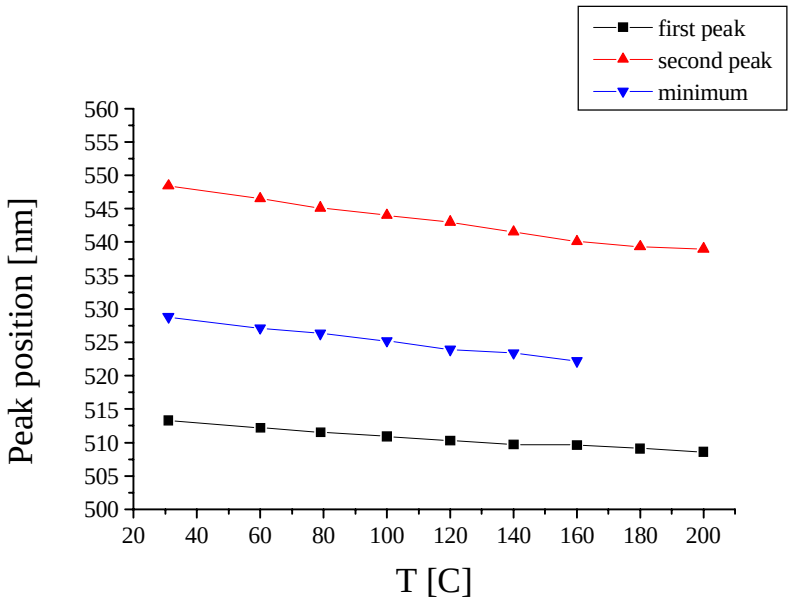

Figure 33 Peak position of PPV photoluminescence versus temperature. The position of the first (squares) and second (triangles) peaks shift to shorter wavelength with increasing temperature.

4.2 Stability at Elevated Temperatures

To examine the stability of PPV at elevated temperatures over longer time periods, a PPV film on ITO-covered glass substrate was heated to 100 ^{o}C and kept at the elevated temperature for more than an hour. The measurements in the following graphs are labeled according to the following: #1 at room temperature, #2 after T stabilized at 100 °C, #3 right after #2, #4 ~30 min after #3, #5 ~30 min after #4. Figure 35 shows the recorded spectra for measurements #1 through #5. While the PL decreases and shifts to lower wavelengths when the temperature is raised from room temperature to 100 ^{o}C, the PL does not change further when T is kept constant at 100 ^{o}C for one hour.

A close look at the peak intensity and peak position shows that the spectra at elevated temperature are indeed identical. Figure 36 plots the peak intensity of the first and second peaks in the PL spectrum for the 5 measurements. The intensity of both peaks first drops when the temperature is raised from room temperature to 100 ^{o}C but then stays constant for more than an hour at the elevated T. Also, the peak position first shifts to a shorter wavelength when T is raised to 100 ^{o}C but then does not change during a time of more than an hour (Figure 37). Again the PL spectrum shows a full recovery of the original PL indicating that there is no degradation due to oxidation or decomposition.

Similar observations of PL reduction and shifting is observed for MEH-PPV films but has not been studied to the same extent as it has been for the PPV devices. In the following interdiffusion studies, the soluble derivative MEH-PPV and a soluble polythiophene derivative (P3OT) are used. The solubility of these polymers makes the device production much easier since a thermal conversion is not needed saving a significant amount of time.

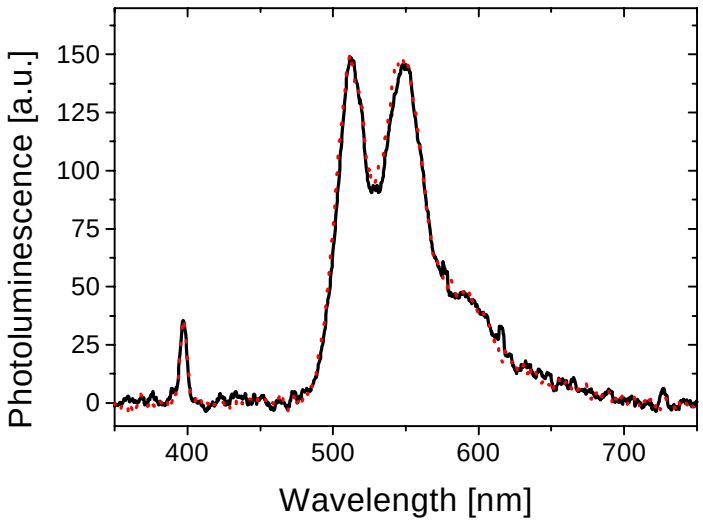

Figure 34 Photoluminescence of PPV before and after heating. The spectra shown were taken before (solid, black) and after (red, dotted) heating the film to 180 ^{o}C. The PL fully recovers to the original spectrum.

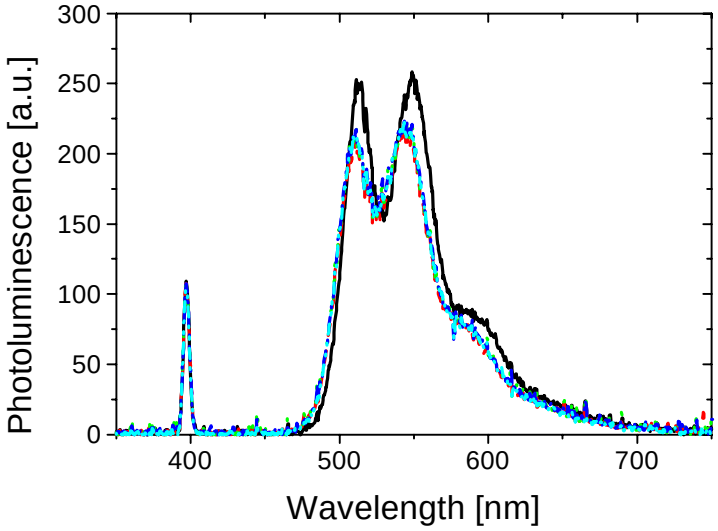

Figure 35 Photoluminescence spectra of PPV at constant elevated temperature. The graph shows the following measurements: #1 at room temperature (black), #2 after T stabilized at 100 °C (red), #3 right after #2 (green), #4 ~30 min after #3 (blue), #5 ~30 min after #4 (cyan). The PL spectrum decreases and shifts to lower wavelengths when T increases but doesn't change further when T is constant at elevated T.

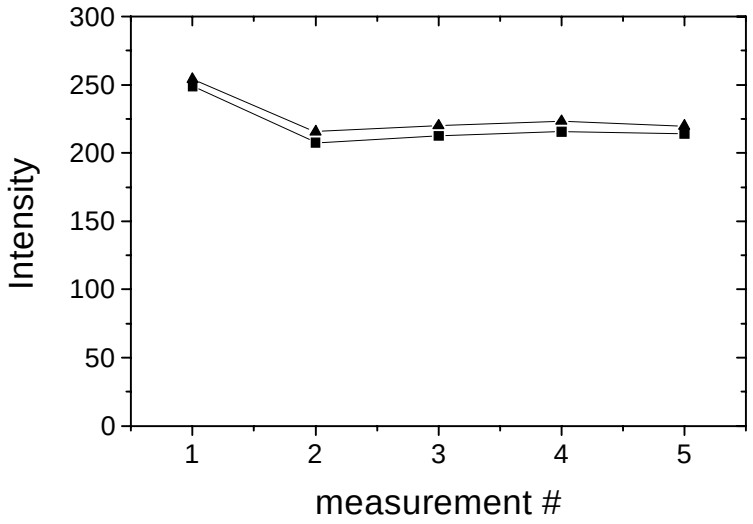

Figure 36 Intensity of the peaks in the PL spectrum. Squares show the first peak and triangles the second. The measurements are labeled as in the previous Figure. The PL intensity drops when T increases from room temperature to 100 ^{o}C and stays constant at 100 ^{o}C over more than an hour.

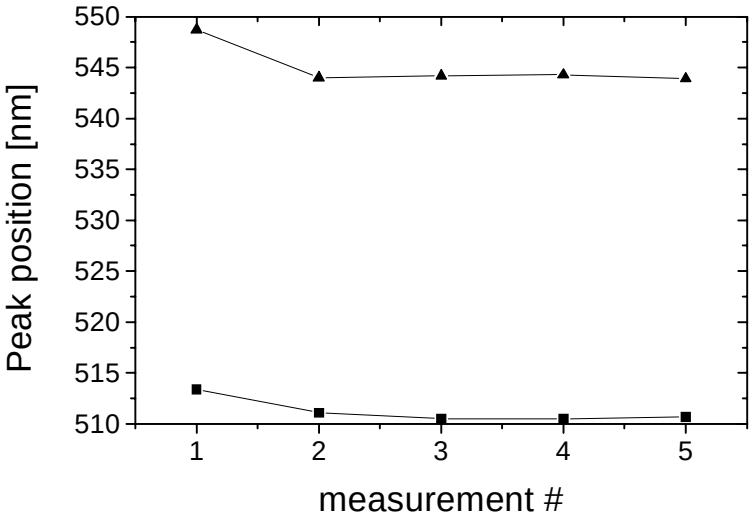

Figure 37 Peak position of the peaks in the PL spectrum. Squares show the first peak and triangles the second. The measurements are labeled as in the previous two figures. The peaks shift to lower wavelengths when the temperature increases and stay at the same position for constant elevated T.

Chapter 5

MEH-PPV/C_{60} devices

The first donor-acceptor system that we studied was MEH-PPV as the electron donor material and C_{60} as the acceptor. The main reason for choosing these materials was the high solubility of MEH-PPV in organic solvents like chlorobenzene, chloroform, toluene etc.. The solubility made it possible to spin-cast MEH-PPV from solution without thermal conversion (which is needed for unsubstituted PPV) and therefore made device production easy. In addition, both materials have been studied intensively together as donor and acceptor in heterojunction and bulk-heterojunction devices. Therefore, a solid foundation of data was available to check the devices produced for this study with already existing devices to assure reproducibility.

5.1 Unheated Devices

In a first step, a series of unheated single and bilayer devices was produced. Cleaned ITO slides were covered with a 50 nm PEDOT film that was spin-cast from an aqueous solution. After a short air-drying (typically between 5 and 10 minutes), a 90 nm MEH-PPV layer was spin-cast from a 1 % wt/vol chlorobenzene solution. These films were then transferred into the vacuum system and annealed for 1 hour at 150 ^{o}C (pressure below 4x10^{-6} Torr) to remove water and solvent. After cooling down, a 200 nm Al layer was evaporated for the single layer devices without breaking the vacuum. For the bilayer devices, a 100 nm C_{60} layer was sublimed. After the C_{60} sublimation, the vacuum had to be broken to remove the C_{60} source and add the Al source to the vacuum chamber. The 200 nm Al layer was evaporated after re-establishing the vacuum.

5.1.1 Single Layer Devices

The optical density of the ITO-PEDOT substrate and the MEH-PPV layer on top of this substrate is shown in Figure 38. The substrate shows low featureless absorption for wavelengths above 400 nm but does not transmit any light below 300 nm. The MEH-PPV layer has an absorption peak at 490 nm and an onset at 590 nm.

The photoresponsivity data of this device is shown in Figure 39. The graph displays the data obtained for all 8 devices on a single slide showing the good reproducibility between devices on the same film. The device corresponding to the diamond symbols that shows a lower photoresponsivity is actually a device that is located at the edge of the substrate. This shows that the spin-casting technique usually gives homogeneous films, but at the edge of the slide there can be some inhomogeneity in thickness. Very similar results are also obtained for devices produced on additional substrates from same concentration solutions under the same spin-casting conditions.

The shape of the photoresponsivity data shows a peak in photocurrent at a wavelength of 540 nm. This is not at the peak absorption, which is at 490 nm. This mismatch between absorption and photocurrent can be explained by the filter effect of the bulk. Since MEH-PPV is a good hole transporting material, but does not transport

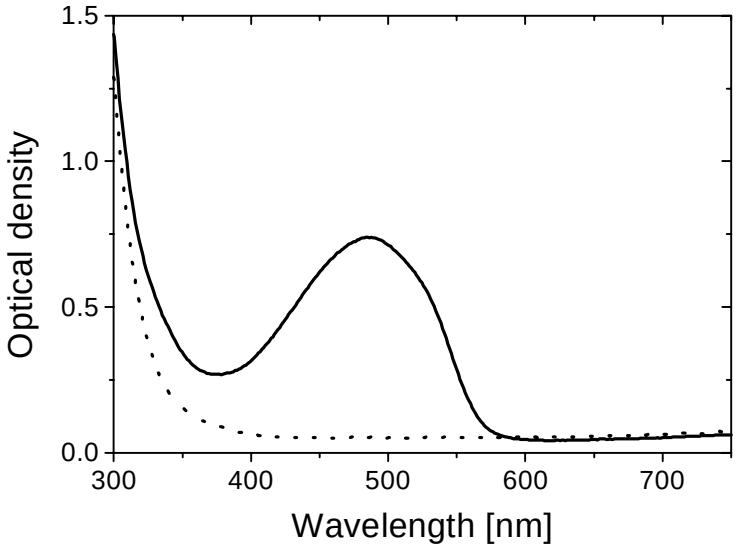

Figure 38 Optical density of a MEH-PPV single layer device. The dotted line shows the absorption of the ITO/PEDOT-coated glass substrate and the solid line shows the absorption after spin-casting an additional layer of 90 nm MEH-PPV.

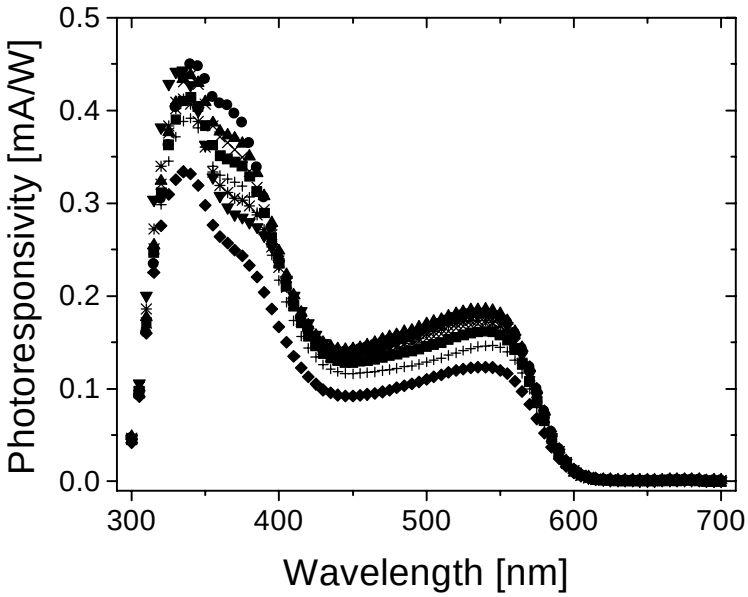

Figure 39 Photoresponsivity spectrum of 8 MEH-PPV single layer devices on one substrate. The fact that the spectra match each other shows that good reproducibility is obtained from device to device on the same film. The lowest PR spectrum (diamonds) is from a device at the edge of the slide.

electrons well, only electrons that are created by exciton dissociation close to the Al electrode will be extracted out of the device. Photons therefore must travel through the entire MEH-PPV bulk before being absorbed close to the Al electrode and creating an exciton. Thus, fewer photons with energies that are strongly absorbed will reach the desired region which can be seen in the form of lower photocurrents being extracted. The MEH-PPV bulk acts as an optical filter reducing the transmitted light for certain wavelengths.

The I-V characteristic of the single layer devices in the dark and under illumination is shown in Figure 40. The semi-log scale makes it easy to see the rectification between reverse and forward bias. Also, the V_{OC} under illumination is easily seen. The V_{OC} of single layer devices is 0.9 V at monochromatic illumination at 470 nm with an intensity of 3.8 mW/cm^2. The rectification of the devices at ±1.5 V is 2 orders of magnitude in the dark and one under illumination. The rectification gives information about the diode behavior of the device. Low rectification usually results from low shunt resistance and therefore leads to low fill factors. Figure 41 shows a linear plot of the I-V curve. The inset just shows the I-V characteristics in the 4th quadrant. This representation gives information about the fill factor of the solar cell and therefore gives some essential information about the efficiency of the cell. The single layer devices show a very low *FF* that is below 0.25. Fill factors below 0.25 typically indicate that there is a blocking contact at one of the electrodes inhibiting charge extraction out of the device. In the ECD this effect is accounted for by the second diode D_2 (Section 2.2.1).

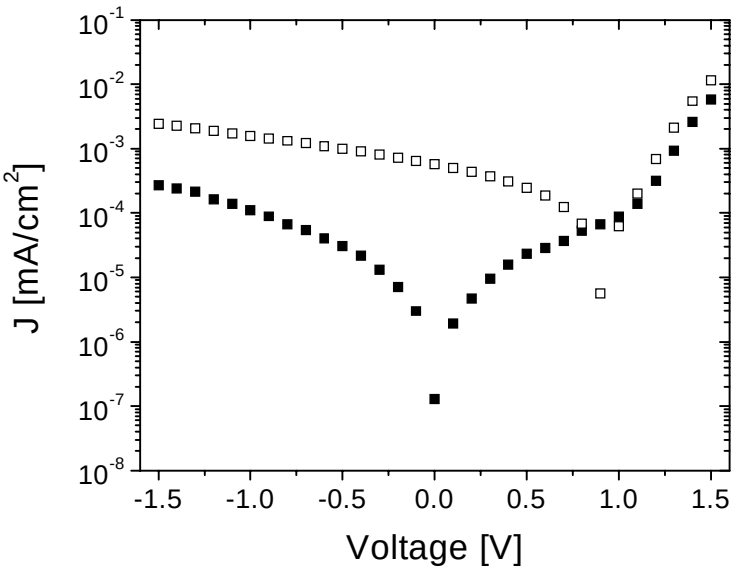

Figure 40 I-V characteristic of a MEH-PPV single layer device on a semi-log scale. The device shows rectification of 2 orders of magnitude in the dark and 1 order of magnitude under illumination (470 nm, 3.8 mW/cm^2)

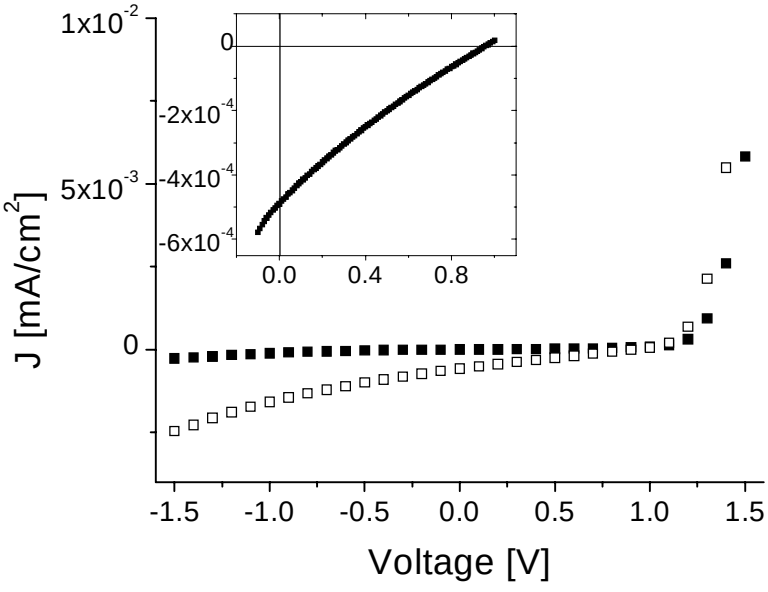

Figure 41 I-V curve of a MEH-PPV single layer device in the dark (solid) and under illumination (open) on a linear scale. The inset shows the I-V characteristic of the 4th quadrant, which is used to calculate the fill factor of the device.

5.1.2 Bilayer Devices

The optical density of an MEH-PPV/C_{60} bilayer device is shown in Figure 42. The absorption of the bilayer is a superposition of the two single layers. This shows that there is no ground state interaction between the donor and the acceptor.

Figure 43 shows the photoresponsivity of the bilayer device. The *PR* values are about an order of magnitude larger than those for single layer MEH-PPV devices. A sharp rise in photocurrent for wavelengths below the absorption edge is observed with a peak at 560 nm. The photocurrent then drops dramatically in regions of strong absorption and increases again below 400 nm. The drop in photocurrents below 350 nm is due to the absorption of the substrate preventing photons to enter the active layer. Overall the *PR* has increased by an order magnitude throughout the spectrum by introducing the C_{60} layer on top of the MEH-PPV.

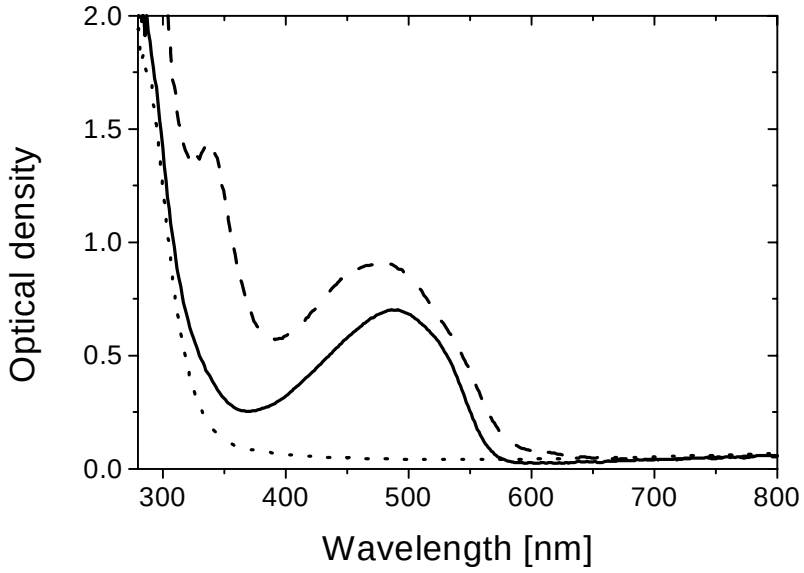

Figure 42 Optical density of a MEH-PPV/C_{60} bilayer device. The dotted line shows the absorption of the ITO/PEDOT-coated glass substrate, the solid line shows the absorption after spin-casting an additional layer of 90 nm MEH-PPV, and the dashed line shows the absorption after subliming an additional layer of 100 nm C_{60}. The absorption of the bilayer is a superposition of the absorption of the two single layers.

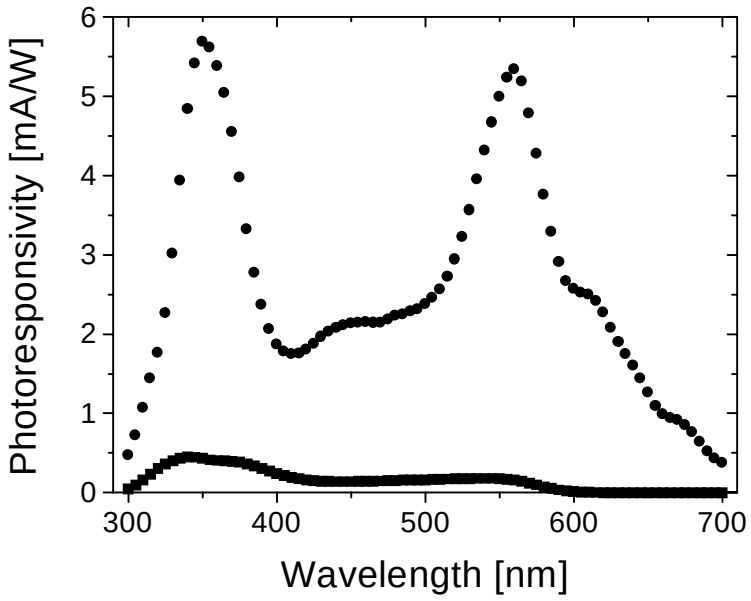

Figure 43 Photoresponsivity of an unheated bilayer of MEH-PPV/C_{60} (circles). The PR spectrum shows a peak at 560 nm and low currents at 490 nm (absorption peak). For comparison, an MEH-PPV single layer device is also shown (squares).

The shape of the photoresponsivity spectrum can again be explained by a filter effect of the MEH-PPV bulk. This time, though, it works somewhat differently than in the case of a single layer device. The overall increase in *PR* indicates that the charge separation has improved in the bilayer device. Because of the limited charge transfer range of the excitons, this efficient charge separation is limited to a very small region at the interface between MEH-PPV and C_{60}, whereas in the rest of the MEH-PPV bulk, the excitons created by photon absorption will not be dissociated and recombine instead. The number of photons reaching the donor-acceptor interface with energies that are strongly absorbed by the MEH-PPV bulk is lower than the number of photons that are not strongly absorbed. Therefore less excitons are created at the interface by photons that get strongly absorbed in the bulk. Again, the MEH-PPV bulk acts as an optical filter as observed in the *PR* spectrum. The mismatch between the spectral shape of the absorption and the *PR* of devices can be used as an indicator for the quality of the bulk-heterojunction of a device. In a bulk-heterojunction device, the shape of the photocurrent spectrum will follow the absorption spectrum.

The I-V characteristic of the bilayer devices is shown in Figure 44. The device has three orders of magnitude rectification in the dark and two orders of magnitude under illumination. This is an improvement compared to the single layer devices. On the other hand, the V_{OC} drops down to 0.4 V upon adding a layer of C_{60}. The linear plot of the I-V characteristics for the bilayer device is shown in Figure 45. The inset shows that the fill factor improves significantly upon adding the C_{60} layer. *FF* is calculated to be 0.4 for the MEH-PPV/C_{60} bilayer devices.

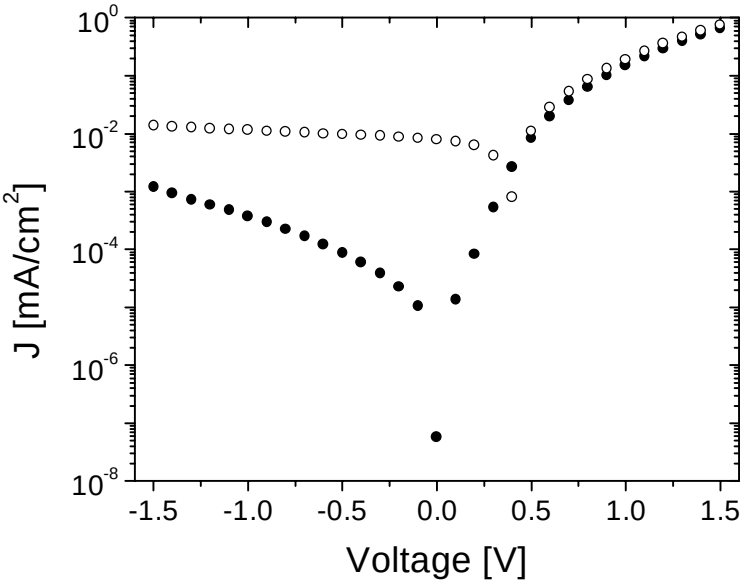

Figure 44 I-V characteristic of a MEH-PPV/C_{60} bilayer device on a semi-log scale. The device shows rectification of 3 orders of magnitude in the dark (solid) and 2 order of magnitude under illumination (open) at 470 nm, 3.8 mW/cm^2.

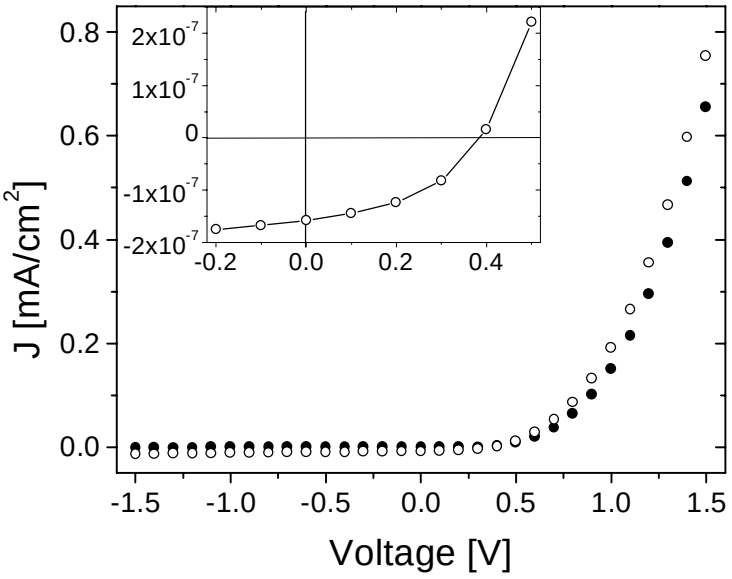

Figure 45 I-V characteristic of a MEH-PPV/C_{60} bilayer device on a linear scale. The inset shows the I-V characteristic of the device in the 4th quadrant. The V_{OC} is 0.4 V and the *FF* is calculated to be 0.4.

5.1.3 Photoluminescence of Unheated Devices

The photoluminescence of the unheated single and bilayer devices was measured in the setup described in Section 3.1.3. The devices were illuminated through the glass substrate at an excitation wavelength of 470 nm (3.8 mW/cm^2). This way the excitation beam was not subject to absorption in the C_{60} layer before reaching the MEH-PPV.

The obtained photoluminescence spectra are shown in Figure 46. The PL intensity of the single MEH-PPV layer is found to be about half of the intensity of the MEH-PPV/C_{60} bilayer. This observation is counterintuitive. The PL signal of the MEH-PPV/C_{60} bilayer was expected to be slightly smaller than the MEH-PPV single layer because the PL should be quenched at the donor/acceptor interface due to exciton dissociation. Since the interface makes up only a small fraction of the total MEH-PPV bulk, the PL is not expected to drop dramatically.

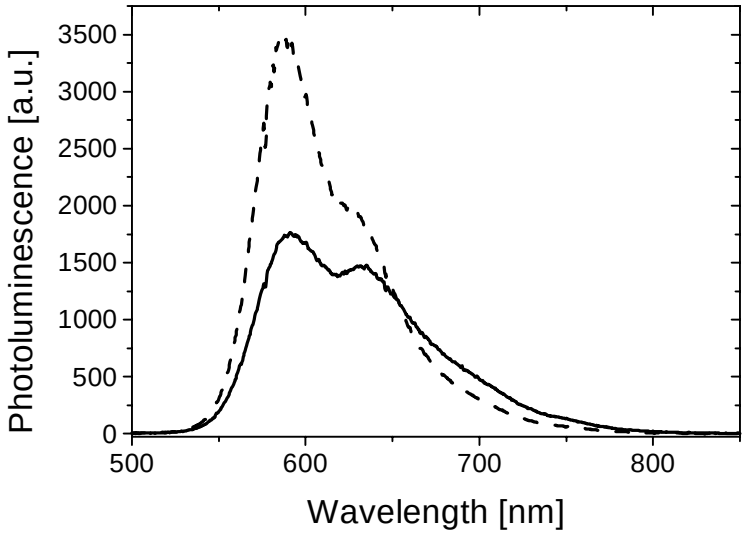

Figure 46 Photoluminescence of an MEH-PPV single layer and an MEH-PPV/C_{60} bilayer. The single layer (solid) and the bilayer (dashed) both have the same MEH-PPV thickness.

To explain the strong PL signal from the bilayer, the reflection of the excitation beam at the different interfaces of the devices was studied. The reflectivity for light at normal incidence was calculated according to

$$R = \frac{(n_2 - n_1)^2 + (k_2 - k_1)^2}{(n_2 + n_1)^2 + (k_2 + k_1)^2} \qquad 5.1$$

The real and imaginary part (n and k) of the refractive index of the device materials are listed in Table 2. The reflectivity of the interfaces resulting from the refractive index are listed in Table 3. The results shows that by introducing a layer of C_{60}, 3 % of the excitation beam that is not absorbed is reflected at the MEH-PPV/C_{60} interface. In addition to that, the reflectivity of the C_{60}/air interface is more than double that of the MEH-PPV/air interface (14 % vs 6 %). On the other hand the excitation light beam is subject to absorption in the C_{60} layer. Clearly, the slight increase in intensity of the reflected excitation beam can not account for the doubling of the PL intensity.
In addition, the reflectivity of the interfaces for a wavelength of 600 nm was calculated. The peak of the PL spectrum is close to this wavelength. Table 3 shows that

Table 2 Real and imaginary part (*n* and *k*) of the refractive index for organic materials at different wavelengths.

	n (470 nm)	*n* (600 nm)	*k* (470 nm)	*k* (600 nm)
air	1	1	0	0
C_{60}	2.2	2	0.2	0
MEH-PPV	1.6	2.0	0.3	0.6

the reflectivity of the MEH-PPV/air and C_{60}/air interface are nearly the same for this wavelength and that the reflectivity of the MEH-PPV/C_{60} interface is negligible.

A full explanation for the increased intensity of PL signal upon adding a C_{60} layer cannot be found. Even though not very satisfying, this observation is not essential for the presented work. The important comparison for this study is the development of the PL intensity of the bilayer device upon heat-treatment. This will be presented in Section 5.2.2.

5.2 Interdiffused Devices

To induce interdiffusion between MEH-PPV and C_{60}, the devices were heated in an inert environment. Heat cycles at temperatures below and above the glass transition temperature of the MEH-PPV (T_g = 230 ^{o}C) were used to examine the interdiffusion. The interdiffusion heating was done on devices before Al deposition. Before doing the

Table 3 Reflectivity R at the interfaces of the MEH-PPV/C_{60} device for normal incidence.

	R (470 nm) [%]	R (600 nm) [%]
MEH-PPV/air	6	13
C_{60}/air	14	11
MEH-PPV/C_{60}	3	2

interdiffusion heating on bilayer devices, single layer devices were heated to see if there were any changes in the single layer device due to heating. Arias *et al.* reported interdiffusion of polystyrene sulfonic acid (PSS) (a component of PEDOT) into PPV during thermal conversion [61]. This doping of PPV by the PSS eliminated the filter effect of the devices due to strong absorption of the PPV. Since thermal conversion is done at temperatures ~220 ^{o}C for 10 hours versus the interdiffusion heating in this study being done for 5 minutes, this interdiffusion is not expected to occur but has to be tested to exclude this effect.

5.2.1 Single Layer Devices

A series of four MEH-PPV single layer devices on a PEDOT-ITO substrate was prepared to study the influence of the heat-treatment on the polymer. Two were heated for 5 minutes at 250 ^{o}C before Al deposition while the other two were not heat-treated. The photoresponsivity data of the four films is shown in Figure 47. All four devices show very similar photoresponsivity above 400 nm. Below 400 nm, the heated devices have lower photocurrents. All devices show a filter effect due to strong absorption of the MEH-PPV bulk. The photocurrent peak of the unheated devices at 540 nm shifts slightly to 535 nm but not substantially closer to the absorption maximum at 490 nm. Therefore, no significant reduction of the filter effect due to PSS doping of the MEH-PPV film is observed.

The optical density of the heated devices was measured before and after the heating. Figure 48 shows that the optical density decreases slightly around the absorption peak after the heat-treatment at 250 ^{o}C. This might be due to oxidation of the polymer since the samples are exposed to air during the spin casting and not all oxygen traces can be removed prior to the heat treatment. Another possibility is that there is a small decomposition of the polymer at this high temperature. Heating the polymer at 150 ^{o}C (below T_g) has no influence on the optical density.

From these observations, it is concluded that an interdiffusion of PEDOT into the MEH-PPV bulk does not occur and the changes to the polymer due to the heat-treatment are relatively minor.

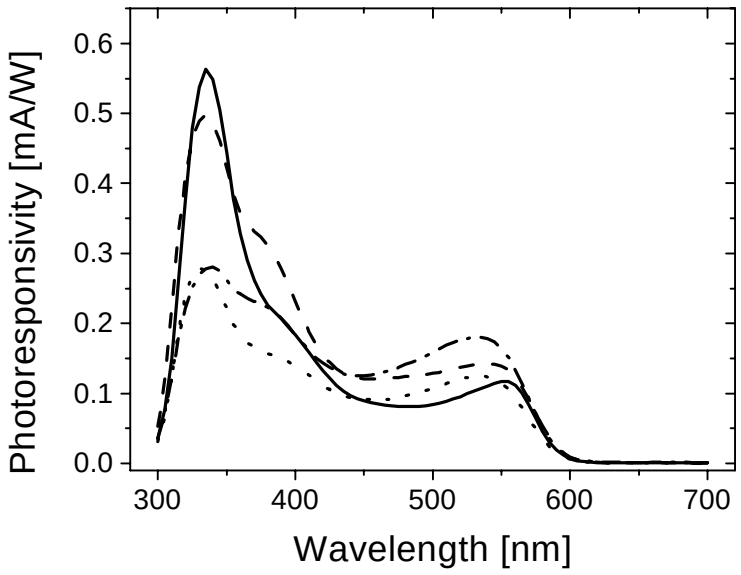

Figure 47 Photoresponsivity spectra for unheated and heated MEH-PPV single layer devices. Two MEH-PPV films were prepared without heating (solid and dashed lines) and two were heated at 250 ^{o}C for 5 minutes (dotted and dash-dotted lines). The heated devices both have smaller photocurrents below 400 nm than the unheated devices. The film represented by the solid line has a thickness of 140 nm, all other films have a thickness of approximately 110 nm.

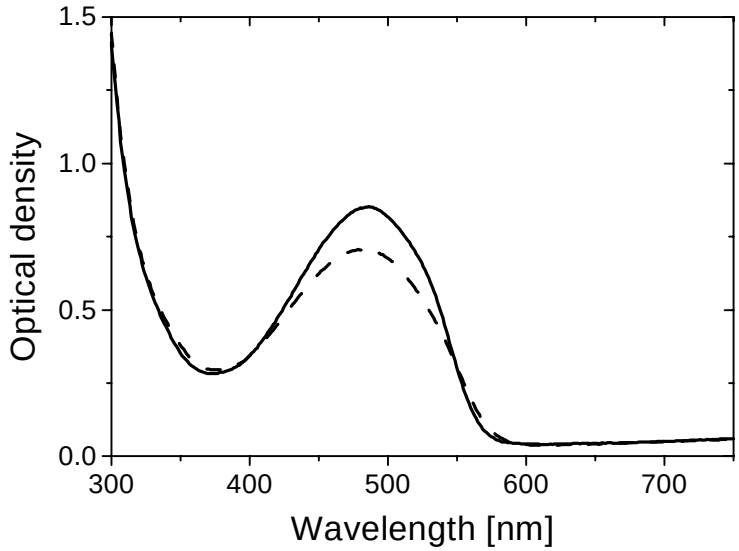

Figure 48 Optical density of a MEH-PPV single layer device before (solid) and after (dashed) heating at 250 ^{o}C. The device shows a reduction in OD around the peak absorption.

5.2.2 Photoluminescence Quenching due to Heating

In the next step, MEH-PPV/C_{60} bilayer devices were prepared. Devices presented here have a 100 nm C_{60} layer deposited on a 90 nm MEH-PPV layer. The bilayer devices were heated at temperatures below (150 ^{o}C) and above (250 ^{o}C) T_g. Heat cycles include heating up to the set temperature, staying at that temperature for five minutes, and cooling back down to room temperature, all done in an inert environment to prevent oxidation of the samples.

The photoluminescence of the samples was recorded in the same way as for the unheated devices (Section 5.1.3). Figure 49 shows the PL spectra obtained for the heated devices. For comparison the PL spectrum of an unheated bilayer is shown. While the unheated bilayer shows strong PL, the PL is quenched by an order of magnitude for devices heated below and above T_g.

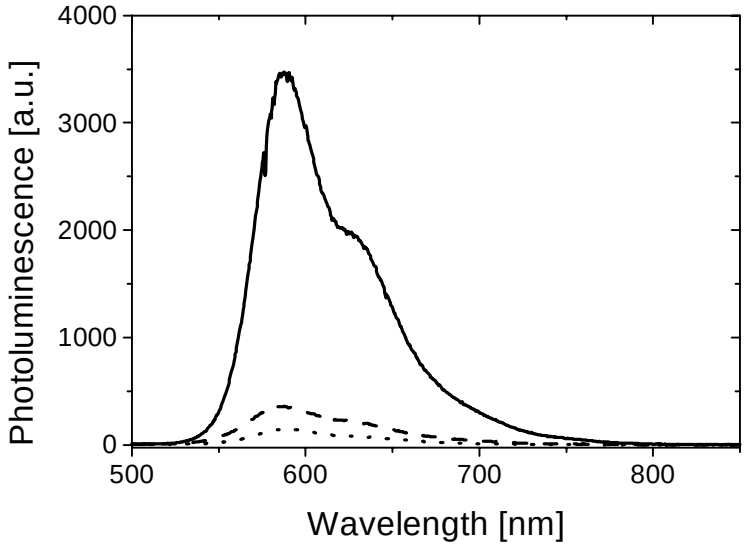

Figure 49 Photoluminescence quenching in interdiffused devices. The PL of the unheated bilayer (solid) is quenched by an order of magnitude upon heating at 150 ^{o}C (dotted) or 250 ^{o}C (dashed) for 5 minutes.

In Section 2.1.4, it was described that PL occurs when excitons recombine radiatively and that strong PL in donor-acceptor devices is a sign of low charge separation efficiency. Thus, the quenching of PL observed after heat-treatment is an indication that more excitons are dissociated in the device and therefore that the donor-acceptor interface was improved. The data show that even at temperatures below the T_g of MEH-PPV, some C_{60} can diffuse into the polymer bulk and improve the exciton dissociation. The fact that the absorption of the bilayer does not change during the heat-treatment at 150 ^{o}C shows that the observed PL quenching is not due to oxidation of the polymer.

A closer look at Figure 49 reveals that the PL signal of the bilayer heated at 250 ^{o}C is bigger than the PL signal of the bilayer heated at 150 ^{o}C. Intuitively this does not seem to be correct because at higher temperatures stronger interdiffusion is expected therefore leading to stronger PL quenching. A look at the scattered intensity of the excitation beam shows that for the device heated at 250 ^{o}C the scattered excitation light is nearly double the intensity of that from the 150 ^{o}C device. This might indicate that the heating above T_g induces a change in morphology that leads to stronger scattering. If the

excitation beam is scattered more strongly in the film, then the volume where excitons are created is larger and therefore the PL signal is larger.

To examine whether the heating leads to a rougher film surface, atomic force microscopy (AFM) studies were performed on an unheated bilayer, a bilayer heated at 150 ^{o}C and a bilayer heated at 250 ^{o}C. While the root mean square roughness of the C_{60} surface barely increases from 1.5 nm in the unheated bilayer to 1.6 nm in the bilayer heated at 150 ^{o}C, it more than doubles to 3.2 nm in the bilayer heated at 250 ^{o}C. Even though the rougher C_{60}-air interface does not necessarily explain the stronger PL signal for films heated at 250 ^{o}C, it indicates some change in the morphology of the film.

The issue of stronger scattering will be revisited in section 5.5 where the interface between MEH-PPV and C_{60} is examined on a microscopic level with TEM studies.

5.2.3 Improved Photocurrent Behavior

After observing PL quenching for the heated bilayer device, the photorepsonsivity spectra of these bilayer devices were recorded. The results are shown in Figure 50. While the unheated bilayer shows a strong filter effect between 400 and 500 nm, the device heated at 150 ^{o}C does not show a filter effect. This shows that indeed C_{60} diffused into the MEH-PPV bulk and improves the charge separation process. However, the maximum currents have not improved significantly compared to the unheated bilayer device. Even though there is C_{60} in the MEH-PPV bulk to quench PL and to reduce the filter effect, the charge transport through the C_{60} phase out of the active layer is most likely still poor. Upon heating the bilayer at 250 ^{o}C, the photoresponsivity is improved by an order of magnitude throughout the spectrum. This seems to indicate that heating above the T_g of MEH-PPV leads to an interdiffusion of C_{60} that not only quenches the PL but also builds pathways for the separated charges to be transported through the active layer to the electrodes.

The *PR* spectrum was also used to calculate the *EQE* of the interdiffused devices. The *EQE* gives the efficiency of converting incident photons to collected electrons. Figure 51 shows that the peak *EQE* is 7 % for the device heated at 250 ^{o}C.

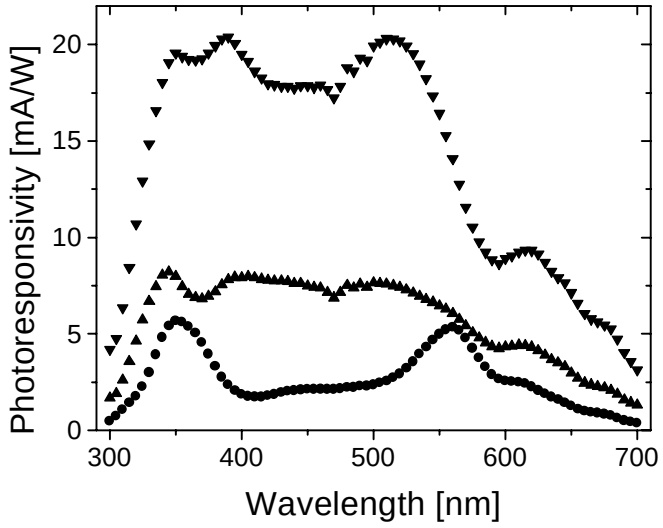

Figure 50 Photoresponsivity spectra of the interdiffused devices. The graph shows the *PR* spectrum of a device heated at 150 ^{o}C for 5 minutes (up triangles) and a device heated at 250 ^{o}C for 5 minutes (down triangles). For comparison, an unheated bilayer device is shown (circles).

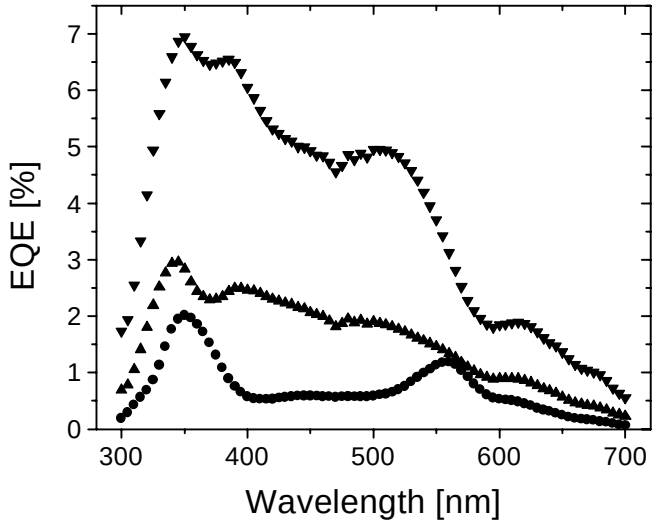

Figure 51 External quantum efficiencies of interdiffused devices. The *EQE* of the devices shown in Figure 50 was calculated from equation 2.7. The graph shows the *EQE* spectrum of a device heated at 150 ^{o}C for 5 minutes (up triangles) and a device heated at 250 ^{o}C for 5 minutes (down triangles). For comparison, an unheated bilayer device is shown (circles).

The I-V curves of the heated devices show two orders of magnitude rectification in the dark and one order of magnitude rectification under illumination (Figure 52). Compared to the unheated bilayer device (V_{OC} = 0.4 V), the open circuit voltage is improved to 0.6 V for heating below T_g (at 150 ^{o}C) and 0.5 V for heating above T_g (at 250 ^{o}C). On the other hand, the *FF* drops for heat-treated devices. It is found to be 0.24 for the devices heated at 150 ^{o}C and 0.29 for 250 ^{o}C compared to 0.4 in the unheated devices. The linear I-V characteristics are shown in Figure 53 and a closer look at the shape of the I-V curve in the 4th quadrant is plotted in Figure 54. Another observation that can be made from the linear I-V curves is the change in slope in the 3rd quadrant of the graph. Compared to the unheated bilayer device, the slope increases from 0.004 mA/(cm^{2}V) to 0.04 mA/(cm^{2}V) in the device heated at 150 ^{o}C and 0.08 mA/(cm^{2}V) in the device heated at 250 ^{o}C. This increase in slope indicates a reduction in shunt resistance R_{Sh} (see Section 2.2.4) of the device due to the heating. A reduction of R_{Sh} would also explain the smaller *FF* in the heated devices. Typically, a smaller R_{Sh} also results in a smaller V_{OC}. Instead, the devices show an increase in V_{OC}, which can be explained by a higher short circuit current I_{SC} resulting from a higher photocurrent generation in the interdiffused devices. While the increase in photocurrents and V_{OC} is advantageous for the efficiency of photovoltaic devices, the reduction of R_{Sh} and the resulting lower *FF* is an effect that is not desirable.

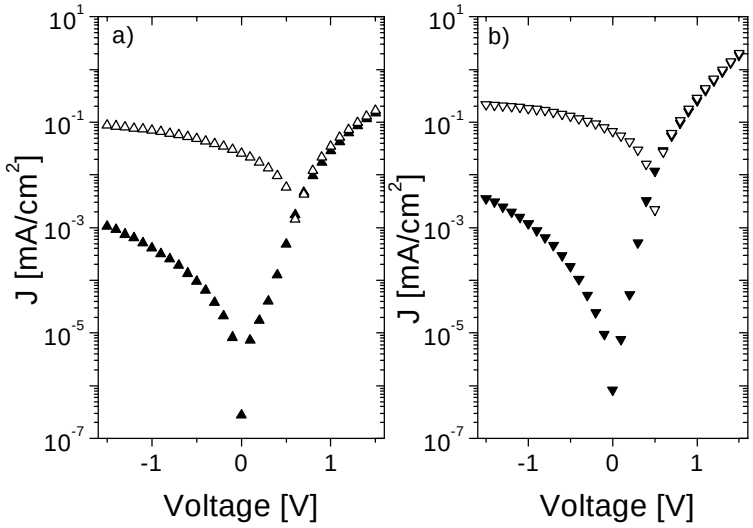

Figure 52 I-V characteristics for interdiffused devices. The devices heated at 150 ^{o}C (a) and at 250 ^{o}C (b) show an improved V_{OC} compared to the unheated bilayer. Solid symbols show the dark I-V and open symbols show illuminated I-V (470 nm, 3.8 mW/cm^2).

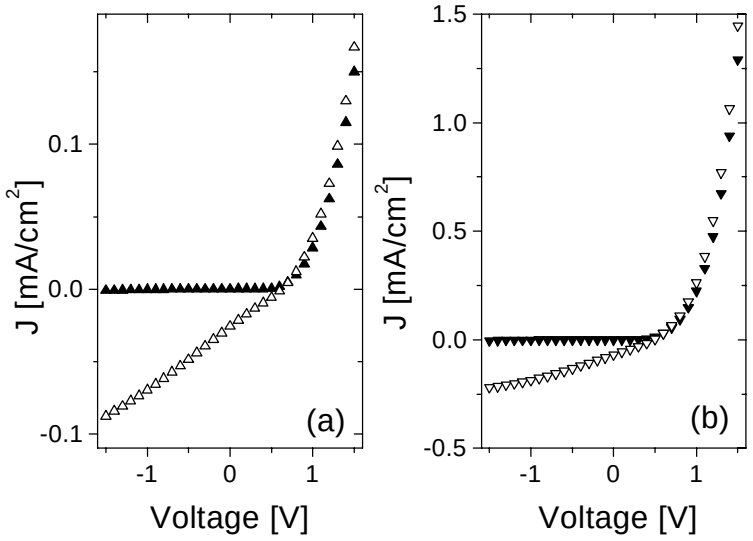

Figure 53 I-V characteristic of devices interdiffused at a) 150 ^{o}C and b) 250 ^{o}C on a linear scale.

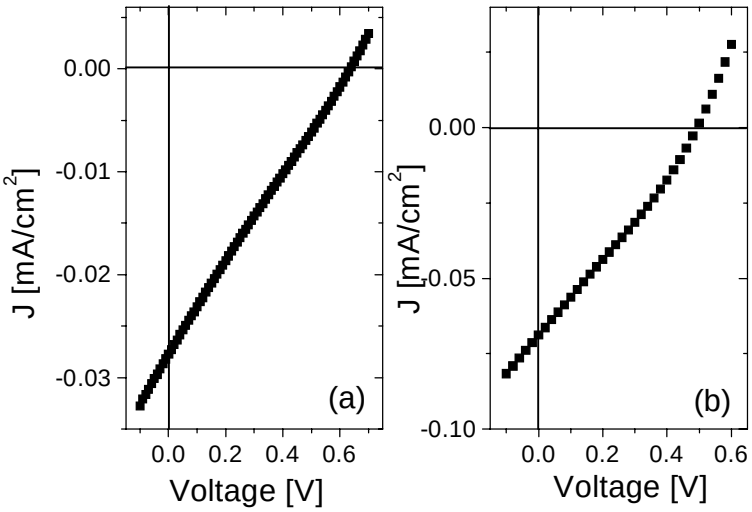

Figure 54 I-V characteristic of devices interdiffused at a) 150 ^{o}C and b) 250 ^{o}C in the 4th quadrant. *FF* is 0.24 for 150 and 0.29 for 250

5.2.4 Thermal Stress

In some devices, the heat treatment resulted in cracks in the polymer film. These cracks occurred in devices that were heated below and above the polymer T_g. While the appearance of cracks was independent of the final temperature, it did depend on the thickness of the polymer film. For polymer film thicknesses of 90 nm and below, none of the produced devices showed any cracks. Only films that were 110 nm or thicker showed cracks. An example picture of a cracked bilayer device taken with a 20x microscope is shown in Figure 55. Even though the device shows significant damage due to cracks, it is still functional. The Al deposition did not lead to dramatic shorting between the Al and ITO even though the Al deposition was done after the heating and therefore in the presence of cracks. Since the cracks were observed both in single polymer layers and polymer fullerene bilayers, it is suspected that the cracks occur exclusively in the polymer phase. In that case, the C_{60} layer is not cracked and prevents shorting between Al and ITO.

To further investigate the origin of the cracking, studies were performed with a microscope hot stage. In this setup, the samples could be observed with the microscope

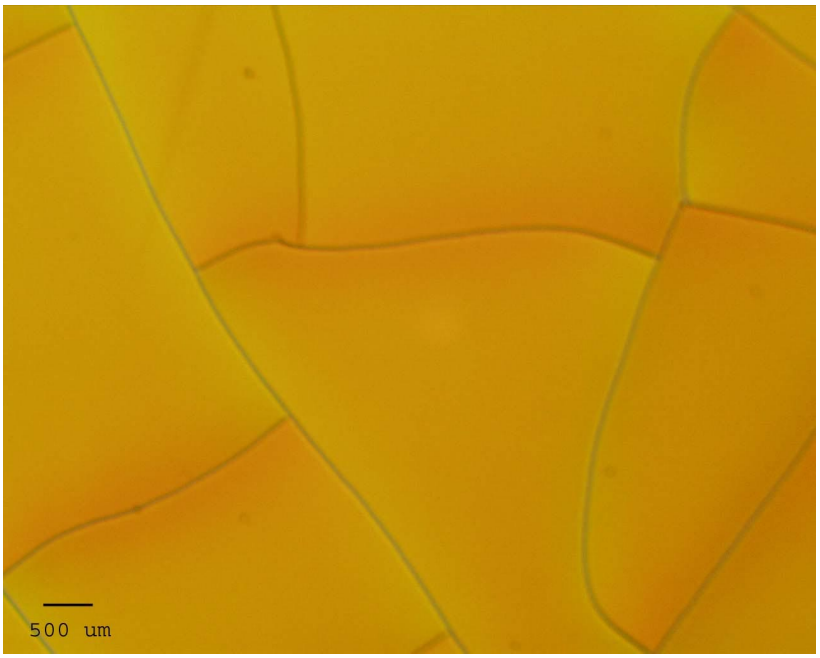

Figure 55 Cracked MEH-PPV/C_{60} bilayer film. The picture was taken under a microscope and shows the cracks that formed during the interdiffusion heating. Film thicknesses are 110 nm MEH-PPV and 100 nm C_{60}.

during the whole heating and cooling process. The hot stage had a temperature controller with a ramp function enabling various constant heat rates. Heating was done in a nitrogen atmosphere.

In these studies, the polymer films were heated to 250 ^{o}C to see when cracking occurs. It was observed that cracking did not occur every time. It was only observed for high heating rates (>30 ^{o}C/min) and then only when the heating rate suddenly changed when the heater reached the setpoint of 250 ^{o}C. The cracks seemed to originate from defects in the film. A picture of a film before heating and during crack-formation at elevated temperature is shown in Figure 56. The picture clearly shows cracks starting from impurities in the film. The color change in the polymer is due to the change in luminescence of the polymer at elevated temperatures. It is fully reversible when the sample is cooled down to room temperature. A similar behavior was also observed in PPV and is described in more detail in Chapter 4.

It is therefore concluded that the cracking occurs due to thermal stress in the polymer at large heating rates. In the setup used for the interdiffusion, the heating rates can exceed 40 ^{o}C/min because the temperature controller used has no ramp function. This

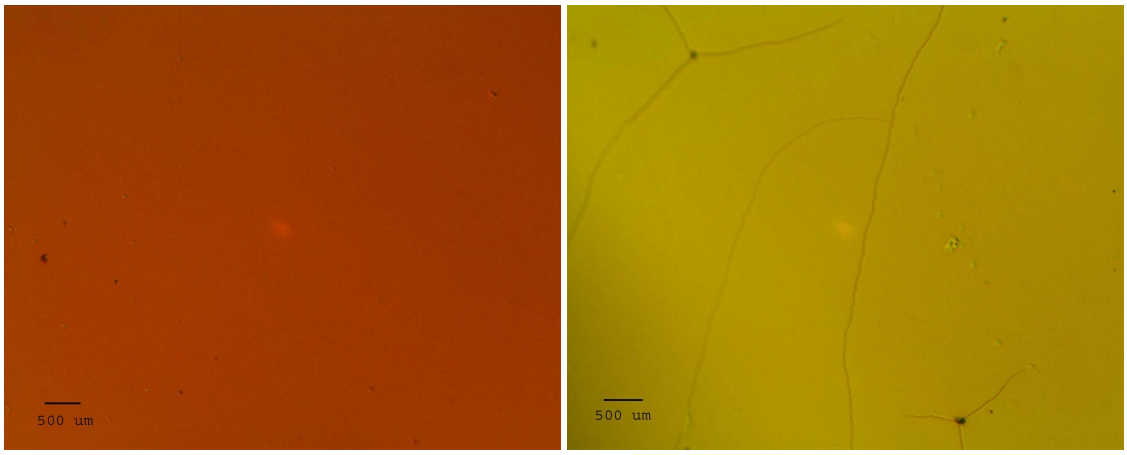

Figure 56 Picture of MEH-PPV/C_{60} bilayer before and during heating. The left picture shows the film at room temperature before heating. The right picture shows the film at 250 ^{o}C when cracks start developing. Cracks seem to originate from defects in the film. The color change is due to the change in luminescence of MEH-PPV at elevated temperatures and is fully reversible.

problem was later solved by building a new hot stage with a controller that was computer-controlled allowing for programmed heating rates. Also, the thermal stress seems to be less significant in thinner polymer films, preventing cracking in films 90 nm and below.

5.3 Influence of the Polymer Layer Thickness

After successfully implementing the thermally-controlled interdiffusion concept to create a bulk-heterojunction from a bilayer system of polymer and fullerene, the dependence of the photocurrents on polymer layer thickness was studied. While an increase in layer thickness leads to more absorbed photons and therefore should increase the number of separated charges, it also increases the length of the path that charges have to travel to get to one of the extracting electrodes, resulting in an increased series resistance of the device. There should be an intermediate thickness that shows maximum photocurrents because if the active layer gets thinner then photocurrents drop because less photons get absorbed and if it gets thicker the series resistance is too large and starts limiting the photocurrent.

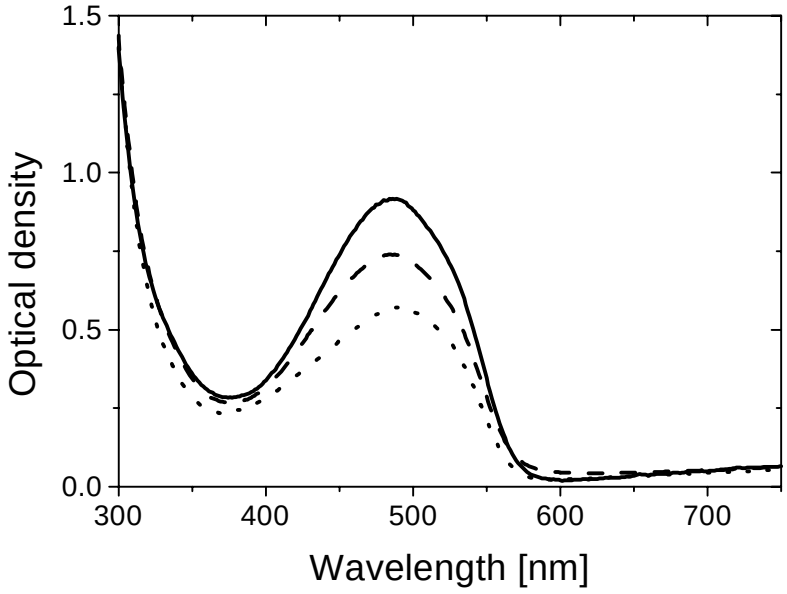

Figure 57 Optical density of MEH-PPV single layer devices with varying thickness. The graph shows the OD of MEH-PPV single layers of 110 nm (solid), 90 nm (dashed), and 70 nm (dotted) thickness.

For this study a series of devices was produced that had MEH-PPV thicknesses of 70, 90 and 110 nm. The optical density of MEH-PPV films of these thicknesses is shown in Figure 57. The C_{60} layer was 100 nm in all devices (except for the MEH-PPV single layer devices).

5.3.1 Unheated Devices

The photoresponsivity of a series of MEH-PPV single layer devices is shown in Figure 58. The photocurrents increase with decreasing film thickness. This is an effect that is expected since the series resistance increases with increasing film thickness. It was not possible to study thinner films because devices with thinner polymer layer had troubles with shorts between the Al and the ITO due to pinholes in the thin films. The position of the photocurrent peak is found to be at 540 nm for all three devices. It is

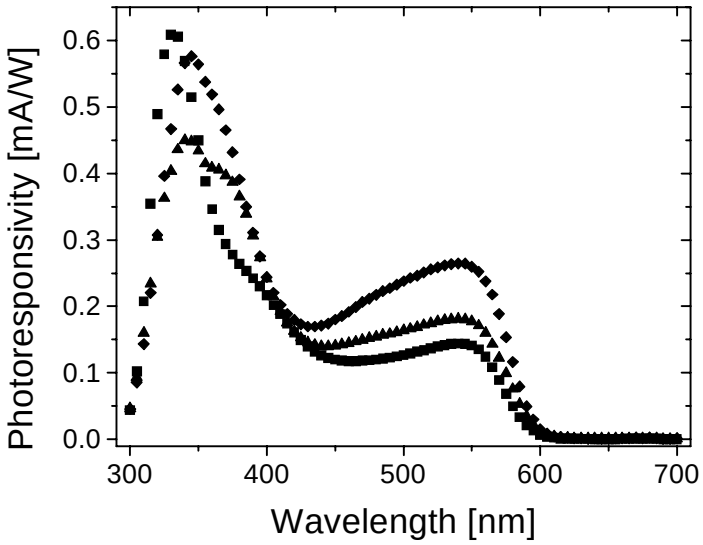

Figure 58 Photoresponsivity of MEH-PPV single layer devices with varying thicknesses. The photocurrents increase with decreasing thickness of MEH-PPV. Devices shown have thickness of 110 nm (squares), 90 nm (triangles) and 70 nm (diamonds). The peak position at 540 nm is not changed by thickness variation.

expected to shift towards the absorption onset at 590 nm for much thicker films because of the filter effect of the MEH-PPV bulk. In this thickness regime, the filter effect does not seem to vary the peak position in single layer devices significantly.

A similar trend for the photocurrents is observed for unheated bilayer devices. Again, the photocurrents increase with decreasing polymer layer thickness within the varied thickness range. Figure 59 shows the photoresponsivity for the series of MEH-PPV/C_{60} bilayer devices. In addition to the increase in photocurrent, the peak position of the photocurrents shifts towards the absorption maximum at 490 nm. The peak photocurrent moves from λ=575nm in the 110 nm device to λ=560 nm and λ=540 nm in the 90 nm and 70 nm devices, respectively. This behavior can be explained by a reduction in the filter effect of the MEH-PPV bulk with decreasing layer thickness. The overall increase in the photocurrents is due to two reasons: 1) the number of photons that can reach the polymer-fullerene interface where efficient charge separation occurs is increased in devices with thinner polymer films and 2) the distance that charges have to travel to the collecting electrodes is reduced, therefore reducing the series resistance R_S.

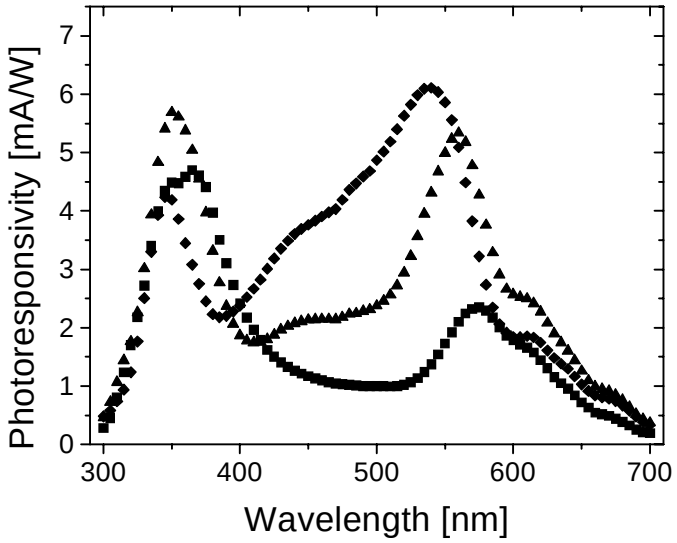

Figure 59 Photoresponsivity of MEH-PPV/C_{60} bilayer devices with varying MEH-PPV thickness. The photocurrents increase with decreasing MEH-PPV thickness. In addition, the photocurrent peak for 110 nm MEH-PPV (squares) shifts from 575 nm to 560 nm and 540 nm for 90 nm MEH-PPV (triangles) and 70 nm MEH-PPV (diamonds), respectively. The C_{60} film thickness was 100 nm for all devices.

5.3.2 Interdiffused Devices

All interdiffused devices in this series were produced in the same way as described before. Heating was done before Al deposition. The photoresponsivity spectra for the devices heated at 150 ^{o}C are shown in Figure 60 and spectra for devices heated at 250 ^{o}C are shown in Figure 61. In both series, the devices show the same trend for photocurrents as observed before, namely an increase in photocurrent with a decrease in polymer layer thickness. In addition, all devices show a reduction in filter effect with decreased thickness, which indicates interdiffusion of C_{60} into the polymer bulk.

The device with 70 nm MEH-PPV heated at 250 ^{o}C (see Figure 61) is the only device that has a photocurrent that fairly well matches the absorption spectrum. Therefore, in this device the goal of creating a bulk-heterojunction is finally fulfilled.

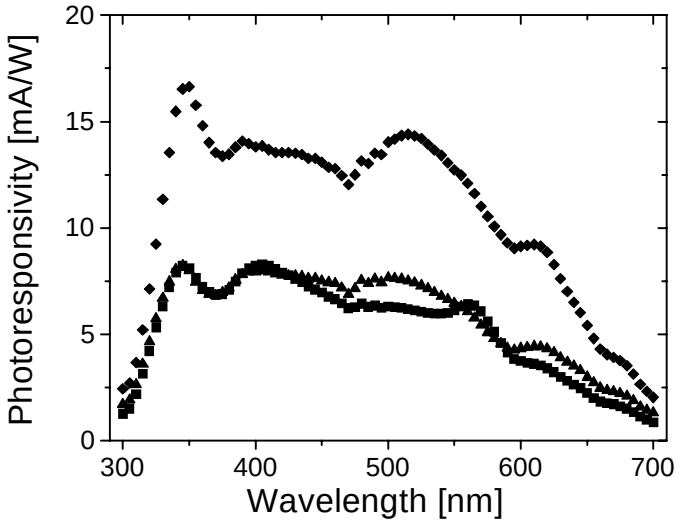

Figure 60 Photoresponsivity of MEH-PPV/C_{60} bilayer devices heated at 150 ^{o}C with varying MEH-PPV thickness. A decrease in MEH-PPV thickness results in an increase of photocurrents. In all devices, the filter effect is reduced because of interdiffusion. Devices shown have MEH-PPV thickness of 110 nm (squares), 90 nm (triangles) and 70 nm (diamonds). C_{60} thickness is 100 nm for all devices.

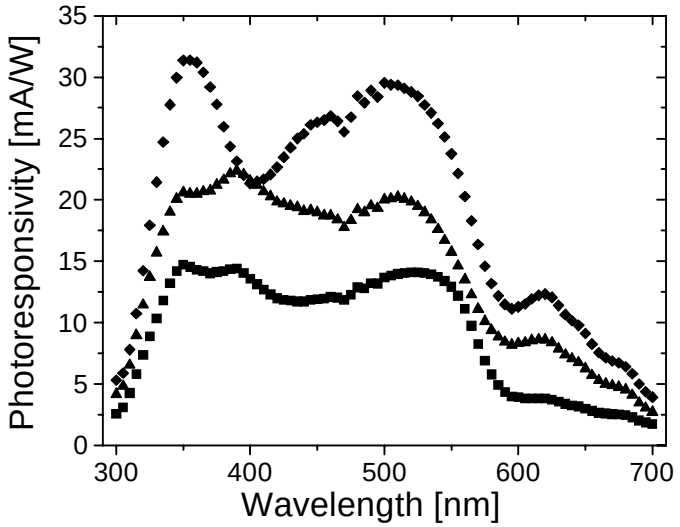

Figure 61 Photoresponsivity of MEH-PPV/C_{60} bilayer devices heated at 250 ^{o}C with varying MEH-PPV thickness. A decrease in MEH-PPV thickness results in an increase of photocurrents. Devices shown have MEH-PPV thickness of 110 nm (squares), 90 nm (triangles) and 70 nm (diamonds). C_{60} thickness is 100 nm for all devices. The photocurrent spectrum of the 70 nm device is very similar in shape to the absorption spectrum which indicates that the interdiffusion resulted in a bulk heterojunction device.

The power conversion efficiency of the 70 nm MEH-PPV device heated at 250 ^{o}C was calculated with equation 2.8 to be 0.3 % under monochromatic illumination at 470 nm (3.8 mW/cm^2).

These results show that the interdiffusion of C_{60} into the MEH-PPV bulk does not occur easily. Only in thin MEH-PPV films, where the C_{60} does not have to travel over very long distances to achieve close proximity of the acceptor to the donor material, a bulk-heterojunction is created. The reason for this will be discussed in detail in the morphology study section.

5.4 *In Situ* Interdiffusion Experiments

One goal in studying the interdiffusion of donor and acceptor materials was to observe the interdiffusion *in situ*. In all studies presented thus far, the interdiffusion heating was done before the final production step of depositing the top electrode. Because of this, the measurement of the photoresponse of the device before and after the heat treatment was not possible. In this section, results are presented of devices that were produced as bilayer devices and then taken through a heat treatment. Therefore, measurements of the photoresponsivity of the devices before and after the interdiffusion heating could be done and changes in the photocurrent spectrum of the same device were observed.

An example of an *in situ* measurement of the photocurrent is shown in Figure 62. The device was made up of 110 nm of C_{60} sublimed onto 70 nm of MEH-PPV. 470 nm light was used to illuminate the device throughout the whole heat treatment. The data shown is the uncorrected photocurrent that was measured with the picoammeter versus the elapsed time. The temperature of the hot stage is indicated for selected times.

With increasing temperature, the photocurrent of the illuminated sample starts rising. When the temperature reaches 150 ^{o}C, it is maintained for 5 minutes before the hot plate is turned off and the temperature starts decreasing. While the temperature stays constant at 150 ^{o}C, the photocurrent still increases and even after the temperature starts decreasing it still rises. The photocurrent then levels off and finally starts decreasing. The

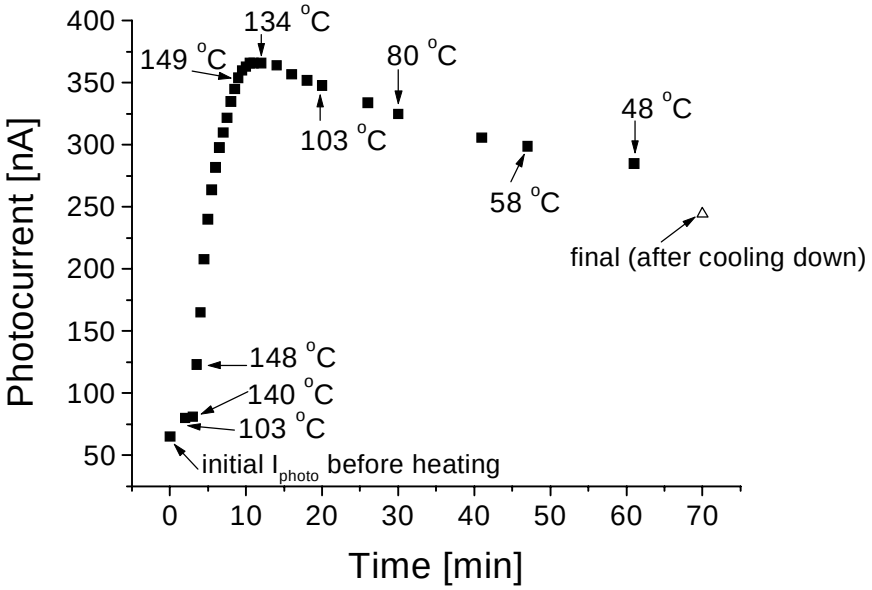

Figure 62 *In situ* photocurrent measurements. The photocurrent of a 70 nm MEH-PPV, 110 nm C_{60} device was observed during the interdiffusion heating at 150 °C (470 nm, 3.8 mW/cm^2 illumination). The squares show the photocurrent during the thermal treatment. The temperature at various times is indicated. The final photocurrent of the device (after complete cooling down to room temperature) is given by the open triangle.

final photocurrent after cooling to room temperature is 4 times larger than the initial photocurrent. Since the photocurrent decreases to some extent during cooling, not all of the increase in photocurrent during the heating is due to interdiffusion. Part of it is simply due to the elevated temperature. The reason for higher photocurrents at higher temperatures may be detrapping of charges that were trapped in shallow traps.

Figure 63 shows the photoresponsivity spectra before and after the heat treatment. The photocurrents have increased throughout the whole spectrum after the heating. To better compare the shape of the photocurrents before and after heating, the photoresponsivity spectra were normalized in Figure 64. The photocurrent spectrum after heating clearly shows a reduction in the filter effect. However, compared to devices that were heated without the Al electrode, the reduction in the filter effect is not as strong. This might be due to some constraint that the Al electrode puts on the interdiffusion of C_{60} into the MEH-PPV bulk.

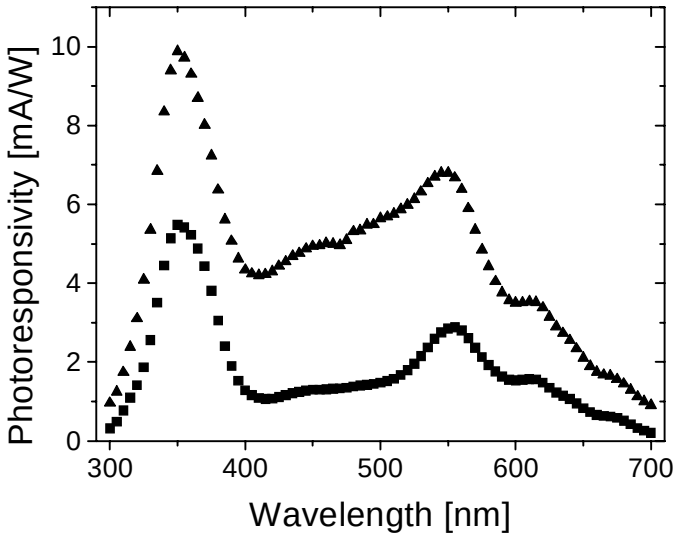

Figure 63 Photoresponsivity before and after interdiffusion. The *PR* spectrum was obtained before (squares) and after (triangles) the *in situ* interdiffusion measurement shown in Figure 62. The photocurrents were increased throughout the whole spectrum due to the heat-induced interdiffusion.

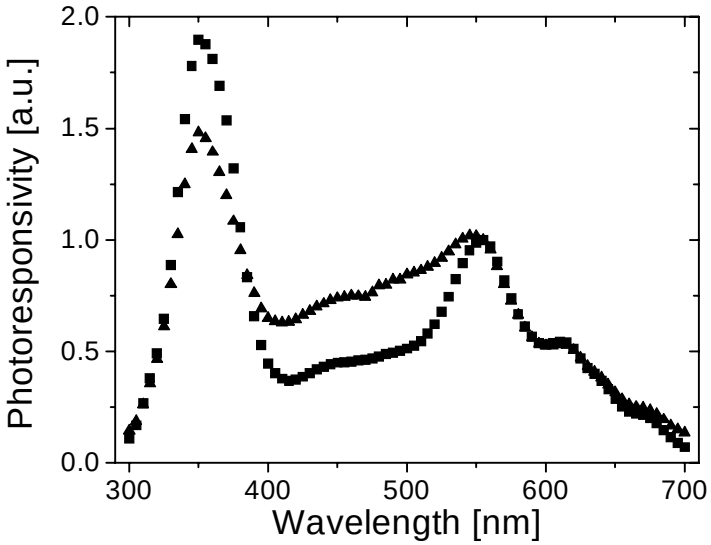

Figure 64 Normalized photoresponsivity spectra before and after interdiffusion. The photoresponsivity spectra shown in Figure 63 were normalized to the peak at 555 nm to show the difference in shape before (squares) and after (triangles) interdiffusion. The filter effect is clearly reduced by the interdiffusion.

It should be mentioned here that heating the devices for more than 5 minutes at 150 ^{o}C led to a decrease in photocurrent at the elevated temperature. The time after which this decrease started varied between devices from 5 minutes after reaching 150 ^{o}C to about 10 minutes. Also, it was not possible to monitor the interdiffusion at 250 ^{o}C. In all attempts, the devices were destroyed. The photocurrents could be monitored up to temperatures of about 200 ^{o}C. Above 200 ^{o}C, the photocurrents suddenly decreased to zero and even after cooling down did not reappear. The reason for this device failure could not be determined. It is apparent that the device failure is in the vicinity of the glass transition temperature of the polymer where the polymer chains are able to start segmental motion. There might be some kind of a delamination of the Al electrode, which ruins the contact between the C_{60} and the Al electrode.

5.5 Morphology Study

After observing the quenching of photoluminescence and the improvement of photocurrents in heat-treated devices, it was concluded that an interdiffusion of C_{60} into the MEH-PPV bulk occurred. However, these studies could not provide a microscopic picture of the new morphology of the C_{60} and MEH-PPV. The fact that only devices with a thin polymer layer resulted in a complete bulk-heterojunction after heat-treatment seems to indicate some trouble with the interdiffusion of the two materials. To get more insight on the interface between MEH-PPV and C_{60} on a microscopic level, the cross-section of devices was studied with transmission electron microscopy (TEM).

To study the morphology of the MEH-PPV/C_{60} devices, films were first prepared on microscope slides in the same fashion as devices on ITO-coated glass. The only change was that the PEDOT layer was left out in these films. To study the cross section, films were lifted off the glass by submerging the substrate with the film in deionized water. Due to the hydrophobic behavior of MEH-PPV, the films lifted off the glass and were then put on Teflon pieces. While MEH-PPV sticks to glass when it is dry it lifts off the Teflon even after drying films overnight in a nitrogen glovebox. Films were then

imbedded in an epoxy so that slices of the film revealing the cross-section could be microtomed (Section 3.1.5).

Figure 65 shows the TEM image of an unheated bilayer. From TEM studies on an MEH-PPV single layer, it was determined that MEH-PPV results in a white contrast therefore leaving the dark contrast to be the C_{60}. The image shows a distinct smooth interface between the two materials that is expected from an untreated bilayer system.

Upon heating at 150 ^{o}C, the interface between MEH-PPV and C_{60} does not seem to be influenced significantly. A TEM image of the cross-section is shown in Figure 66. Since the TEM image does not provide atomic resolution, it cannot give information about single C_{60} molecules or very small clusters of C_{60} moving into the MEH-PPV. The quenching of PL indicates that some interdiffusion occurs but the TEM image shows that no significant intermixing of the two materials takes place.

Figure 65 TEM image of an unheated MEH-PPV/C_{60} bilayer. The light phase is MEH-PPV, the dark phase is C_{60} and the gray background is from the epoxy. The picture shows a distinct and smooth interface between the two materials.

Figure 66 TEM image of an MEH-PPV/C_{60} bilayer device heated at 150 ^{o}C for 5 minutes. The interface between MEH-PPV and C_{60} is smooth and distinct. There is no indication of a large-scale interdiffusion of C_{60} into the MEH-PPV bulk.

In contrast, the bilayer heated at 250 ^{o}C shows strong changes in the morphology. In Figure 67, the TEM image of this interdiffused bilayer is shown. The distinct smooth interface between the two materials has vanished. Instead, clusters of C_{60} have moved into the MEH-PPV bulk. These clusters have diameter of up to 30 nm. The TEM image therefore shows that there isn't a continuous concentration gradient of donor and acceptor materials from one end of the film to the other. The formation of C_{60} clusters is due to the crystallizing behavior of C_{60} [62]. In addition, there is a trend of MEH-PPV and C_{60} to phase separate. It is therefore not surprising that the interdiffusion is limited in these materials.

The results of the TEM studies help explain the polymer thickness dependence of the devices. In Section 5.3.2, it was found that only for thin polymer layers is a good

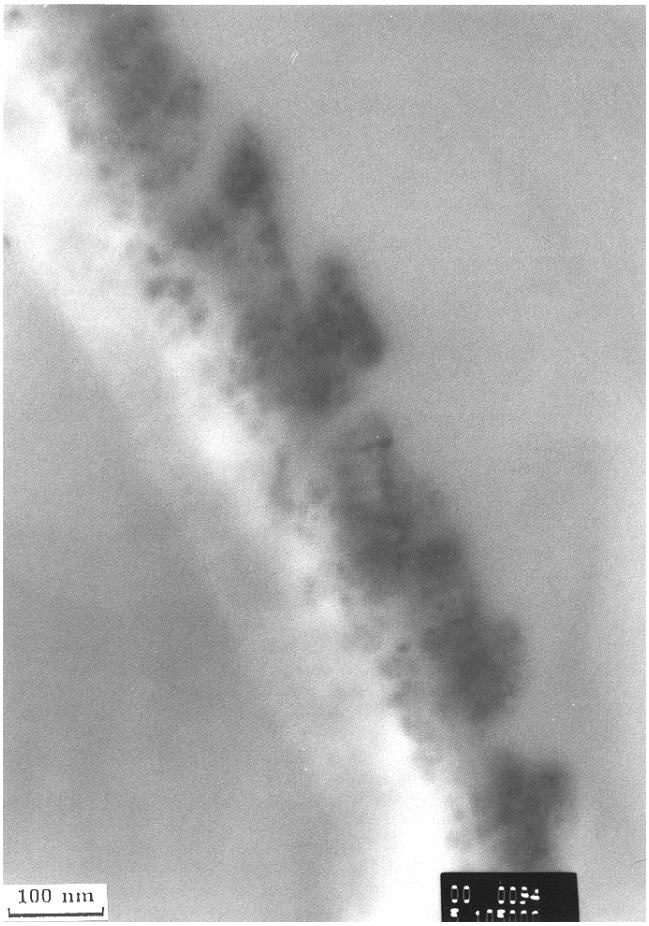

Figure 67 TEM image of an MEH-PPV/C_{60} bilayer heated at 250 ^{o}C for 5 minutes. The image shows a rough interface with clusters of C_{60} with a diameter of up to 30 nm that have moved into the MEH-PPV bulk.

bulk-heterojunction formed. Observing the size of C_{60} clusters moving into the polymer bulk and keeping in mind that the two materials tend to stay in separate phases, it is clear that the C_{60} will not move very long distances into the MEH-PPV bulk. This then limits the pathways for electrons to be transported to the Al electrode.

Another observation made earlier can now be explained with a better knowledge of the morphology of the heated films. In Section 5.2.2, it was reported that the PL signal of a bilayer heated at 250 ^{o}C was bigger than the PL signal of a bilayer heated at 150 ^{o}C. This does not make sense since for higher temperatures more interdiffusion and therefore less PL is expected. Knowledge of the film morphology now explains the phenomenon. In the bilayer heated at 150 ^{o}C, the excitation beam for the PL experiment experiences a smooth interface between MEH-PPV and C_{60}. In the bilayer heated at 250 ^{o}C, this smooth

interface does not exist any more. Instead, the excitation beam is more highly scattered by the C_{60} clusters. The scattered light then illuminates a larger area of the device leading to a stronger PL signal. An indication that this is indeed what happens is the fact that the scattered intensity of the excitation beam picked up by the detector doubles from the bilayer heated at 150 ^{o}C to the one heated at 250 ^{o}C.

These morphology studies show that the choice of donor and acceptor materials is critical for interdiffusion. Materials with low miscibility will not easily interdiffuse. A solid knowledge of the materials used and their interaction is therefore essential to successfully produce interdiffused devices. An improved donor-acceptor combination is presented in Chapter 6.

5.6 Blend Devices

A different approach to create a bulk-heterojunction between MEH-PPV and C_{60} is to blend the two materials in solution and spin coat devices from this blend. To compare the performance of the interdiffused devices to devices produced from a MEH-PPV/C_{60} blend solution, MEH-PPV and C_{60} were blended at a 1:1 weight ratio for these devices.

Devices were produced on ITO/PEDOT-coated glass substrates by spin-casting a solution made out of 20 mg of MEH-PPV and 20 mg of C_{60} dissolved in 2 ml of 1,2-dichlorobenzene. The optical density of the resulting devices is shown in Figure 68. It is comparable, but not identical to the absorption of devices made from 70 nm of MEH-PPV and 100 nm C_{60}. Therefore, the blend devices will be compared to the performance of the interdiffused devices with 70 nm polymer layer thickness.

The photoresponsivity spectrum of the blend device is shown in Figure 69. The photocurrent spectrum has the same shape as the absorption spectrum indicating that the device has a bulk-heterojunction. For comparison, Figure 69 also shows the *PR* spectrum of a 250 ^{o}C interdiffused MEH-PPV/C_{60} (70 nm / 100 nm) bilayer device. The interdiffused bilayer has essentially the same shape as the blend device and shows a slightly higher *PR* throughout the spectrum. Between 600 and 700 nm, the shape of the

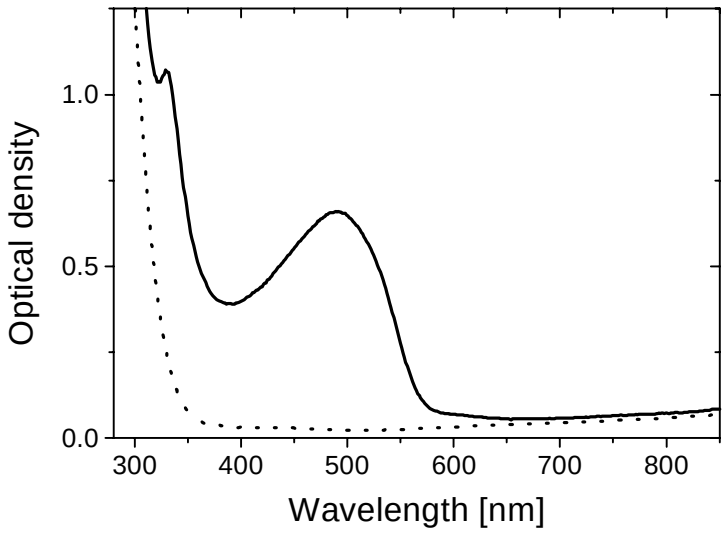

Figure 68 Optical density of an MEH-PPV/C_{60} blend device. The absorption of the polymer/fullerene blend on a ITO/PEDOT covered substrate is shown (solid) as well as the absorption of the substrate itself (dotted).

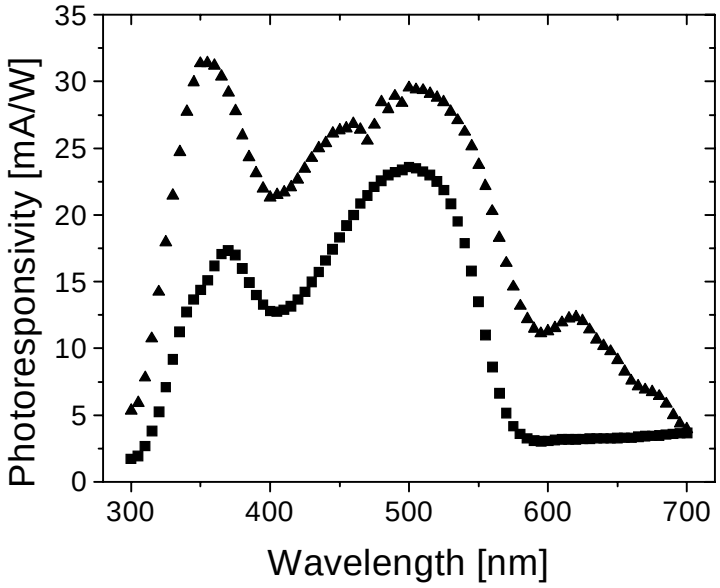

Figure 69 Photoresponsivity of an MEH-PPV/C_{60} blend device. The squares show the PR of the blend device. For comparison an interdiffused (at 250 ^{o}C) MEH-PPV/C_{60} (70 nm / 100 nm) bilayer device is shown (triangles) that has comparable absorption.

two spectra are different. This is probably due to optical absorption in the C_{60} layer followed by hole transfer to the polymer, which is stronger in the interdiffused bilayer devices since they have a layer of pristine C_{60}.

The I-V characteristics of the blend device are plotted on a semi-log scale in Figure 70 and on a linear scale in Figure 71. The devices have 4 orders of magnitude rectification in the dark and 3 orders of magnitude rectification under illumination. The V_{OC} is 0.57 V and *FF* is 0.38 (at 470 nm, 3.8 mW/cm^2). The parameters of the I-V curve are much better than the I-V parameters measured for the interdiffused device. There, the rectification in the dark is 2 orders of magnitude and 1 order of magnitude under illumination. The V_{OC} was measured as 0.47 V and the *FF* was determined to be 0.25.

These results indicate that overall the performance of the blend devices is better than the performance of interdiffused devices for MEH-PPV/C_{60}. This does not seem surprising considering the problems with the interdiffusion due to the low miscibility of C_{60} and MEH-PPV.

It should be noted here that is always difficult to compare devices produced from different solvents. Studies show that the choice of solvent can have a significant influence on the performance of devices [63,64]. If a good solvent is used, the polymer chains are long and extended in the solution. Typically, the polymer chains are also extended in the films processed from these solutions. On the other hand, in poor solvents the chains are less extended and will be more coiled together. This is again reflected in the films produced from this solution.

The reason for using 1,2-dichlorobenzene for the blend devices instead of chlorobenzene lies in the better solubility of C_{60} in dichlorobenzene making higher concentration solutions for spin-casting possible. It is not clear in this case how much influence the different solvent has on the device performance. It is believed, though, that most of the improved I-V characteristics in the blend devices is due to the better morphology of blend devices.

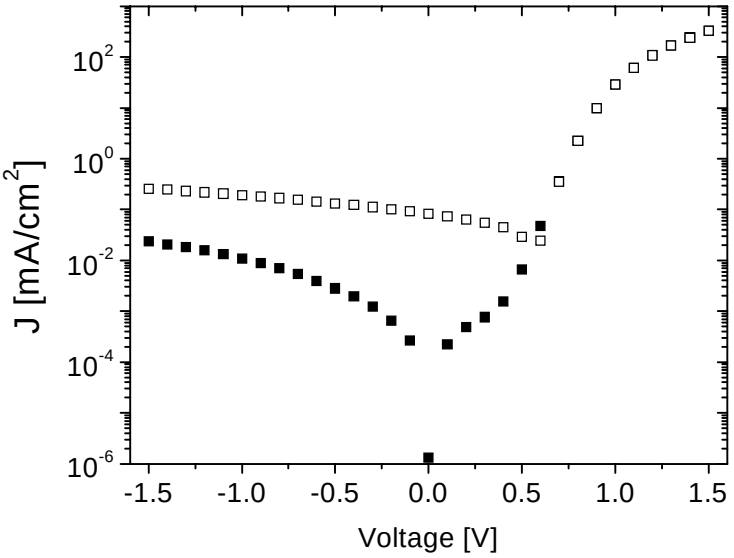

Figure 70 I-V characteristic of an MEH-PPV/C_{60} blend device. The dark I-V (solid) has 4 orders of magnitude rectification and the illuminated I-V (open) has 3 orders of magnitude rectification (at 470 nm, 3.8 mW/cm^2). The data are identical above 0.6 V.

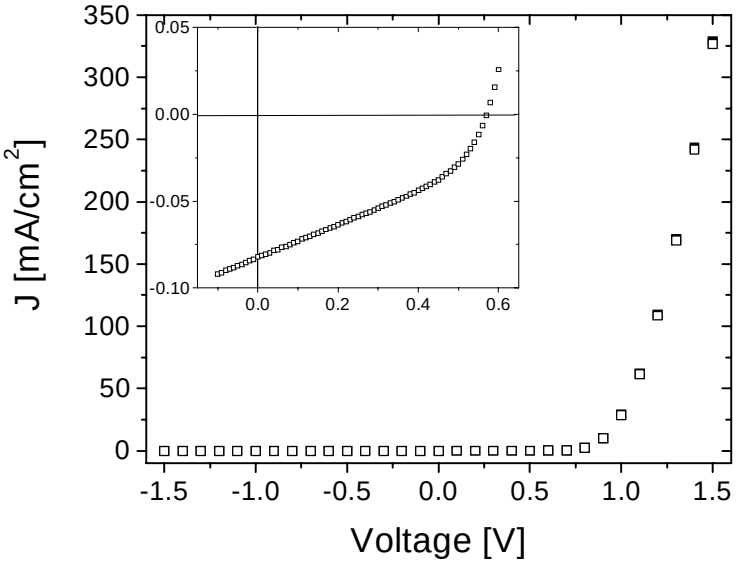

Figure 71 Linear I-V characteristic of an MEH-PPV/C_{60} blend device. The dark (solid) and illuminated (open) I-V curves are shown and overlap nearly identically on this scale. The inset shows the illuminated I-V curve in the 4th quadrant. V_{OC} is 0.57 V and *FF* is 0.38 (at 470 nm, 3.8 mW/cm^2).

5.7 Conclusions

In this chapter, studies were presented where the interface between the polymer MEH-PPV and the fullerene C_{60} in photovoltaic devices was improved by thermally controlled interdiffusion. This interdiffusion led to a closer proximity of electron donor and acceptor material therefore improving the charge separation needed for efficient photovoltaic devices. The improved interface was concluded from the observation of photoluminescence quenching and concomitant increase in photocurrents.

The influence of the polymer layer thickness on the photocurrents was studied showing that the choice of layer thickness is critical for the efficiency of devices. The interdiffusion process could be monitored *in situ* allowing for future studies to improve time-temperature cycles for optimum efficiency of devices.

TEM studies showed clustering of the C_{60} due to strong phase separation. This indicated that the two materials chosen for this initial study are not a good match due to the low miscibility of C_{60} with MEH-PPV. These findings point out the importance of a detailed knowledge of the donor and acceptor materials used in the devices. Only materials that show good miscibility are candidates for devices produced by the thermally induced interdiffusion process.

Comparison of devices produced from a blend of MEH-PPV and C_{60} with devices produced by interdiffusion showed that even though the photocurrents were higher in interdiffused devices, the I-V characteristics were better in the blend devices.

The overall power conversion efficiency of MEH-PPV/ C_{60} interdiffused devices was a relatively modest 0.3 % under monochromatic illumination at 470 nm (3.8 mW/cm^2). Yu *et al.* [6] achieved power conversion efficiencies of 2.9 % under monochromatic illumination (20 mW/cm^2 at 430 nm) in devices produced from a blend of MEH-PPV and PCBM. A comparison of these results is not really fair because of the much better miscibility of PCBM and MEH-PPV compared to C_{60}. This simply emphasizes how important a good match of donor and acceptor material is for the interdiffusion process. Considering the miscibility problems in the MEH-PPV/C_{60} system it is actually impressive how good of a performance could still be achieved by

interdiffusing two materials that have low miscibility. The next chapter shows how improved miscibility leads to improved performance for interdiffused devices.

Chapter 6

P3OT/C_{60} Devices

In Chapter 5, the concept of thermally controlled interdiffusion was introduced to improve the interface between donor polymer and acceptor fullerene in photovoltaic devices. While the concept was successfully used for MEH-PPV as the donor polymer and C_{60} as the acceptor, the studies indicated that these two materials were not an ideal combination. The main limiting factor was the low miscibility of C_{60} in MEH-PPV leading to the limited interdiffusion of large clusters of C_{60} into the polymer bulk.

In an attempt to improve the interdiffusion of the donor and acceptor material, a different donor polymer with better miscibility for C_{60} was chosen. The new donor polymer is a soluble polythiophene derivative, the regioregular poly(3-octylthiophene) (P3OT). Schlebusch *et al.* report interdiffusion of C_{60} into the P3OT bulk occurring at room temperature [65]. In this study a monolayer of C_{60} was sublimed onto a P3OT film

and its presence confirmed by X-ray absorption near edge spectroscopy. After 28 minutes at room temperature the C_{60} layer had fully diffused into the P3OT bulk. This shows the good miscibility of P3OT and C_{60}. It is therefore expected that in our devices, C_{60} might interdiffuse even during and after sublimation. PL quenching observed in unheated bilayer devices (Section 6.3) confirms the interdiffusion of C_{60} at room temperature observed by Schlebusch *et al.*. For an efficient charge transport through the C_{60} phase however, there needs to be a sufficient amount of C_{60} in the polymer bulk. This degree of interdiffusion is not expected at room temperature but only at elevated temperatures.

Another nice feature of the P3OT is the sulfur atom in the polymer backbone. This sulfur content can be used in Auger spectroscopy to test for the polymer concentration in the surface layer of a film. When combining Auger spectroscopy with a layer by layer etching technique, a depth profile of the film can be created showing the polymer concentration as a function of film depth.

6.1 Unheated Devices

In the first step, a series of single and bilayer devices was produced that were not heat-treated. P3OT was spin-cast from a 1.5 % wt/vol chloroform solution onto glass substrates coated with ITO and PEDOT. Typical thickness of the P3OT films was 100 nm. Devices were then annealed in a vacuum system at 120 ^{o}C for 1 hour. Al evaporation and C_{60} sublimation were done as described in the previous chapter.

6.1.1 Single Layer Devices

The optical density of P3OT is shown in Figure 72. The absorption onset is at 670 nm and the peak absorption is at 512 nm. Compared to MEH-PPV, this is a slight red shift of the absorption spectrum and is a better match for the solar spectrum (see Figure 73).

The external quantum efficiency of a single P3OT layer (Figure 74) shows the photocurrent onset at the absorption onset. It then has a maximum at 570 nm and minimum at 510 nm before it increases again. Below 350 nm, the absorption of the substrate prevents photons from entering the device and therefore cutting off the *EQE*.

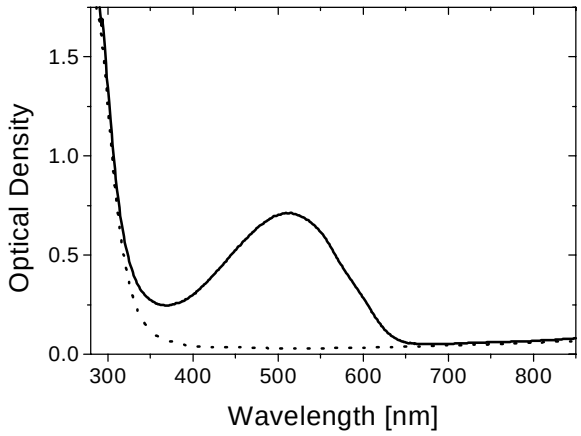

Figure 72 Optical density of a P3OT single layer. The peak absorption of a 100 nm P3OT film (solid) is at 512 nm and the absorption onset is at 670 nm. Also shown is the absorption of the ITO-PEDOT substrate (dotted).

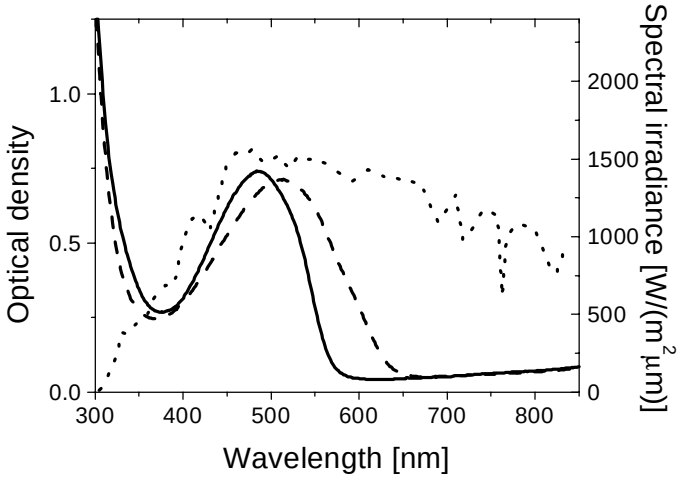

Figure 73 Optical densities of an MEH-PPV and a P3OT film. The absorption of a 100 nm P3OT film (dashed) is clearly red shifted compared to a 90 nm MEH-PPV film (solid) absorption. Also shown is the AM1.5 solar spectrum (dotted). The P3OT film absorption covers a wider range of wavelengths of the solar spectrum than the MEH-PPV film.

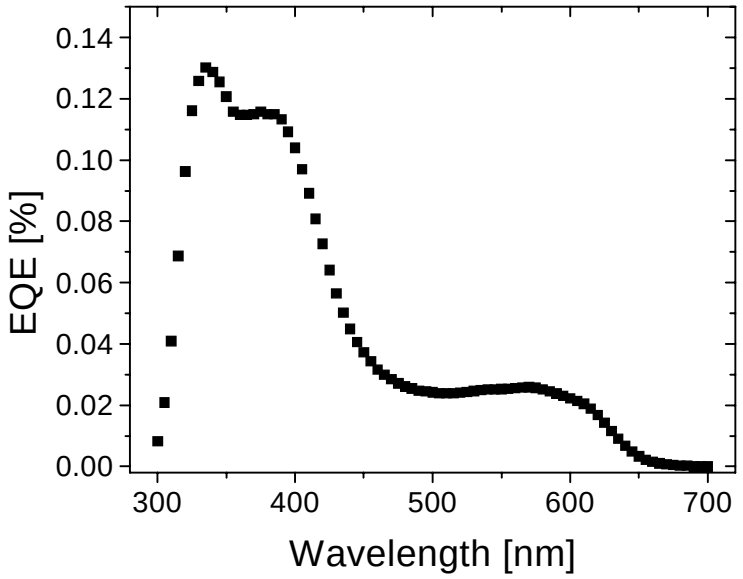

Figure 74 External quantum efficiency of a P3OT single layer device. The photocurrent of the device starts at the absorption onset but does not show a maximum at peak absorption due to the filter effect.

The same effect occurs in MEH-PPV devices. The minimum of *EQE* at the absorption maximum is due to the filter effect of the polymer bulk.

The I-V characteristics of a P3OT single layer device are shown in Figure 75 and Figure 76. The devices show 3 orders of magnitude rectification in the dark and more than 2 orders of magnitude rectification under illumination. The open circuit voltage is found to be 0.25 V and the fill factor is about 0.25.

Altogether, the results for the P3OT single layer devices are very similar to the MEH-PPV single layer devices. The main difference is the red shift of the P3OT absorption, which results in a red shift of the photocurrents.

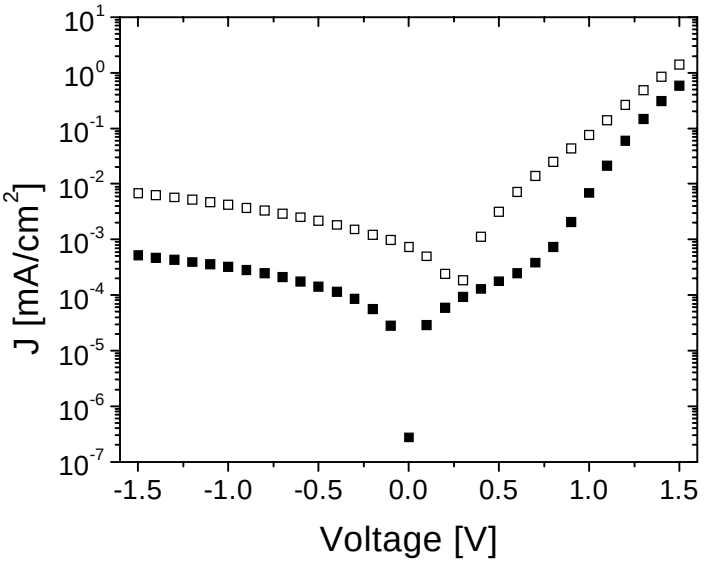

Figure 75 I-V characteristic of a P3OT single layer device. The device has 3 orders of magnitude rectification in the dark (solid) and 2 orders of magnitude rectification under illumination (open). The V_{OC} is found to be below 0.3V.

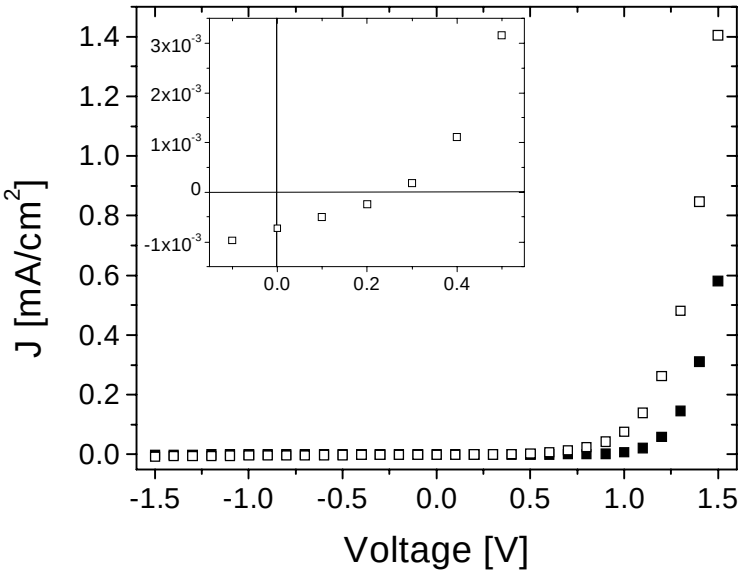

Figure 76 Linear plot of the I-V characteristic of a P3OT single layer device. Solid squares show the dark I-V and open squares show the illuminated I-V. The inset shows the I-V characteristic of the 4th quadrant. The behavior is nearly linear indicating a low *FF* of ~0.25.

6.1.2 Bilayer Devices

The optical density of a P3OT/C_{60} bilayer device is shown in Figure 77. In addition, the graph shows the absorption of a P3OT single layer. The *EQE* for this device is shown in Figure 78. Upon adding a layer of C_{60}, the *EQE* improves by an order of magnitude throughout the spectrum. The photocurrent slowly increases in the region of C_{60} absorption around 700 nm. At the absorption onset of P3OT, it shows a sharp increase but is relatively constant between 500 and 600 nm. Below 500 nm, it increases to a peak at 435 nm.

The shape of the photocurrent spectrum therefore does not match the absorption spectrum. It does not show peak photocurrents in regions of maximum absorption and instead has the photocurrent peak in a region of weaker absorption. This is the same behavior that was observed previously in MEH-PPV/C_{60} bilayer devices and is due to the filter effect of the polymer bulk. In the P3OT devices, this effect is not nearly as extreme as it was in the MEH-PPV devices. This already indicates that there are some differences between the polymer donor materials. In the MEH-PPV devices, a reduced filter effect

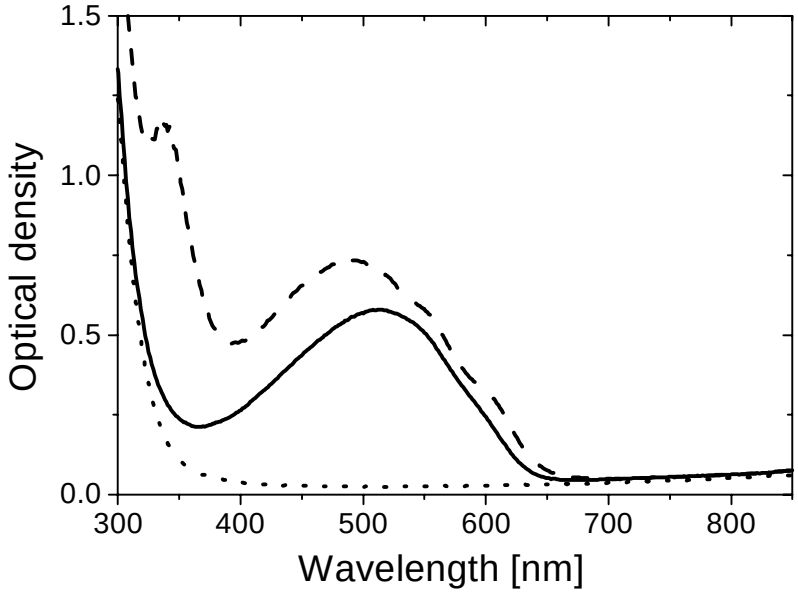

Figure 77 Optical density of a P3OT/C_{60} bilayer device. The dotted line shows the absorption of the ITO-PEDOT substrate, the solid line of the P3OT single layer, and the dashed line of the P3OT/C_{60} bilayer.

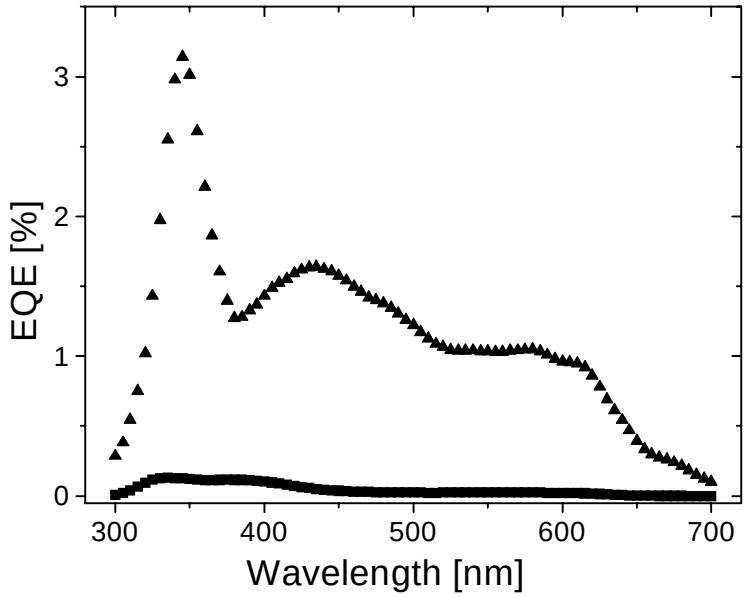

Figure 78 *EQE* spectrum of an unheated P3OT/C_{60} bilayer device. The *EQE* of the bilayer system (up triangles) increases by more than an order of magnitude compared to a P3OT single layer device (squares).

was attributed to low amounts of C_{60} diffusing into the MEH-PPV bulk. In the case of P3OT, this interdiffusion might be expected to occur during the sublimation of C_{60}, in accordance with the reports by Schlebusch *et al.*. This issue will be discussed more in Section 6.3 where the photoluminescence of the devices is studied.

The I-V characteristics of the P3OT/C_{60} bilayer devices are shown on a semilog scale in Figure 79 and on a linear scale in Figure 80. At ±1.5 V the devices show 4 orders of magnitude rectification in the dark and 3 orders of magnitude rectification under illumination (470 nm, 3.8 mW/cm^2). The V_{OC} is 0.14 V and *FF* is calculated to be 0.41. The reason for the low V_{OC} is not immediately clear. Shorts due to pinholes that might arise from fast evaporation of chloroform during spin casting would cause the fill factor to drop down to 0.25. Also, devices with shorts would not show the strong rectification that these devices have. Typically, reduction of the V_{OC} because of low current generation I_G also goes along with a reduction of the fill factor, but the rectifying behavior of the device is not influenced. It is therefore likely that the low V_{OC} is due to low photocurrent generation in the device. This conclusion is in agreement with the fact that, in the

unheated bilayer devices, the interface between donor and acceptor is not optimized yet and the charge separation and charge transport need improvement.

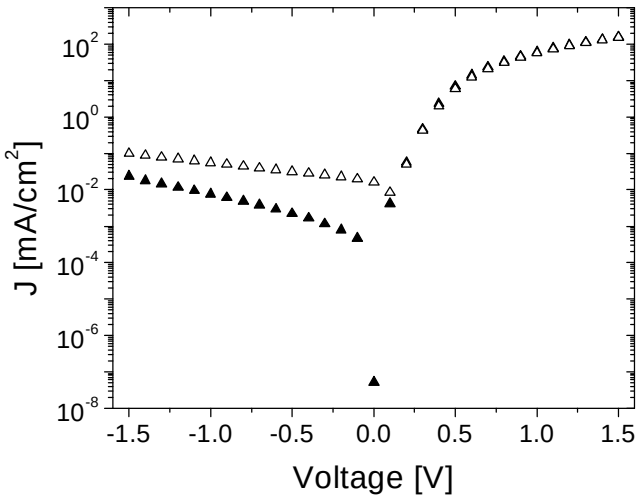

Figure 79 I-V characteristic of an unheated P3OT/C_{60} bilayer device on a semi-log scale. The device shows 4 orders of magnitude rectification in the dark (solid) and 3 orders of magnitude rectification under illumination (open) at 470 nm 3.8 mW/cm^2.

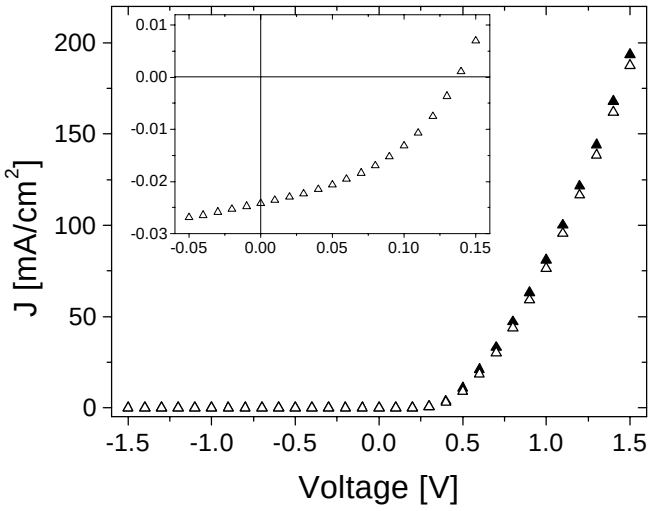

Figure 80 Linear I-V characteristic of an unheated P3OT/C_{60} bilayer device in the dark (solid) and under illumination (open). The inset shows the 4th quadrant of the illuminated I-V. The V_{OC} is found to be 0.14 V and the *FF* is calculate as 0.41. Illumination was done at 470 nm, 3.8 mW/cm^2.

6.2 Heated Devices

Since P3OT is a microcrystalline polymer, it has both a melting point T_m and a glass transition temperature T_g. Thus, P3OT has two characteristic temperatures that might have a significant influence on the interdiffusion. While the interdiffusion of C_{60} into the P3OT bulk should already be good above T_g, heating above the melting point might allow an even better movement of C_{60} into the P3OT bulk.

To better understand the importance of T_m on the interdiffusion process, heat cycles with temperatures above and below T_m (187 ^oC) were chosen. The temperature cycles used were 210 ^oC for 5 minutes and 130 ^oC also for 5 minutes. A heating time of 5 minutes turned out to be good for MEH-PPV/C_{60} devices and was therefore used in these studies as well. More studies should be done to determine the optimum time-temperature cycle for the interdiffusion heating. T_g could not be determined but is expected to be below 100 ^oC. No heat cycles below T_g were tried.

The *EQE* spectra of both heat-treated devices are shown in Figure 81. The two spectra are nearly the same, indicating that for the photocurrents it does not matter whether the heat-treatment is done below or above T_m. For both temperature cycles, the *EQE* has improved by an order of magnitude throughout the whole spectrum. In addition, the *EQE* spectrum better matches the absorption spectrum. This indicates that a bulk-heterojunction has been created successfully.

The I-V characteristics of the interdiffused devices are plotted on a semi-log scale in Figure 82. The devices heated below T_m have 4 orders of magnitude rectification in the dark and 3 orders of magnitude rectification under illumination. This is the same rectifying behavior that the unheated bilayer devices showed. The rectification is reduced to 3 orders of magnitude in the dark and 2 orders of magnitude under illumination when the temperature of the heat-treatment is raised above the melting temperature (210 ^oC).

The linear I-V curves and a magnification of the 4th quadrant are plotted in Figure 83 and Figure 84. The V_{OC} of devices heated at 130 ^oC is 0.36 V and the *FF* is 0.57. This is a dramatic increase compared to the unheated bilayer. For devices heated at 210 ^oC, the V_{OC} is 0.24 V and *FF* is 0.32. The V_{OC} and the *FF* drop somewhat for heating at 210 ^oC compared to 130 ^oC.

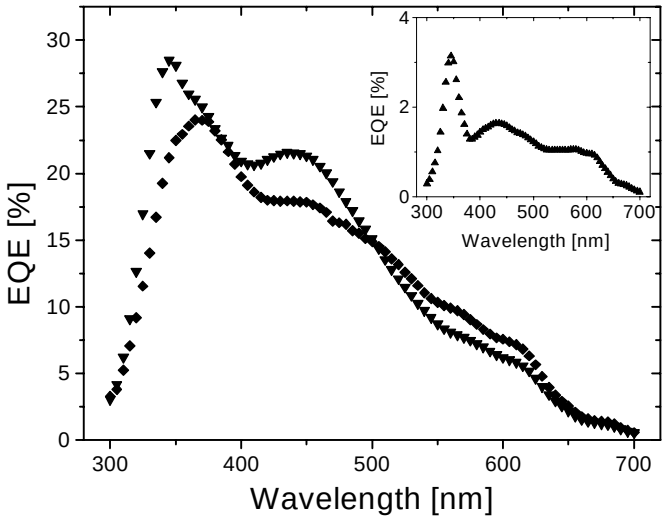

Figure 81 *EQE* spectrum of heat-treated P3OT/C_{60} bilayer devices heated at 130 ^{o}C (down triangles) and at 210 ^{o}C (diamonds). Both were heated for 5 minutes at the setpoint temperature, are similar, and are one order of magnitude larger than the untreated bilayer device (shown in the inset).

The power conversion efficiency of the P3OT/C_{60} devices heated at 130 ^{o}C was calculated with equation 2.8 to be 1.5 % under monochromatic illumination at 470 nm (3.8 mW/cm^2).

In conclusion it can be said that heating above T_m does not give better photovoltaic performance than heating below T_m but above T_g. While the *EQE* is improved by the same factor, the I-V characteristics are much more desirable when the heat-treatment is below T_m.

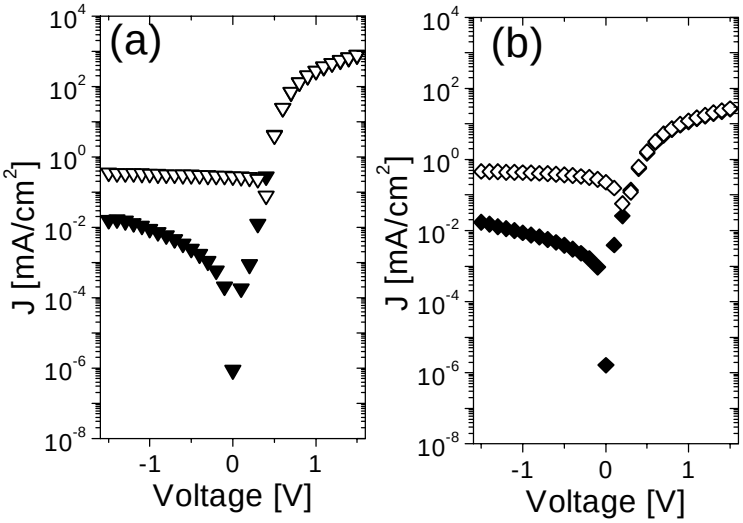

Figure 82 I-V characteristic of heat-treated P3OT/C_{60} bilayer devices on a semi-log scale. The device heated at 130 ^{o}C (a) shows 4 orders of magnitude rectification in the dark (solid) and 3 orders of magnitude under illumination (open). The device heated at 210 ^{o}C (b) has 3 orders of magnitude rectification in the dark (solid) and 2 orders of magnitude under illumination (open). Illumination was at 470 nm, 3.8 mW/cm^2.

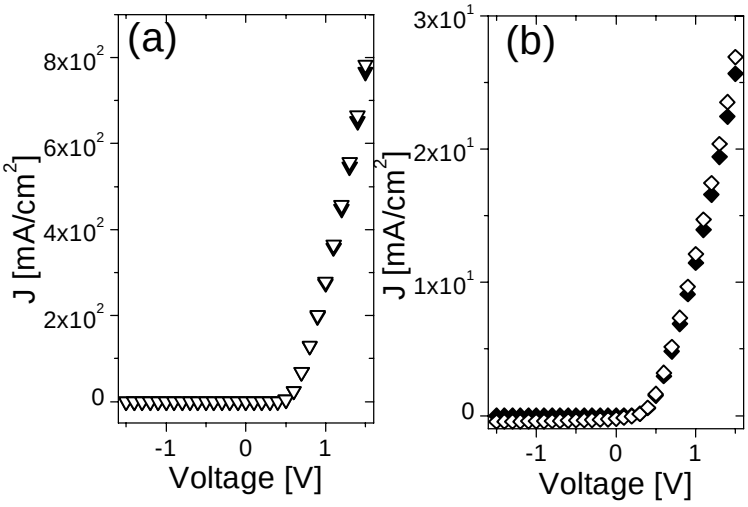

Figure 83 Linear I-V characteristic of heat-treated bilayer devices. (a) shows the device heated at 130 ^{o}C in dark (solid) and illumination (open), (b) shows shows the device heated at 210 ^{o}C in dark (solid) and illumination (open).

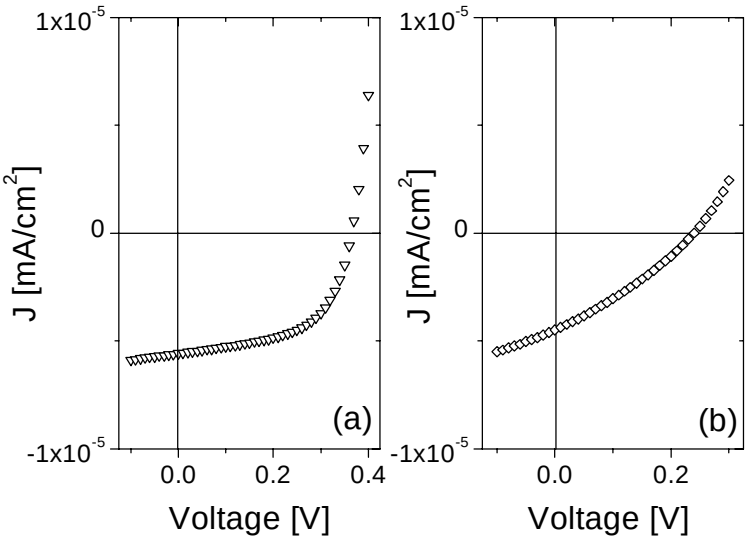

Figure 84 I-V characteristic of heat-treated P3OT/C_{60} bilayer devices in the 4th quadrant under illumination. The bilayer heated at 130 °C (a) has V_{OC} of 0.36 V and *FF* of 0.57, the bilayer heated at 210 °C (b) has V_{OC} of 0.24 V and *FF* of 0.32.

6.3 Photoluminescence

Since the photoluminescence is weaker in the P3OT devices than in MEH-PPV, a stronger excitation source was needed. For the PL measurements of the P3OT devices, an Ar-Ion laser was used. The beam diameter was 1.5 mm with an intensity of 450 mW/cm^2 at a wavelength of 488 nm. The sample was illuminated through the ITO/PEDOT-coated glass substrate to prevent absorption in the C_{60} layer. The PL signal was again detected with an Ocean Optics fiber optics spectrometer under a 45 ° angle compared to the incident light beam.

The detected PL signals for single layer, bilayer, and heated bilayer devices are shown in Figure 85. Single layer devices show a strong photoluminescence with a peak at 670 nm and a shoulder at 705 nm. Upon sublimation of a layer of C_{60}, the PL intensity drops by 2 orders of magnitude. This shows that the PL is strongly quenched throughout the P3OT bulk when C_{60} is sublimed. This PL quenching can only occur when excitons

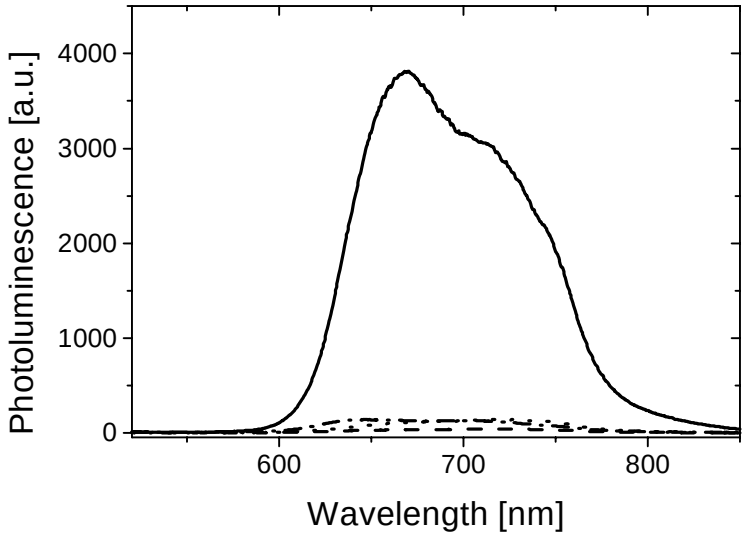

Figure 85 Photoluminescence of P3OT/C_{60} devices. The P3OT single layer device (solid) shows strong PL. The PL is quenched for bilayer devices (dashed) and devices heated at 130 ^{o}C (dotted) and 210 ^{o}C (dash-dotted). Excitation light was 488 nm from an Ar-Ion laser with 450mW/cm^2 and the integration time of the spectrometer was 250 ms.

are dissociated throughout the bulk, which takes place when C_{60} is available as an electron acceptor. The PL data for an unheated bilayer therefore seem to indicate that a significant amount of C_{60}, enough to quench the PL by 2 orders of magnitude, already diffuses into the P3OT bulk during or after sublimation. This observation is in agreement with the weak filter effect observed in the photocurrent spectra of the unheated bilayer devices. It is not known here if the interdiffusion takes place immediately during the C_{60} deposition or if it is a slower process that takes place afterwards. The temperature increase of the film during C_{60} sublimation should be minor. The temperature of the glass substrate does not change measurably during the sublimation as was observed with a temperature probe during the process.

Compared to the unheated bilayer, the heat-treated bilayer devices show a stronger PL signal. To better resolve differences in the bilayer devices, the PL spectra were measured again with a longer integration time (3 s) to obtain stronger PL signals. The measured data are shown in Figure 86. The PL intensity of the heated bilayer devices is about 3 times stronger than the unheated device. This is an unexpected result since the photocurrent spectra indicate a better interface between P3OT and C_{60} in the

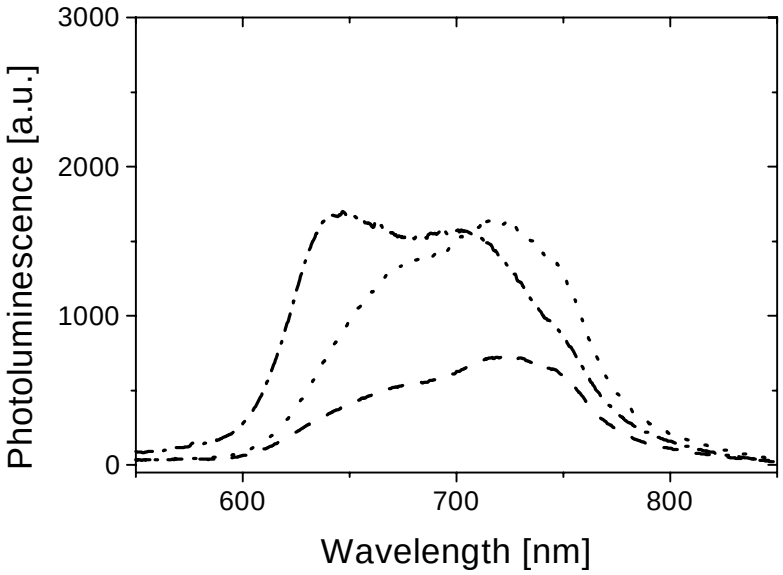

Figure 86 Photoluminescence of P3OT/C_{60} devices. The PL signal from the bilayer (dashed) is weaker than from the devices heated at 130 ^{o}C (dotted) and 210 ^{o}C (dash-dotted). This increase in PL signal upon heat-treatment is probably due to changes in morphology of the films. Excitation light was 488 nm from an Ar-Ion laser with 450mW/cm^2 and the integration time of the spectrometer was 3 s.

heated devices, which should lead to stronger PL quenching. On the other hand, a similar behavior was observed in the MEH-PPV/C_{60} devices that were heated above the T_g of MEH-PPV. There, the increase in PL intensity upon heating above T_g was related to clusters of C_{60} that moved into the MEH-PPV and thereby changed the film morphology. A similar effect might be observed here but cannot be identified for certain from the PL data. TEM studies that show the film morphology on a microscopic level provide an explanation as described in Section 6.4.2.

In addition to the increase in PL intensity due to heat-treatment, there is a change in shape of the PL signal for devices heated above the melting temperature of P3OT. While the unheated bilayer and the bilayer heated below T_m (130 ^{o}C) have a shoulder at 680 nm and a peak at 720 nm, the bilayer heated above T_m has two peaks, one at 644 nm and one at 700 nm. The reason for this blue-shift and change in shape of the PL spectrum might be related to changes in the crystallinity of the P3OT. These changes can result from two factors:

- The crystallinity of a polymer film depends on the temperature history of the film (see e.g. [66]). When the P3OT is heated above T_m, the crystallites melt and then recrystallize during the cooling process. Therefore the crystallinity of the sample might be different from the films that were not heated above T_m.
- The crystallinity might be influenced by molecules or small clusters of C_{60} diffusing into the P3OT, preventing recrystallization of the polymer chains.

It is not determined in this work whether or not the crystallinity is the cause for changes in the PL spectrum and, if so, which of the two factors influences the PL of the bilayer heated above T_m. It might be a combination of the two.

6.4 Morphology Studies

Since the *EQE* and PL spectra as well as the I-V curves do not provide information about the details of the morphology of the films, other techniques need to be implemented. In addition to transmission electron microscopy as was used for MEH-PPV/C_{60} devices, the sulfur content in P3OT also allowed an elemental analysis of the surface layer. In combination with repeated milling, a depth profile of the film could be obtained.

6.4.1 Auger Spectroscopy

Auger spectroscopy with ion beam milling was used to study the morphology of an unheated P3OT bilayer device and a bilayer heated at 130 ^{o}C. The step width for each etching step was chosen to be 0.5 nm. One limitation of this analysis method is the penetration depth of the electron beam during the Auger spectroscopy, which is on the order of 5 nm. In addition, the Ar ion milling is like a sandblasting technique and does not necessarily remove a perfectly smooth layer of the surface.

A quantity commonly plotted in Auger spectroscopy is the peak to peak (P-P) signal. In Auger spectroscopy, the number of electrons of certain energy *N(E)* is recorded. For elements in the surface, the *N(E)* spectrum has a characteristic signal on top of the baseline of the *N(E)* spectrum without a sample. This characteristic signal becomes more obvious when taking the derivative of *N(E)*. In that case a characteristic up peak followed by a down peak is observed. The P-P signal is the area underneath this up and down peak. The stronger the P-P signal at a given electron energy, the more atoms of the associated element are in the surface of the tested film.

Figure 87 shows the P-P Auger signal of an unheated bilayer of P3OT and C_{60} on ITO. The elements monitored are sulfur, which is characteristic of the polymer, indium and oxygen, both of which indicate when the ITO layer is reached. Since C_{60} as well as P3OT contain a lot of carbon, there is no significant change in the P-P signal of carbon between the C_{60} layer and the P3OT layer. Therefore the carbon content was not monitored. In the graph, the sulfur content is zero up to the vicinity of the P3OT/C_{60} interface where it shows a sudden rise and then remains constant until the ITO layer is reached. The position of the interface indicated in the figure was determined from absorption measurements (C_{60} thickness of 110 nm). For the unheated bilayer, the Auger spectroscopy therefore indicates a very distinct interface between P3OT and C_{60} with an interfacial region of less than 25 nm.

The P-P signal of a P3OT/C_{60} bilayer device heated at 130 ^{o}C is plotted versus the film depth in Figure 88. The sulfur content starts to rise after about 35 nm milling through the film. The concentration of sulfur then slowly rises over more then 100 nm before it levels off and stays constant until the milling reaches the ITO layer. The small step at 180 nm depth is due to an adjustment in the electronics of the Auger system. The C_{60} film in this case was determined to be 80 nm from the optical density. After heating at 130 ^{o}C, the P3OT/C_{60} interface is distributed over more than 100 nm (35 to 135 nm of the scan).

The heat-treatment at 130 ^{o}C has therefore washed out the distinct interface between P3OT and C_{60}. The data indicate that there is a concentration gradient of the P3OT content in the film throughout most of the bulk of the device. This is exactly the morphology of the active layer that was intended. The interdiffusion of polymer donor

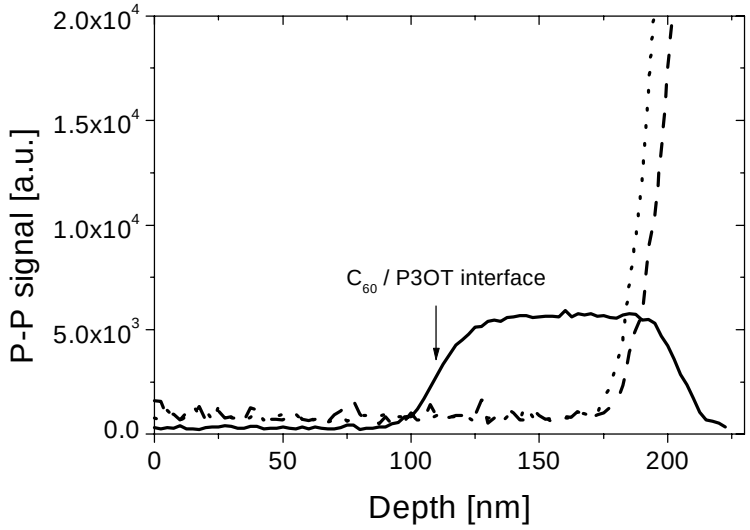

Figure 87 Depth profile of an unheated P3OT/C_{60} bilayer device. The concentration of sulfur (solid), indium (dotted), and oxygen (dashed) was monitored. The arrow indicates the position of the P3OT/C_{60} interface as determined from absorption measurements. The scan shows a rather sharp interface between P3OT and C_{60}.

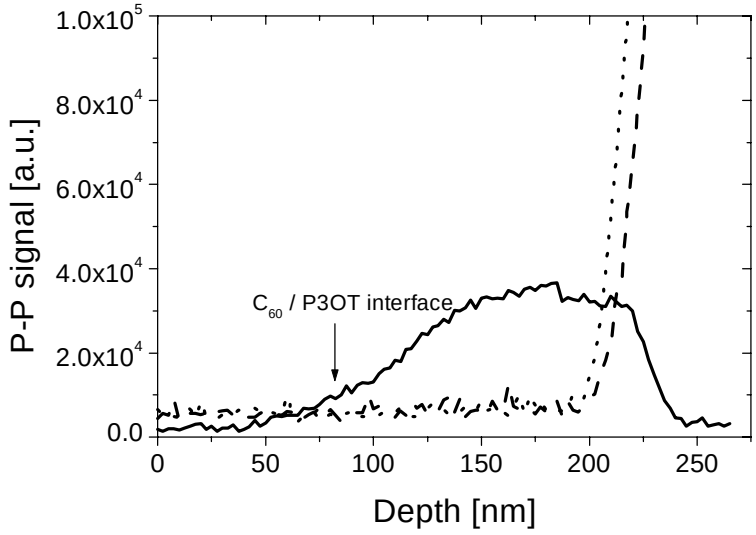

Figure 88 Depth profile of a P3OT/C_{60} bilayer device heated at 130 ^{o}C. The concentration of sulfur (solid), indium (dotted) and oxygen (dashed) was monitored. The arrow indicates the position of the P3OT/C_{60} interface as determined from absorption measurements.

and fullerene acceptor has created a concentration gradient of the two materials with the pristine polymer at the ITO interface and C_{60} at the Al interface.

It should be noted here that Auger spectroscopy always gives an average of the element concentration in the tested area. It can't give information about possible clustering of the C_{60} as it was observed in the previous chapter. For this information, TEM studies are necessary. Also, the method used here cannot distinguish between C atoms from the polymer and the C_{60}. The data therefore does not show whether there is a small amount of C_{60} distributed in the polymer layer of the unheated device. According to the PL data, this was likely the case.

What the Auger spectroscopy can do is detect regions throughout the film where the concentration of polymer has been significantly reduced due to large amounts of C_{60} diffusing into the polymer bulk. Also, it can detect regions where the polymer has moved into the C_{60} layer.

6.4.2 Transmission Electron Microscopy

TEM studies on P3OT/C_{60} films turned out to be much more difficult then the studies done on MEH-PPV/C_{60} films. Since P3OT does not lift off the glass substrate when immersed in water, a suitable substrate had to found with the following conditions:

- It had to be soft enough to be microtomed. The diamond knife of the microtome cannot cut Al foil or even glass. Typically, polymer materials are used as substrates for microtoming.
- The substrate had to be able to withstand a heat-treatment of up to 210 ^{o}C.
- The substrate should be transparent so that the absorption of the films could be measured.

The substrate chosen for these experiments is polyethersulfone (PES). A few sample sheets of PES were provided by Sheldahl. The PES had a hard coat of an acrylic/polyurethane blend and could withstand temperatures of more than 210 ^{o}C. Still, the substrate was not an ideal choice for the microtoming. The P3OT had a tendency to

delaminate from the PES substrate during microtoming. Despite this, the TEM results obtained with this substrate give a reasonable picture of the film morphology.

Films were produced on the PES substrate in the same manner as on the ITO/PEDOT-coated glass slides. Small pieces of the film were then imbedded in epoxy in order to microtome cross sections of the film.

Figure 89 is a TEM image of an unheated P3OT/C_{60} bilayer. The picture shows that the contrast between polymer and fullerene is not as good as was observed in MEH-PPV/C_{60} films. But the two layers can still be distinguished well. The darker phase is the C_{60}. The interface between P3OT and C_{60} is smooth and distinct. There are no clusters of C_{60} in the P3OT bulk. This confirms that even though there might be a low concentration of C_{60} in the P3OT that quenches the PL, there is no large scale interdiffusion at room temperature or during sublimation.

Figure 89 TEM image of an unheated P3OT/C_{60} bilayer. The image shows two rather distinct layers. The C_{60} has the darker contrast. There are no clusters of C_{60} in the P3OT layer. This shows that diffusion of clusters of C_{60} does not occur at room temperature or during sublimation of C_{60}.

TEM images of a P3OT/C_{60} bilayer heated at 130 ^{o}C are shown in Figure 90. The right picture is a magnification of the picture shown on the left. This film turned out to give the most difficulties during the microtoming as can be seen from the regions where the film delaminated from the substrate. Despite these problems, the TEM images indicate that the distinct interface between the P3OT and the C_{60} does not exist in the films heated at 130 ^{o}C. The interface has become much rougher and clusters of C_{60} have moved into the P3OT bulk. Even though it is difficult to see clearly in the images, it seems that the film has a concentration gradient of P3OT and C_{60} through most of the film's cross-section, which is indicated by a gradient in contrast. This would confirm the observations made in the Auger spectroscopy. At the edges of the film, C_{60} is dominant on one side and P3OT is dominant on the other side.

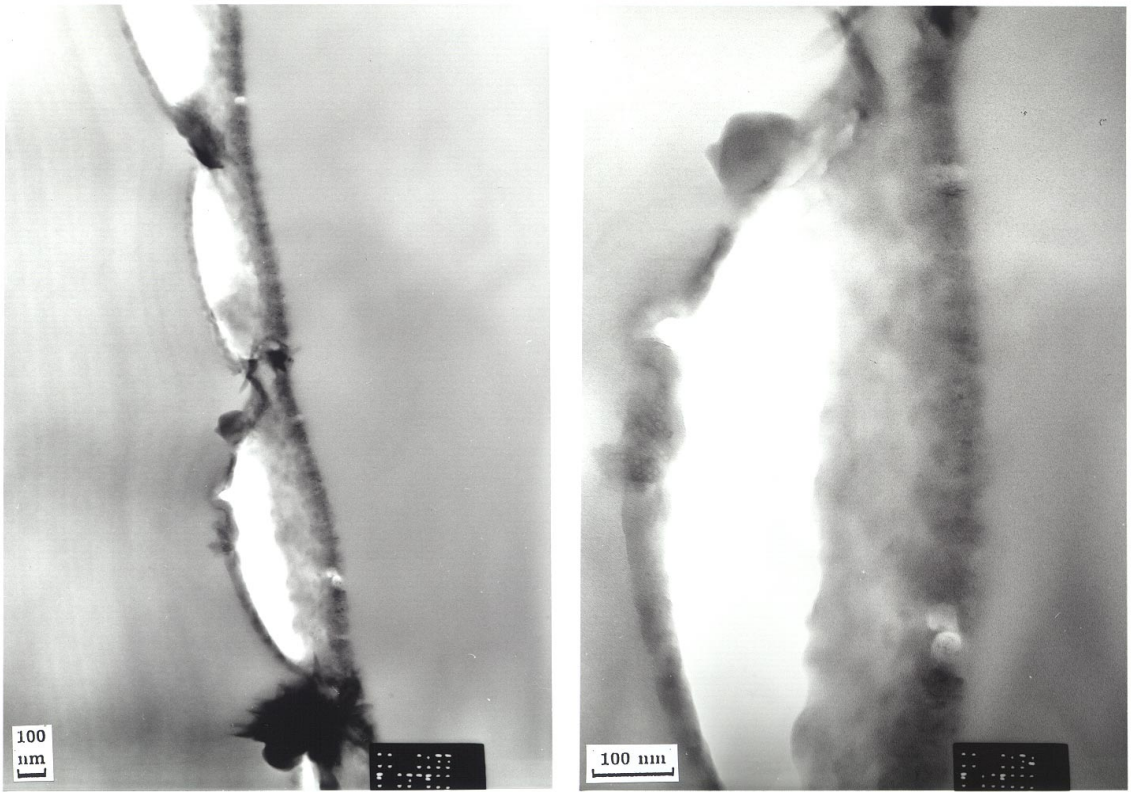

Figure 90 TEM images of a P3OT/C_{60} bilayer heated at 130 ^{o}C. The image on the right is a magnification of the image on the left to better see the morphology. The film has come off the PES substrate in most areas, but TEM images of the film could still be taken. The images show that the interface between P3OT and C_{60} has become rougher than in the unheated bilayer and clusters of C_{60} have moved into the film.

In the bilayer heated at 210 ^{o}C, this process has gone even further. In Figure 91, there is no longer a recognizable bilayer. The TEM graph shows darker and lighter regions randomly distributed throughout the thickness of the former bilayer. It seems that P3OT and clusters of C_{60} are completely blended throughout the film. This indicates that, for this film, the interdiffusion was carried on beyond the intended structure.

The observation of C_{60} clustering in both heated bilayers is consistent with the increase in PL signal for these films. The C_{60} clusters scatter the light of the excitation beam so that a larger volume of the film is illuminated. This leads to a stronger PL from these films compared to the unheated bilayer where the C_{60} film is rather smooth.

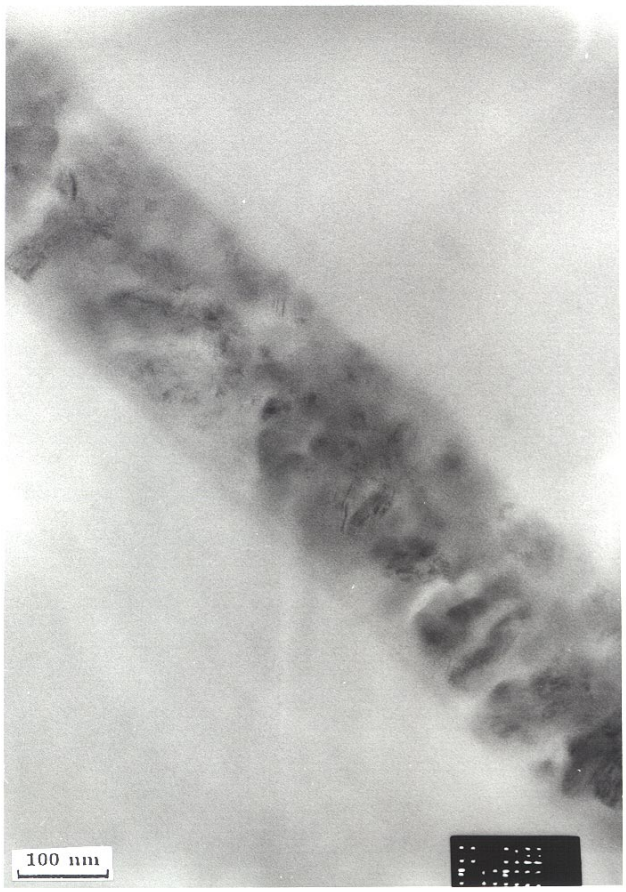

Figure 91 TEM image of a P3OT/C_{60} bilayer heated at 210 ^{o}C. The bilayer structure has completely disappeared. Instead, there are darker and lighter regions indicating that the film is a blend of P3OT and C_{60} clusters.

6.5 Conclusions

In this chapter, the studies of thermally-controlled interdiffusion of a conjugated polymer and fullerene in organic photovoltaic devices that were introduced in the last chapter were continued. The interdiffusion and photovoltaic performance were improved by choosing a polymer that has better miscibility for C_{60}.

Again, the photocurrents and PL were studied for unheated and heated devices. The photocurrents showed an order of magnitude increase and good match to the absorption spectrum upon heating. This indicated that a bulk-heterojunction was formed. The PL was quenched by two orders of magnitude already when C_{60} was sublimed on top of the P3OT. This PL quenching in the unheated bilayer illustrated the much better miscibility of C_{60} in P3OT, since C_{60} already moved into the polymer bulk without heating the devices.

The TEM studies and the PL data demonstrated that again the C_{60} formed clusters that migrated into the polymer film when the bilayers were heated. Interdiffusion of these clusters seemed to be easier in this material combination as compared to MEH-PPV and C_{60}.

An important observation is that the I-V characteristic in the heated devices was improved for P3OT and C_{60}. In MEH-PPV/C_{60} devices, the fill factor dropped dramatically in heated devices. Here, the fill factor, open circuit voltage, and short circuit current were significantly improved compared to the unheated bilayer.

The TEM data show that heating above the polymer melting temperature (at 210 ^{o}C) leads to an interdiffusion that goes beyond the structure of a concentration gradient towards a homogeneous blend. The correlating I-V characteristics are not as good as for the devices heated below T_m (at 130 ^{o}C). This seems to indicate that a concentration gradient of P3OT and C_{60} is advantageous over a blend of the two materials.

In addition, Auger spectroscopy in combination with Ar-Ion beam milling was used as another method to study the morphology of the films. Depth profiles acquired with this method showed a rather distinct interface between P3OT and C_{60} in unheated bilayer devices but showed a concentration gradient of the P3OT throughout a large part of the active layer indicating that the intended morphology was actually achieved.

Chapter 7

Conclusions and Future Work

In this thesis, the interface between polymer donor materials and the fullerene acceptor material C_{60} in photovoltaic devices was studied. Starting from a distinct, flat interface with the two materials deposited as separate layers in contact, an interdiffusion of the two materials was induced thermally. In this manner, the materials interdiffused and an interface between donor and acceptor was created throughout the bulk of the active layer. The studies show that the photovoltaic response of conjugated polymer - fullerene materials can be significantly enhanced through nanoscale control of the spatial location of the components.

Initial studies were done on MEH-PPV/C_{60} devices. The improved interface in heat-treated devices is observed in photoluminescence quenching of an order of magnitude and a concomitant increase in photocurrents of an order of magnitude throughout most of the visible spectrum. The PL quenching occurred even at lower concentrations of C_{60} diffused into the polymer bulk. Significant improvements of the

photocurrents only occurred when larger amounts of C_{60} diffused into the polymer bulk creating efficient pathways for charge transport out of the device. Measurements of the I-V characteristics showed that the open circuit voltage of devices was improved from 0.4 V in the unheated bilayer to 0.6 V in devices heated below the glass transition temperature of MEH-PPV and 0.5 V for devices heated above T_g. While photocurrents and open circuit voltage in the heat-treated MEH-PPV/C_{60} devices were improved, the rectification dropped from 3 and 2 orders of magnitude in the dark and under illumination (at 470 nm, 3.8 mW/cm^2), respectively, to 2 and 1 order of magnitude in the heated devices. Also, the fill factor decreased from 0.4 in the unheated bilayer devices to 0.24 and 0.29 in the bilayer devices heated below and above T_g, respectively. The external quantum efficiency in the devices consisting of 90 nm of MEH-PPV and 100 nm of C_{60} was improved from ~0.5 % in the unheated bilayer throughout most of the visible spectrum to more than 5 % in the devices heated above T_g.

In addition, the filter effect in the unheated bilayer devices was significantly reduced upon interdiffusion. The filter effect results from strong absorption of the polymer bulk, thus preventing photons from reaching the polymer-fullerene interface, where efficient charge separation can occur. This leads to low photocurrents in regions of strong absorption. Reduction in the filter effect shows that the interface between polymer and fullerene throughout the bulk of the active layer (a bulk-heterojunction) has been created.

To determine the influence of the polymer layer thickness on the efficiency of the photovoltaic devices, a series of films with MEH-PPV layer thickness of 70 nm, 90 nm, and 110 nm was prepared. In all devices (unheated and heated), the photocurrents increased with decreasing layer thickness. This trend is expected to turn around when the MEH-PPV layer thickness becomes much thinner and therefore the absorption in the devices becomes very small. The results show that the choice of layer thickness is critical for the efficiency of photovoltaic devices. In the 70 nm MEH-PPV devices, the photocurrent spectrum started to match the absorption spectrum, which indicates that in these devices a bulk-heterojunction was formed. The power conversion efficiency in these devices was calculated to be 0.3 % under monochromatic illumination at 470 nm (3.8 mW/cm^2).

Transmission electron microscopy was used to examine the cross section of the interdiffused devices. These studies revealed that C_{60} has a tendency to form clusters that diffuse into the polymer film. The C_{60} clusters are, of course, much less mobile than individual C_{60} molecules and therefore put a constraint on the interdiffusion. Thus, the low miscibility of C_{60} in MEH-PPV hindered the interdiffusion process.

Using P3OT, which is known to have better miscibility for C_{60}, the interdiffusion worked much better and further improved photovoltaic performance is observed. This demonstrates that the choice of materials is critical for the performance of organic photovoltaic devices formed by thermally-induced interdiffusion.

The better miscibility of C_{60} and P3OT was observed even in the unheated bilayer devices. Upon sublimation of a C_{60} layer, the photoluminescence was quenched by 2 orders of magnitude compared to P3OT single layer devices. This demonstrates that some C_{60} can already diffuse into the P3OT bulk at room temperature. Also, the observed filter effect in unheated P3OT/C_{60} bilayer devices is not as strong as in MEH-PPV/C_{60} devices.

In its regioregular form, P3OT is micro-crystalline, thus having a glass transition temperature and a melting temperature. To study the influence of melting the polymer during interdiffusion-heating, devices were heated at temperatures below T_m (but above T_g) and above T_m. In both cases, the photocurrents improved by an order of magnitude compared to the unheated bilayer devices. The *EQE* spectra for devices heated below and above T_m are comparable. Therefore, to maximize the *EQE* it is not necessary to heat above T_m. The *EQE* was found to be up to 28 % in these improved devices and matched the absorption spectrum better than the unheated devices.

In the P3OT/C_{60} devices, the I-V characteristics were also improved by the heat-treatment. The rectification was 4 orders of magnitude in the dark and 3 orders under illumination (470 nm, 3.8 mW/cm^2) at ±1.5 V bias for unheated bilayer devices and bilayers heated at 130 ^{o}C (below T_m). The rectification dropped to 3 orders of magnitude in the dark and 2 under illumination for devices heated at 210 ^{o}C (above T_m). The V_{OC} improves from 0.14 V in the unheated bilayer devices to 0.36 V and 0.24 V in the devices heated below and above T_m. The fill factor improves from 0.41 in the unheated bilayer devices to 0.57 in the devices heated below T_m and drops to 0.32 in the devices heated above T_m. These results show that it is advantageous to keep the temperature below T_m

for the interdiffusion heating. For the best devices (heated at 130 ^{o}C), the power conversion efficiency was calculated to be 1.5 % under monochromatic illumination (470 nm, 3.8 mW/cm^2). As a comparison, the largest monochromatic power conversion efficiencies obtained so far are ~10 %. However, those results were obtained with different polymer and fullerene materials than those employed in this work. Our initial studies demonstrate that the interdiffusion approach has significant potential for fabrication of highly efficient organic solar cells.

For P3OT/C_{60} films, the cross sections of the films were also studied with Auger spectroscopy enabled by the sulfur content of the polymer. The profile of the interdiffused films revealed a concentration gradient of the P3OT through most of the film thickness in contrast to the sharp interface observed in unheated films. Even though there might be inhomogeneities on a microscopic level – TEM studies still showed C_{60} clusters, which Auger spectroscopy cannot detect because it averages over a larger area – the overall trend in the films is a concentration gradient. The intended concentration gradient between donor and acceptor material was therefore achieved in the device morphology using this pair of materials having improved miscibility.

The interdiffusion was also observed *in situ* in MEH-PPV/C_{60} devices. This way, the devices could be measured before, during, and after the interdiffusion. The before and after performance of the devices could be compared. The experiments indicated that the Al electrode puts some constraint on the interdiffusion of C_{60}. Unfortunately, the interdiffusion could not be observed *in situ* for heating above the glass transition temperature of the MEH-PPV because devices failed permanently when heated at temperatures close to the T_g with the Al electrode in place.

As a next step to improve interdiffusion as an approach for efficient organic photovoltaic devices, the electron acceptor material should be replaced by a material that has less tendency to cluster than C_{60}. In addition, the acceptor should have good miscibility in the polymer such that individual molecules should be able to interdiffuse more easily into the polymer bulk. A possible candidate would be the methanofullerene (phenyl-[6,6]-C_{61})-butyric acid methyl ester (PCBM). The bulky side group reduces the tendency for aggregation and improves solubility/miscibility. It is often used in high

concentrations (4:1 by weight fullerene:polymer) without showing problems due to clustering [4,6,12].

With PCBM, the interdiffusion might also be a little bit more controlled. The main constraint on modeling the interdiffusion and drawing conclusions concerning the photocurrent spectra in this work has been the random size of C_{60} clusters. This makes it inappropriate to use the proposed model from Section 2.3.2. With PCBM, the mass transport and the concentration gradient in the active layer might be more homogeneous.

Another interesting aspect of the devices is the crystallinity of P3OT. From this work, it is not clear what influence the crystallinity has on the photovoltaic behavior of the devices. It should be determined whether higher crystallinity of the polymer is advantageous for the photovoltaic efficiency. In future work, the influence of the interdiffusion step on the crystallinity could be studied.

In a final remark, it should be noted that the MEH-PPV/C_{60} devices were remeasured after being stored in a N_2 glove box for one year. The photocurrents had dropped by ~50 % compared to the original measurements. This is most likely due to the handling of the devices in air when being transported from the measurement setup to the glove box and to some small oxygen and moisture content in the glove box itself. Even though the photocurrents dropped, this suggests that by handling the samples carefully during production and immediately encapsulating them to exclude oxygen and moisture these devices can exhibit long-term stability.

In conclusion, it can be said that it is essential to know and control the nanoscale morphology of the active layer in organic photovoltaic devices. The morphology is strongly influenced by the choice of solvent, the miscibility of the polymer and fullerene, and the thermal history of the film. Only in this manner can the structure of the devices be tuned in a way that will maximize the efficiency of photovoltaic devices.

Bibliography

[1] Intergovernmental Panel on Climate Change (IPCC), " Third Assessment Report of Working Group I - Summary for policy makers", (2001) Web page: http://www.ipcc.ch/

[2] C. B. Hatfield ”Oil back on the global agenda.” *Nature* **387**, 121 (1997).

[3] C.J. Campbell, "Oil, gas and make-believe", *Energy Exploration & Exploitation* **19**(2&3), 117-133 (2001).

[4] S.E. Shaheen, C.J. Brabec, N.S. Sariciftci, F. Padinger, T. Fromherz, J.C. Hummelen, "2.5 % Efficient Organic Solar Cells", *Appl. Phys. Lett.* **78**, 841-843 (2001).

[5] M. Granstrom, K. Petritsch, A.C. Arias, A. Lux, M.R. Andersson, R.H. Friend, "Laminated fabrication of polymeric photovoltaic diodes", *Nature* **395**, 257 (1998).

[6] G. Yu, J. Gao, J.C. Hummelen, F. Wudl, A.J. Heeger, "Polymer photovoltaic cells: enhanced efficiencies via a network of internal donor-acceptor heterojunctions", *Science* **270**, 1789-1791 (1995).

[7] P. Peumans, S.R. Forrest, "Very-high-efficiency double-heterostructure copper phthalocyanine/C_{60} photovoltaic cells", *Appl. Phys. Lett.* **80**(2), 338-338 (2002).

[8] W.U. Huynh, J.J. Dittmer, A.P. Alivisatos, "Hybrid nano-rod-polymer solar cells", *Science* **295**, 2425-2427 (2002).

[9] H. Ago, M.S.P. Shaffer, D.S. Ginger, A.H. Windle, R.H. Friend, "Electronic interaction between photoexcited poly(*p*-phenylene vinylene) and carbon nanotubes", Phys. Rev. B **61**(3), 2286-2290 (2000).

[10] L. Chen,D. Godovsky,O. Inganäs, J.C. Hummelen, R.A.J. Janssens, M. Svensson, M.R. Andersson," Polymer photovoltaic devices from stratified multilayers of donor-acceptor blends", *Advanced Materials* **12**(18),1367- (2000).

[11] C.J. Brabec, A. Cravino, D. Meissner, N.S. Sariciftci, M.T. Rispens, L. Sanchez, J.C. Hummelen, T. Fromherz, "The influence of materials work function on the open circuit voltage of plastic solar cells ", *Thin Solid Films* **403-404**, 368-372 (2002).

[12] S.E. Shaheen, R. Radspinner, N. Peyghambarian, G.E. Jabbour, "Fabrication of bulk heterojunction plastic solar cells by screen printing", *Appl. Phys. Lett.* **79**(18), 2996-2998 (2001).

[13] N.S. Sariciftci, L. Smilowitz, A.J. Heeger, F. Wudl, "Photoinduced electron transfer from a conducting polymer to buckminsterfullerene", *Science* **258**, 1474-1476 (1992).

[14] B. Kraabel, D. McBranch, N.S. Sariciftci, D. Moses, A.J. Heeger, "Ultrafast spectroscopic studies of induced electron transfer from semiconducting polymers to C_{60}", *Phys. Rev. B* **50**(24), 18543-18552 (1994).

[15] D. Vacar, E.S. Maniloff, D.W. McBranch, A.J. Heeger, "Charge-transfer range for photoexcitations in conjugated polymer/fullerene bilayers and blends", *Phys. Rev. B* **56**(8), 4573-4577 (1997).

[16] J.J.M. Halls, K. Pichler, R.H. Friend, S.C. Moratti, A.B. Holmes, "Exciton diffusion and dissociation in a poly(p-phenylenevinylene)/C_{60} heterojunction photovoltaic cell", A*ppl. Phys. Lett.* **68** (22), 3120-3122 (1996).

[17] A. Haugeneder, M. Neges, C. Kallinger, W. Spirkl, U. Lemmer, , J. Feldmann, U. Scherf, E. Harth, A. Gügel, K. Müllen, " Exciton diffusion and dissociation in conjugated polymer/fullerene blends and heterostructures", *Phys. Rev. B* **59**, 15346–15351 (1999).

[18] N.S. Sariciftci, L.Smilowitz, A.J. Heeger, F. Wudl, "Semiconducting Polymers (as donors) and Buckminsterfullerene (as acceptor) - photoinduced electron-transfer and heterojunction devices", *Synthetic Metals* **59**(3), 333-352 (1993).

[19] F. Zhang, M. Johansson, M.R. Andersson, J.C. Hummelen, O. Inganas, "Polymer photovoltaic cells with conducting polymer anodes", *Advanced Materials* **14**(9), 662-665 (2002).

[20] M. Drees, K. Premaratne, W. Graupner, J.R. Heflin, R.M. Davis, D. Marciu, M. Miller, "Creation of a gradient polymer-fullerene interface in photovoltaic devices by thermally controlled interdiffusion", *Applied Physics Letters* **81**(24), 4607-4609 (2002).

[21] M. Drees, R.M. Davis, D. Marciu, K. Premaratne, M. Miller, J.R. Heflin, "Improved polymer-fullerene interface in photovoltaic devices by thermally-controlled interdiffusion", *Polymer Preprints (American Chemical Society, Division of Polymer Chemistry)* **43**(2), 506-507 (2002).

[22] M. Drees, R.M. Davis, D. Marciu, K. Premaratne, W. Graupner, M. Miller, J.R. Heflin, "Nanoscale control of the polymer-fullerene interface in photovoltaic devices by thermally-controlled interdiffusion", *Materials Research Society Symposium Proceedings* **708**(Organic Optoelectronic Materials, Processing and Devices), 355-360 (2002).

[23] T. Schimmel, M. Schwoerer, H. Naarmann, "Mechanisms limiting the DC conductivity of high-conductivity polyacetylene", *Synthetic Metals* **37**(1-3), 1-6 (1990).

[24] R. Farchioni, G. Grosso (Eds.), *Organic electronic materials – conjugated polymers and low molecular weight organic solids*, Springer-Verlag, Berlin Heidelberg (2001).

[25] P.C. Eklund, A.M. Rao (Eds.), *Fullerene polymers and fullerene polymer composites*, Springer-Verlag, Berlin Heidelberg (2000).

[26] E.J.W. List, C. Creely, G. Leising, N. Schulte, A.D. Schluter, U. Scherf, K. Mullen, W. Graupner," Excitation energy migration in highly emissive semiconducting polymers", *Chemical Physics Letters* **325** (1-3), 132-138 (2000)

[27] I.D.W. Samuela, B. Crystallb, G. Rumblesb, P.L. Burn, A.B. Holmes and R.H. Friend, "The efficiency and time-dependence of luminescence from poly (p-phenylene vinylene) and derivatives", *Chem. Phys. Lett.* **213**(5-6), 472-478 (1993).

[28] N.T. Harrison, G.R. Hayes, R.T. Phillips, R.H. Friend, "Singlet Intrachain Exciton Generation and Decay in Poly(p-phenylenevinylene)", *Phys. Rev. Lett.* **77**, 1881–1884 (1996).

[29] C.H. Lee, G. Yu, A.J. Heeger, "Persistent photoconductivity in poly(p-phenylenevinylene): Spectral response and slow relaxation", *Phys. Rev. B* **47**, 15543–15553 (1993).

[30] T. W. Hagler, K. Pakbaz, A. J. Heeger, "Polarized-electroabsorption spectroscopy of a soluble derivative of poly(p-phenylenevinylene) oriented by gel processing in polyethylene: Polarization anisotropy, the off-axis dipole moment, and excited-state delocalization", *Phys. Rev. B* **49**, 10968–10975 (1994).

[31] M. Chandross, S. Mazumdar, S. Jeglinski, X. Wei, Z.V. Vardeny, E.W. Kwock, T.M. Miller, "Excitons in poly(para-phenylenevinylene)", *Phys. Rev. B* **50**, 14702–14705 (1994).

[32] R.N. Marks, J.J.M. Halls, D.D.C. Bradley, R.H. Friend, A.B. Holmes, "The photovoltaic response in poly(p-phenylene vinylene) thin-film devices", *J. Phys - Cond. Matt.* **6**(7), 1379-1394 (1994).

[33] S. Barth, H. Bässler, "Intrinsic Photoconduction in PPV-Type Conjugated Polymers", *Phys. Rev. Lett.* **79**, 4445–4448 (1997).

[34] M. Yan, L.J. Rothberg, F. Papadimitrakopoulos, M.E. Galvin, T.M. Miller, "Defect quenching of conjugated polymer luminescence", *Phys. Rev. Lett.* **73**(5), 744-747 (1994).

[35] L.J. Rothberg, M. Yan, S.Son, M.E. Galvin, E.W. Kwock, T.M. Miller, H.E. Katz, R.C. Haddon, F. Papadimitrakopoulos, "Intrinsic and extrinsic constraints on phenylenevinylene polymer electroluminescence", *Synthetic Metals* **78**, 231-236 (1996).

[36] K. Petritsch, "Organic solar cell architectures", *Ph.D. thesis*, Technical University Graz (2000), (available at http://www.solarpassion.com/solar_thesis/thesis.zip).

[37] K.L. Chopra, S.R. Das, *Thin film solar cells*, Plenum Press, New York (1983).

[38] C.J. Brabec, A. Cravino, D. Meissner, N.S. Sariciftci, T. Fromherz, M. Minse, L. Sanchez, J.C. Hummelen, "Origin of the Open Circuit Voltage in Plastic Solar Cells", *Advanced Functional Materials* **11**(5), 374-380 (2001).

[39] F.P. Incropera, D.P. De Witt, *Fundamentals of heat transfer*, John Wiley & Sons, New York (1981).

[40] D. Braun, A.J. Heeger, "Visible light emission from semiconducting polymer diodes", *Appl. Phys. Lett.* **58**(18), 1982-1984 (1991).

[41] I.D. Parker, "Carrier tunneling and device characteristics in polymer light-emitting diodes", *J. Appl. Phys.* **75**(3), 1656-1666 (1994).

[42] J.C. Scott, J.H. Kaufman, P.J.Brock, R. DiPietro, J. Salem, J.A. Goitia, "Degradation and failure of MEH-PPV light-emitting diodes", *J. Appl. Phys.* **79**(5), 2745-2751 (1996)

[43] N.S. Sariciftci, D. Braun, C. Zhang, V.I. Srdanov, A.J. Heeger, G. Stucky, F. Wudl, "Semiconducting polymer-buckminsterfullerene heterojunctions: Diodes, photodiodes, and photovoltaic cells", *Appl. Phys. Lett.* **62**(6), 585-587 (1993).

[44] M.G. Harrison, J. Gruener, G.C.W. Spencer, "Analysis of the photocurrent action spectra of MEH-PPV polymer photodiodes", *Phys. Rev. B* **55**(12), 7831-7849 (1997).

[45] J.J. Dittmer, K. Petritsch, A.E. Marseglia, R.H. Friend, H. Rost, A.B. Holmes, "Photovoltaic properties of MEH-PPV/PPEI blend devices", *Synthetic Metals* **102**, 879-880 (1999).

[46] I.H. Campbell, P.S. Davids, D.L. Smith, N.N. Barashkov, J.P. Ferraris, "The Schottky energy barrier dependence of charge injection in organic light-emitting diodes", *Appl. Phys. Lett.* **72**(15), 1863-1865 (1998).

[47] C.H. Lee, G. Yu, D. Moses, K. Pakbaz, C. Zhang, N.S. Sariciftci, A.J. Heeger, F. Wudl, "Sensitization of the photoconductivity of conducting polymers by C_{60} photoinduced electron-transfer", *Phys. Rev. B* **48**(20), 15425-15433 (1993).

[48] D. Gebeyehu, C.J. Brabec, F. Padinger, T. Fromherz, J.C. Hummelen, D. Badt, H. Schindler, N.S. Sariciftci, "The interplay of efficiency and morphology in photovoltaic devices based on interpenetrating networks of conjugated polymers with fullerenes", *Synthetic Metals* **118**(1-3), 1-9 (2001).

[49] E. Kymakis, I. Alexandrou, G.A.J. Amaratunga, "High open-circuit voltage photovoltaic devices from carbon-nanotube-polymer composites", *J. Appl. Phys.* **93**(3), 1764-1768 (2003).

[50] T.A. Chen, X. Wu, R.D. Rieke, "Regiocontrolled synthesis of poly(3-alkylthiophenes) mediated by Rieke zinc: their characterization and solid-state properties", *J. Am. Chem. Soc.* **117**, 233-244 (1995).

[51] S. Malik, A.K. Nandi, "Crystallization mechanism of regioregular poly(3-alkyl thiophene)s", *J. Polym. Phys.* **40**, 2073-2085 (2002).

[52] R.J. Young and P.A. Lovell, *Introduction to polymers*, Chapman & Hall, New York (1991), p. 297

[53] D. Gebeyehu, C.J. Brabec, N.S. Sariciftci, D. Vangeneugden, R. Kiebooms, D. Vanderzande, F. Kienberger, H. Schindler, "Hybrid solar cells based on dye-sensitized nanoporous TiO2 electrodes and conjugated polymers as hole transport materials", *Synthetic Metals* **125**(3), 279-287 (2001).

[54] M.S. Dresselhaus, G. Dresselhaus, P.C. Eklund, "Fullerenes", *J. Mater. Res.* **8**(8), 2054-2097 (1993).

[55] C.J. Brabec, N.S. Sariciftci, J.C. Hummelen, "Plastic Solar Cells", *Adv. Funct. Mater.* **11**(1), 15-26 (2001).

[56] Y. Park, V. Choong, Y. Gao, B. R. Hsieh, C. W. Tang, " Work function of indium tin oxide transparent conductor measured by photoelectron spectroscopy", *Appl. Phys. Lett.* **68**(19), 2699-2701 (1996).

[57] J.S. Kim, M. Granström, R.H. Friend, N. Johansson, W.R. Salaneck, R. Daik, W.J. Feast, F. Cacialli, " Indium–tin oxide treatments for single- and double-layer polymeric light-emitting diodes: The relation between the anode physical, chemical, and morphological properties and the device performance", *J. Appl. Phys* **84**(12), 6859-6870 (1998).

[58] T.M. Brown, J.S. Kim, R.H. Friend, F. Cacialli, R. Daik, W.J. Feast, " Built-in field electroabsorption spectroscopy of polymer light-emitting diodes incorporating a doped poly(3,4-ethylene dioxythiophene) hole injection layer", *Appl. Phys. Lett.* **75(**12), 1679-1681 (1999).

[59] H.B.Michaelson, "The workfunction of the elements an its periodicity", *J. Appl. Phys.* **48**(11), 4729-4733 (1977).

[60] Landolt-Börnstein, *Numerical data and functional relationships in science and technology*, Vol. 23a, Springer, Berlin (1961).

[61] A.C. Arias, M. Granstrom, D.S. Thomas, K. Petritsch, R.H. Friend, "Doped conducting-polymer-semiconducting-polymer interfaces: their use in organic photovoltaic devices", *Phys. Rev. B* **60**(3), 1854-1860 (1999).

[62] C.Y. Yang, A.J. Heeger, "Morphology of composites of semiconducting polymers mixed with C_{60}", *Synthetic Metals* **83**, 85-88 (1996).

[63] T.C. Nguyen, V. Doan, B.J. Schwartz, "Conjugated polymer aggregates in solution: Control of interchain interactions", *J. Chem. Phys.* **110**(8), 4068-4078 (1999).

[64] J. Liu, Y. Shi, Y. Yang, "Solvation-induced morphology effects on the performance of polymer-based photovoltaic devices", *Adv. Funct. Mater.* **11**(6), 420-424 (2001).

[65] C. Schlebusch, B. Kessler, S. Cramm, W.Eberhardt, "Organic photoconductors and C_{60}", *Synthetic Metals* **77**, 151-154 (1996).

[66] J.M.G. Cowie, *Polymers: chemistry & physics of modern materials*, Intertext Books (1973).

Vita

Martin Drees was born on April 10th, 1975 in Bochum, Germany. In 1997 he received his Vordiplom in Physik from the Technische Universität Carolo-Wilhelmina zu Braunschweig, Germany. In 1998 he joined the Physics Department at the Virginia Polytechnic Institute and State University in Blacksburg, VA as a graduate student. From there he received his M. SC. in Physics in May 2000. In 2002, he received the Ray F. Tipsword Graduate Scholarship in recognition of excellence in research in the area of condensed-matter physics, optics, or statistical physics. In May 2003 he obtained his Ph.D. in Physics from the same university